

TEST METHOD FOR EVALUATING THERMAL-SPRAYED
COATINGS UNDER UNIFORM STRAIN CONDITIONS

Christine Steinkamp
B.S., Portland State University, 1979

A thesis submitted to the faculty of the
Oregon Graduate Institute of Science & Technology
in partial fulfillment of the
requirements for the degree
Master of Science
in
Material Science and Engineering

October, 1994

The thesis "Test Method for Evaluating Thermal-Sprayed Coatings Under Uniform Strain Conditions" by Christine A. Steinkamp has been examined and approved by the following Examination Committee:

Dr. William E. Wood,
Thesis Advisor
Professor and Department Head

Dr. Lemmy Meekisho
Assistant Professor

Dr. Margaret Ziomek-Moroz
Assistant Professor

Dr. Milt Scholl
Assistant Professor

Acknowledgements

I wish to express my gratitude to my advisor Professor William Wood for his support and encouragement during this work.

I am grateful to the CWS company for their thermal spray services. I gratefully acknowledge the sponsorship of the Edison Welding Institute and appreciation is also extended to the Hartford steam Boiler Company for their technical support in acoustic emission matters.

I also wish to thank the members of the thesis committee, Dr. Milt Scholl, Dr. Lemmy Meekisho, and Dr. Margaret Ziomek-Moroz for their helpful suggestions and comments.

I also wish to express much gratitude to my husband and children, for allowing me to pursue and complete this goal of mine.

Finally, much praise and thanks to my Lord God and to His Son Jesus Christ for the chance to attend the Oregon Graduate Institute and further my education.

Table of Contents

ACKNOWLEDGEMENTS	iii
TABLE OF CONTENTS	iv
LIST OF TABLES	vi
LIST OF FIGURES	vii
ABSTRACT	xii
1. INTRODUCTION	1
2. BACKGROUND	3
2.1. THERMAL SPRAY COATING	3
2.2. ACOUSTIC EMISSIONS (AE)	7
2.3. ACOUSTIC EMISSION PARAMETERS	9
2.4. BOILER TUBE STRAIN CALIBRATION	10
2.5. MULTIPLE TESTING	11
2.6. KAISER EFFECT	11
3. EXPERIMENTAL PROCEDURE	12
3.1. MATERIALS	12
3.2. TEST SPECIMEN PREPARATION	12
3.3. MONITORING AND RECORDING EQUIPMENT	13
3.4. PRESSURE TESTING	13
3.5. DYE PENETRANT TESTS	14
3.6. METALLOGRAPHY	14
3.7. SCANNING ELECTRON MICROSCOPE	15
4. RESULTS	16
4.1. BACKGROUND STRAIN ANALYSIS RESULTS	16
4.2. COATING PROFILE	16
4.3. COATING PLACEMENT	16
4.4. NON-DESTRUCTIVE INSPECTION RESULTS	17
4.4.1. DYE PENETRANT TESTS	17
4.4.2. ACOUSTIC EMISSION TESTS	17
4.4.2.1. ALUMINUM OXIDE COATINGS	17
4.4.2.2. STAINLESS STEEL COATINGS	19
4.4.2.3. MOLYBDENUM-IRON BLEND COATING	20

4.5. MICROSTRUCTURE	23
4.5.1. ALUMINUM OXIDE	23
4.5.2. STAINLESS STEEL	23
4.5.3. MOLYBDENUM-IRON BLEND COATING	24
5. DISCUSSION	26
5.1. INTRODUCTION	26
5.2. SOURCE LOCATION	26
5.3. KAISER EFFECT	27
5.4. ALUMINUM OXIDE COATING	27
5.5. STAINLESS STEEL	29
5.6. MOLYBDENUM-IRON BLEND COATING	32
6. CONCLUSIONS	34
7. RECOMMENDATIONS	35
APPENDIX 1 – METALLOGRAPHY PROCEDURES	36
APPENDIX 2 – PROCEDURE FOR DYE PENETRANT TESTING OF COATINGS	37
APPENDIX 3 – TYPICAL A.E. TEST PARAMETERS	38
FIGURES	40
TABLES	95
REFERENCES	103
BIOGRAPHICAL SKETCH	106

List Of Tables

TABLE I - Coating Matrix	95
TABLE II - Test Code Designation	96
TABLE III - Maximum Strain Reached By Each Tube	97
TABLE IV - Test Statistics of Accepted Events	98
TABLE V - Test Statistics of Rejected Events	99
TABLE VI - Strain At Which Onset of Significant AE Activity Began	100
TABLE VII - Approximate Slope of Total Events vs. Strain Plots	102

List Of Figures

Figure 1 – LOCATION OF STRAIN GAGES FOR STRAIN ANALYSIS . . .	40
Figure 2 – COATING PLACEMENT	41
Figure 3 – ACOUSTIC EMISSION SENSOR LAYOUT	42
Figure 4 – COATING PROFILE	43
Figure 5 – TEST SYSTEM CONFIGURATION	44
Figure 6 – ACOUSTIC EMISSION SENSORS IN POSITION ON COATED TUBING	45
Figure 7 – BANDSAW SECTIONING OPERATION	46
Figure 8 – LATHE SECTIONING OPERATION	46
Figure 9 – STRAIN VALUES AT VARIOUS POSITIONS ALONG UNSPRAYED BOILER TUBE. INITIAL PRESSURIZATION TO 6,000 PSI. . .	47
Figure 10a – STRAIN VALUES AT VARIOUS POSITIONS ALONG UNSPRAYED BOILER TUBE. INITIAL PRESSURIZATION TO 13,000 PSI.	48
Figure 10b – STRAIN VALUES AT VARIOUS POSITIONS ALONG UNSPRAYED BOILER TUBE. SUBSEQUENT PRESSURIZATION TO 13,000 PSI.	48
Figure 11 – STRAIN GAGES FOR STRAIN ANALYSIS MOUNTED ON BARE BOILER TUBE, 6000 PSI MAXIMUM PRESSURE.	49
Figure 12 – DISTRIBUTION OF EVENTS BY LOCATION FOR BARE TUBE, INITIAL PRESSURIZATION	50
Figure 13 – DYE PENETRANT TEST FOR .015" THICK AL ₂ O ₃ COATING MAXIMUM STRAIN CONDITION	51
Figure 14 – DYE PENETRANT TEST FOR .030" THICK AL ₂ O ₃ COATING MAXIMUM STRAIN CONDITION	51
Figure 15 – DYE PENETRANT TEST FOR .045" THICK STRAINED AL ₂ O ₃ COATING, MAXIMUM STRAIN CONDITION	52
Figure 16 – DYE PENETRANT TEST FOR .045" THICK AL ₂ O ₃ COATING, MINIMUM STRAIN CONDITION.	53
Figure 17 – DYE PENETRANT TEST FOR .030" THICK AL ₂ O ₃ COATING, UNSTRAINED CONDITION.	54
Figure 18 – TYPICAL DYE PENETRANT TEST FOR .045" THICK STAINLESS STEEL COATING, MAXIMUM STRAIN CONDITION	55
Figure 19 – TYPICAL DYE PENETRANT TEST FOR .070" THICK STAINLESS STEEL COATING, MAXIMUM STRAIN CONDITION.	55

Figure 20 – TYPICAL DYE PENETRANT TEST FOR .100" THICK STAINLESS STEEL COATING, MAXIMUM STRAIN CONDITION.	56
Figure 21 – DYE PENETRANT TEST FOR STAINLESS STEEL COATING, UNSTRAINED CONDITION.	56
Figure 22 – DYE PENETRANT TEST .020" THICK Mo-Fe BLEND COATING, MAXIMUM STRAIN CONDITION.	57
Figure 23 – DYE PENETRANT TEST .030" THICK Mo-Fe BLEND COATING, MAXIMUM STRAIN CONDITION.	57
Figure 24 – DYE PENETRANT TEST FOR .040" THICK Mo-Fe BLEND COATING, MAXIMUM STRAIN CONDITION.	58
Figure 25 – DYE PENETRANT TEST FOR .030" THICK Mo-Fe BLEND COATING (INERT GAS ATMOSPHERE), UNSTRAINED COATING.	59
Figure 26 – DYE PENETRANT TEST FOR .030" THICK Mo-Fe BLEND COATING (STANDARD GAS ATMOSPHERE), UNSTRAINED COATING.	59
Figure 27 – DYE PENETRANT TEST FOR .020" THICK Mo-Fe BLEND COATING, MINIMUM STRAIN CONDITION.	60
Figure 28 – DYE PENETRANT TEST FOR .030" THICK Mo-Fe BLEND COATING, MINIMUM STRAIN CONDITION.	61
Figure 29 – DYE PENETRANT TEST FOR .040" THICK Mo-Fe BLEND COATING, MINIMUM STRAIN CONDITION.	62
Figure 30 – TYPICAL DISTRIBUTION OF EVENTS BY LOCATION FOR AL ₂ O ₃ COATINGS.	63
Figure 31 – TYPICAL DISTRIBUTION OF EVENTS BY LOCATION FOR Mo-Fe BLEND COATINGS.	63
Figure 32 – TYPICAL DISTRIBUTION OF EVENTS BY LOCATION FOR STAINLESS STEEL COATINGS.	64
Figure 33 – TYPICAL PLOT OF TOTAL ENERGY VS. STRAIN FOR .045" THICK AL ₂ O ₃ COATING.	65
Figure 34 – TYPICAL PLOT OF DISTRIBUTION OF EVENTS BY PEAK AMPLITUDE (dB) FOR .045" THICK AL ₂ O ₃ COATING, MAXIMUM STRAIN CONDITION.	65
Figure 35 – TYPICAL PLOT OF LOG OF CUMULATIVE DISTRIBUTION OF EVENTS BY PEAK AMPLITUDE (dB) FOR .045" THICK AL ₂ O ₃ COATING, MAXIMUM STRAIN CONDITION.	66
Figure 36 – TYPICAL DISTRIBUTION OF EVENTS BY ENERGY FOR .045" THICK AL ₂ O ₃ COATING, MAXIMUM STRAIN CONDITION.	66
Figure 37 – TYPICAL TOTAL ENERGY VS. STRAIN FOR .045" THICK AL ₂ O ₃ COATINGS, MAXIMUM STRAIN CONDITION.	67
Figure 38 – TYPICAL PLOT OF MEAN ENERGY VS. STRAIN FOR .045" THICK AL ₂ O ₃ COATINGS, MAXIMUM STRAIN CONDITION. ...	67

Figure 39 – TYPICAL DISTRIBUTION OF EVENTS BY PEAK AMPLITUDE (dB) for .045" THICK STAINLESS STEEL COATING, MAXIMUM STRAIN CONDITION.	68
Figure 40 – TYPICAL DISTRIBUTION OF EVENTS BY PEAK AMPLITUDE (dB) for .070" THICK STAINLESS STEEL COATING, MAXIMUM STRAIN CONDITION.	68
Figure 41 – TYPICAL DISTRIBUTION OF EVENTS BY PEAK AMPLITUDE (dB) for .100" THICK STAINLESS STEEL COATING, MAXIMUM STRAIN CONDITION.	69
Figure 42 – TYPICAL DISTRIBUTION OF EVENTS BY ENERGY FOR .045" THICK STAINLESS STEEL COATINGS, MAXIMUM STRAIN CONDITION.	69
Figure 43 – TYPICAL DISTRIBUTION OF EVENTS BY ENERGY FOR .070" THICK STAINLESS STEEL COATINGS, MAXIMUM STRAIN CONDITION.	70
Figure 44 – TYPICAL DISTRIBUTION OF EVENTS BY ENERGY FOR .100" THICK STAINLESS STEEL COATINGS, MAXIMUM STRAIN CONDITION.	70
Figure 45 – TYPICAL TOTAL ENERGY VS. STRAIN FOR .045" THICK STAINLESS STEEL COATING. MAXIMUM STRAIN CONDITION.	71
Figure 46 – TYPICAL TOTAL ENERGY VS. STRAIN FOR .070" THICK STAINLESS STEEL COATING. MAXIMUM STRAIN CONDITION.	71
Figure 47 – TYPICAL TOTAL ENERGY VS. STRAIN FOR .100" THICK STAINLESS STEEL COATING. MAXIMUM STRAIN CONDITION.	72
Figure 48 – TYPICAL LOG OF CUMULATIVE DISTRIBUTION OF EVENTS BY PEAK AMPLITUDE FOR .045" THICK STAINLESS STEEL COATING.	72
Figure 49 – TYPICAL LOG OF CUMULATIVE DISTRIBUTION OF EVENTS BY PEAK AMPLITUDE FOR .070" THICK STAINLESS STEEL COATING.	73
Figure 50 – TYPICAL LOG OF CUMULATIVE DISTRIBUTION OF EVENTS BY PEAK AMPLITUDE FOR .100" THICK STAINLESS STEEL COATING.	73
Figure 51 – DISTRIBUTION OF EVENTS BY PEAK AMPLITUDE (dB) FOR .020" THICK Mo–Fe BLEND COATING, MAXIMUM STRAIN CONDITION.	74
Figure 52 – DISTRIBUTION OF EVENTS BY PEAK AMPLITUDE (dB) FOR .030" THICK Mo–Fe BLEND COATING, MAXIMUM STRAIN CONDITION.	74
Figure 53 – DISTRIBUTION OF EVENTS BY PEAK AMPLITUDE (dB) FOR .040" THICK Mo–Fe BLEND COATING, MAXIMUM STRAIN CONDITION.	75

Figure 54 – DISTRIBUTION OF EVENTS BY ENERGY FOR .020" THICK Mo-Fe BLEND COATING, MAXIMUM STRAIN CONDITION.	75
Figure 55 – DISTRIBUTION OF EVENTS BY ENERGY FOR .030" THICK Mo-Fe BLEND COATING, MAXIMUM STRAIN CONDITION.	76
Figure 56 – LOG CUMULATIVE DISTRIBUTION OF EVENTS BY PEAK AMPLITUDE FOR .030" THICK Mo-Fe BLEND COATING. MAXIMUM STRAIN CONDITION.	76
Figure 57 – LOG CUMULATIVE DISTRIBUTION OF EVENTS BY PEAK AMPLITUDE (dB) FOR .040" THICK Mo-Fe BLEND COATING. MAXIMUM STRAIN CONDITION.	77
Figure 58 – TOTAL ENERGY VS. STRAIN FOR .020" THICK Mo-Fe BLEND COATING. MAXIMUM STRAIN CONDITION.	77
Figure 59 – TOTAL ENERGY VS. STRAIN FOR .030" THICK Mo-Fe BLEND COATING. MAXIMUM STRAIN CONDITION. ...	78
Figure 60 – TOTAL ENERGY VS. STRAIN FOR .040" THICK Mo-Fe BLEND COATING. MAXIMUM STRAIN CONDITION.	78
Figure 61 – SEM MICROGRAPH OF TYPICAL MICROSTRUCTURE OF UNSTRAINED .030" AL ₂ O ₃ COATING. TOP IS SEM AND BOTTOM IS BSE-COMPOSITION, 200X.	79
Figure 62 – SEM MICROGRAPH OF TYPICAL CRACKED AREA IN .015" THICK AL ₂ O ₃ COATING. TOP IS SEM AND BOTTOM IS BSE-COMPOSITION, 500X.	79
Figure 63 – SEM MICROGRAPH OF TYPICAL CRACKED AREA IN .030" THICK AL ₂ O ₃ COATING. TOP IS SEM AND BOTTOM IS BSE-COMPOSITION, 200X.	80
Figure 64 – SEM CLOSE UP OF A CRACK IN .045" THICK AL ₂ O ₃ COATING 3000X.	80
Figure 65 – OPTICAL MICROGRAPH OF CRACKED AREA IN .045" THICK AL ₂ O ₃ COATING. 50X.	81
Figure 66 – SEM MICROGRAPH OF THE MICROSTRUCTURE OF .030" THICK STAINLESS STEEL COATING, UNSTRAINED CONDITION. TOP IS SEM AND THE BOTTOM IS BSE – TOPOGRAPHY. 100X.	82
Figure 67 – SEM MICROGRAPH OF THE MICROSTRUCTURE OF .100" THICK STAINLESS STEEL COATING, STRAINED CONDITION. TOP IS SEM AND THE BOTTOM IS BSE – TOPOGRAPHY. 100X.	82
Figure 68 – SEM MICROGRAPH OF THE MICROSTRUCTURE OF .070" THICK STAINLESS STEEL COATING. STRAINED CONDITION. ...	83
Figure 69 – SEM MICROGRAPH OF THE MICROSTRUCTURE OF .100" THICK STAINLESS STEEL COATING. STRAINED CONDITION. 30X. ...	83
Figure 70 – SEM MICROGRAPH OF .100" THICK STAINLESS STEEL COATING. STRAINED CONDITION. BSE – TOPOGRAPHY 30X.	84

Figure 71 – SEM MICROGRAPH OF .045” THICK STAINLESS STEEL COATING. 30X.	84
Figure 72 – MICROGRAPH OF EDX ANALYSIS AREAS. 2000X.	85
Figure 73 – EDX ANALYSIS OF AREA USSP1	85
Figure 74 – EDX ANALYSIS OF AREA USSP2	86
Figure 75 – EDX ANALYSIS OF AREA USSP3	86
Figure 76 – EDX ANALYSIS OF AREA USSP4	87
Figure 77 – EDX ANALYSIS OF AREA USSP5	87
Figure 78 – SEM MICROGRAPH OF .030” THICK Mo–Fe BLEND COATING UNSTRAINED CONDITION (STANDARD ATMOSPHERE). SEM. 200X.	88
Figure 79 – SEM MICROGRAPH OF .030” THICK Mo–Fe BLEND COATING UNSTRAINED CONDITION (STANDARD ATMOSPHERE). BSE–COMPOSITION. 500X.	88
Figure 80 – SEM MICROGRAPH OF .030” THICK Mo–Fe BLEND COATING. UNSTRAINED CONDITION. (ARGON ATMOSPHERE). SEM. 200X.	89
Figure 81 – SEM MICROGRAPH OF CRACKING IN .030” THICK Mo–Fe BLEND COATING. BSE–COMPOSITION. 100X.	89
Figure 82 – SEM MICROGRAPH CLOSE UP OF CRACK FROM FIGURE 84. BSE–COMPOSITION. 500X.	90
Figure 83 – SEM MICROGRAPH OF CIRCUMFERENTIAL CROSS SECTION OF COATING FROM FIGURES 84 AND 85. TOP IS SEM AND BOTTOM IS BSE–COMPOSITION 100X. .	90
Figure 84 – SEM MICROGRAPH OF CRACKING IN .040” THICK Mo–Fe BLEND COATING. TOP IS SEM AND BOTTOM IS BSE–COMPOSITION. 100X.	91
Figure 85 – SEM MICROGRAPH OF CRACKING IN .043” THICK Mo–Fe BLEND COATING. TOP IS SEM AND BOTTOM IS BSE–COMPOSITION. 100X. CIRCUMFERENTIAL DIRECTION ..	91
Figure 86 – SEM MICROGRAPH OF MINOR CRACKING IN .020” THICK Mo–Fe BLEND COATING, MINIMUM STRAIN. TOP IS SEM AND BOTTOM IS BSE–COMPOSITION. 500X.	92
Figure 87 – SEM MICROGRAPH OF MINOR CRACKING IN .030” THICK Mo–Fe BLEND COATING, MINIMUM STRAIN. BSE–COMPOSITION. 500X.	92
Figure 88 – SEM MICROGRAPH OF MINOR CRACKING IN .040” THICK Mo–Fe BLEND COATING, MINIMUM STRAIN. BSE–COMPOSITION. 200X. INSET = 400X.	93
Figure 89 – EDX ANALYSIS OF Mo–Fe BLEND COATING.	94
Figure 90 – EDX ANALYSIS OF Mo–Fe BLEND COATING.	94

ABSTRACT

This study represents fundamental research undertaken to establish the bounds of the Acoustic Emission (A.E.) responses of thermal-sprayed coatings during pressurized testing. Surface coating of tubes and pipes is of significant importance to many industries such as power generation, pulp and paper, and chemical processing for purposes of environmental protection, wear, and thermal conductivity. While thermally-sprayed coatings are attractive for their surface protection they have drawbacks such as delamination from substrate material and cracking. This study used continuous A.E. monitoring to determine the threshold stress loads that initiated coating failure.

Initial test specimens were based upon the current industry standard (9" x 1" flat bars) used in 3-point and 4-point bending. The results from those tests were not conclusive due to specimen geometry effects, and a change in the test configuration was made to one that resulted in large uniform stresses by using pressurized tubes. Post test failure analysis of the crack propagation (longitudinal and/or circumferential) was studied using dye penetrant test and scanning electron microscopy. This information was correlated with the real time A.E. results to begin developing a database to assess the quality and fracture resistance of thermal-sprayed coatings.

The findings indicate that the fracture resistance of the coating is inversely proportional to the coating thickness. Three coating materials were used in this study, plasma-sprayed aluminum oxide, flame sprayed stainless steel 420 and a plasma sprayed Mo-Fe blend. Of the three coating materials studied, the molybdenum-iron blend and aluminum oxide were more susceptible to cracking at relatively lower stresses than the stainless steel 420. There was, for the molybdenum blend coating, a change in the crack propagation pattern based upon the thickness of the coating.

1. INTRODUCTION

Acoustic Emission (AE) technology, used for many years to investigate failure characteristics of thermal-sprayed coatings, can be coupled with various test methods for straining coatings to detect the onset of cracking. Two of these methods are ASTM 633-79 Tensile Adhesion Test and flat bar testing.

The ASTM 633-79 Tensile Adhesion Test measures the amount of adhesion a coating has to a substrate or the cohesive strength of a coating in tension normal to the surface. The test consists of depositing a coating on one face of a substrate fixture, bonding a loading fixture to the free surface of the coating, and loading this assembly of coating and fixtures with a tensile load normal to the plane of the coating. This test does not address the surface cracking resistance of the coatings.

Flat bar testing consists of depositing a coating onto one surface of a flat bar of metal. The strip is then bent in a 3-point or 4-point fixture with the coating on the tension side of the metal bar. Flat bar bend testing provides an avenue for investigating cracking resistance of coatings.

Many investigators have been able to couple AE monitoring with strain and microstructural data to gain insight into cracking mechanisms that a particular coating would undergo upon loading. [1, 2, 3, 6, 7, 8]. Neither of these testing styles gives an exact value of stress that a particular coating/substrate combination can resist in terms of cracking. This is due to the residual stresses inherent in thermally applied coatings, the shape of a particular coated part, and that coatings are stressed in the field in a more complicated manner than is usually realized in the ASTM 633 test or the flat bar bend tests.

Limitations of the ASTM 633 style testing arise due to the bonding agent. One limitation is that the bonding agent can compromise test results for coatings less than .015" in thickness. This is due to the bonding agent infiltrating the coating. Another problem that has developed over the years is that the bonding strength of some coating/substrate interfaces

have exceeded the strength of the bonding agent. This is caused by increased expertise over the years of spray applicators into the parameters that create a high value of adhesive and cohesive strength for a coating.

A limitation of the flat bar tests is the influence of the coatings sharp edges on the stress required to crack the coatings. These sharp edges produce stress concentrations which cause cracks to originate at the edges and propagate inward even for uniform strain conditions.

This research program evaluated acoustic emission data obtained during testing of thermal-sprayed coatings under a test configuration that differed from the ASTM –633 or flat bar bend configurations. Initial testing considered coatings deposited onto flat bars. The coating samples differed only by initial powder distribution. The bars were then loaded in a 3-point bend mode with the coating in tension until cracking was detected by AE monitoring. The tests revealed that cracking was detected but differences in cracking due to coating variations was difficult to distinguish due to edge effects and non-uniform loading.

The next phase of testing involved development and evaluation of a new test method to replace the flat bar test commonly used. Along with developing a new test configuration, testing entailed selecting coating materials which were predicted to crack in obviously different modes. Coatings were selected which featured expected differences in ductile and brittle behavior. A new test configuration was developed to allow large test areas of uniform strain conditions in the coatings with the elimination of edge effects, and gave the ability to conduct multiple tests during a single test run.

The new configuration consisted of using a capped section of high-strength boiler tube as the substrate. The tube was sprayed with the test coating, filled with water, and hydrostatically loaded until a desired level of strain was obtained. During loading, the tube was monitored for pressure, strain, and AE data. The procedure can be found in the Procedures section of this body of work. The coatings were then dye penetrant tested for evidence of surface cracking and then metallographically prepared for microstructural analysis. The AE, dye penetrant test, and the microstructure results were compared for interpretation of the significance of the AE signal signature in terms of coating cracking behavior.

2. BACKGROUND

2.1. THERMAL SPRAY COATING*

The term thermal spray is a general term used to describe the process of depositing metallic and non-metallic coatings onto various surfaces. These processes are usually flame spray, plasma-arc spray, or electric-arc spray. Coatings are sprayed from rod, wire stock, or in a powdered form.

For the rod or wire stock form, the material is fed into a flame axially and melted. The molten stock is then removed from the end of the rod or wire, atomized by a high velocity stream of compressed gas (air or other gas) and propelled onto a prepared substrate.

In powdered form, the material is metered by a powder feeder or hopper into a stream of gas (air or other gas) which suspends and delivers the material to the flame. The material is melted or semi-melted and propelled to be deposited on a substrate. As the molten or semi-molten particles impact on the substrate, a coating begins to build up. One or more of the following three bonding mechanisms cause this build up.

- Mechanical bonding occurs when particles splatter on the substrate into a flatter particle shape. The particles interlock with the rough surface or other deposited particles and build up in a lamellar fashion.
- Localized diffusion or alloying can occur for some combinations of coating materials and substrates.
- Van de Waals forces may cause some bonding similar to the bonds formed when two optical flats are in contact.

This thermal spray manner of depositing does produce interesting material responses. For ceramic coatings the response is often in the form of extensive microcracking. Metallic coatings can often exhibit large residual stresses during coating build-up.

*Thermal spray information is based upon "Thermal Spray Coatings", Clare, James H. and Crawmer, Daryl E., ASTM Handbook, Vol 5, 9th edition, pps.361-374.

Numerous processes are employed for depositing the coatings. The following six are briefly discussed here: plasma-arc, transferred plasma-arc, inert atmosphere chamber spraying, electric-arc, flame spray, and flame spray and fuse.

Plasma-arc spray

The plasma-arc spray method usually produces higher temperatures and higher powder particle velocities than other methods. The coating produced have high densities and bond strengths. The use of inert arc gas produces a lower oxide content for metal coatings.

Transferred plasma-arc spray

The transferred plasma-arc process adds the capability of substrate heating and melting to the plasma-arc spray method. The advantages gained by this method are metallurgical bonding, high density coatings, high deposition rates, and a high thickness per pass. Less electrical power is needed than for the nontransferred arc process. This methods helps minimize many problems relating to using powders with wide particles size distributions or large particle sizes. Shortcomings of the process are that microstructure of the substrate can be altered, the substrate needs to be electrically conductive, and must be able to withstand some deformation.

Inert atmosphere and low pressure chamber spray

The inert atmosphere chamber spraying technique is used to confine hazardous materials and to restrict the formation of oxides that can occur in a normal atmosphere. Plasma spraying in an inert atmosphere, low pressure chamber has a number of advantages over spraying in an inert atmosphere at atmospheric pressure. Bond strength is increased in low pressure chambers because higher substrate temperatures occur which allow the coating to diffuse into the substrate. Deposition efficiency can be increased due to a longer dwell time of a particle in the longer heating zone of the plasma and minimal changes in chemistry of the coating because of the inert atmosphere. The low pressure spraying is best controlled by computer to ensure reproducibility and a uniform coating.

Electric-arc spray

The electric-arc spray process uses metal in wire form. There is no external heat source (such as gas flame or plasma) with this method. Heating and melting occur when two electrically opposed charged wires are fed together so that a controlled arc is produces at the intersection. The wires are composed of the depositing material. The molten metal is at-

omized and propelled onto a prepared substrate by a stream of compressed gas or air. This method generally exhibits high bond strengths for some combinations. Substrate heating is lower than other processes and electrical power needs are low. The electric–arc process is limited to relatively ductile and electrically conductive wire. So far, electric–arc coatings of carbides, nitrides, and oxides are not practical.

Flame spray

The flame spray process uses a combustible gas to melt coating material. Flame spray guns are able to spray powder, rod, or wire forms of coating material. Commonly used flame spray gases are acetylene, propane, mapp gas, and oxygen–hydrogen. Lower costs (capital investment and maintenance), high deposition rates and efficiencies, and relative ease are the attractive features of this method. The deposited coatings resulting from this method generally exhibit lower bond strengths, higher porosity, a narrower working temperature range, and higher heat transmitted to the substrate than the plasma–arc or electric–arc spray methods. The flame spray method is frequently used to renovate out of tolerance or worn out parts.

Flame spray and fuse

In a modification of the flame spray method, the coating materials are self fluxing and fusible which require post–spray heat treatment. Parts are prepared and sprayed as for other methods and then are fused. Several methods are used to fuse the coatings among which are flame, torch, induction, and in vacuum, inert or hydrogen furnace.

Spray and fuse coatings generally have good resistance to wear. This method allows for the use of less expensive substrate materials. The coatings produced are fully dense and show metallurgical bonds. Some drawbacks with this method are that substrate material is limited to those that can tolerate 1010° to 1175° C fusing temperatures, fusing temperatures may change the heat treated properties of some alloys.

Surface Preparation

Since mechanical bonding is a primary factor in coating adhesion to a substrate, surface preparation of the substrate material is important. For all spray methods, surface cleanliness is important. It is necessary to make sure all lubricants, oils (equipment or body) are removed before coatings are deposited. Deposits are removed by scraping, wire brushing, machining, grit blasting, or chemical removal.

After the substrate has been cleaned, surface roughening is generally the next step before coating a substrate. Two types of roughening typically used are rough threading and grit blasting.

Rough threading is used often on cylindrical surfaces. This method is limited to thicker substrates and is not recommended for thin coatings. If grit blasting follows threading, a higher bond strength can be achieved.

Grit blasting uses either aluminum oxide, sand, crushed steel, silicon carbide or iron. A number of factors are involved in selecting a grit size and material. The selection of the particle size is determined by the required coating thickness, whether or not the generated roughness will affect the smoothness of the finished coating. Grit material may chemically react with the substrate and adversely affect the finished coating. Some grit may embed itself into softer substrate materials such as aluminium, copper or alloys of these materials. Varying the grit blasting air pressure may alleviate some problems while for others it is a matter of being guided by industry literature of matching grit size, grit material, substrate material, and thermal spray method.

Finishing Treatments

Two common features of thermal spray coatings in the as sprayed condition is a rough surface finish and a porous structure. Typical surface roughness run 5.0 to 13 μ m to 200 to 50 μ m. Porosity is generally 2 to 17 VOL %. Many coatings are sealed before use by machining or grinding. Sealing fills the pores of a coating to remove the possibility of fluid or corrosive material penetration.

Thermal sprayed coating can be finished using standard techniques, but care must be taken during the operations. Due to the nature of their bonding, the method selected needs to be considered carefully. Some adverse affects of an incorrect matching of coatings and finishing techniques are excessive particle pull-out or coating spalling.

While machining a match between coating materials and cutting tools is required with regard to the structure and bond nature of the coatings. High speed tools can be used to cut softer sprayed materials. The harder coatings often require the use of carbide tools or grinding (silicone carbide or diamond). It is usually advisable that coatings are machined under lubricated conditions.

All spray coating can be polished and buffed but results depend on coating hardness for the final results.

2.2. ACOUSTIC EMISSIONS (AE) *

When a material is under stress and a sudden displacement takes place somewhere within a material, stress waves are created at the source of the displacement and propagated throughout the material. The stress waves are called acoustic emissions. Generally the displacement wave takes the form of a step like function and corresponds to permanent change. The associated stress and velocity waves take on a more pulse type of form which is dependent on the actions of the source processes. This wave can last from fractions of a microsecond for submicroscopic dislocations to minutes for large seismic movement. This wave radiates out in all directions throughout the stressed material with directionality being a factor. This wave can be detected by a number of means among which a resonant sensor is a popular choice. The important feature of a resonant sensor is a piezoelectric crystal which converts movement to an electrical signal. The housing for the crystal generally consists of a ceramic wear plate, metal casing, and a connector. As the sensor is excited the signal is carried to a preamplifier which boosts the signal to more useful voltage and sends it to the main signal processing equipment. These resonant type sensors have one or more crystal size and shape. The sensor is usually coupled to the test piece with a viscous couplant and then secured with tape, magnetic hold-on, or some similar type of device, or the sensor may be mounted on a wave guide. The preamplifier is usually placed close to or inside the sensor to minimize stray electromagnetism interference. Preamplifiers usually produce either a 10 (40 dB) or 20 (60dB) gain and have bandpass filters to eliminate low frequency mechanical or acoustical noise.

After the signal leaves the preamplifier, it is delivered to the main instrument where it is amplified and filtered again.

The sensors produce many signals during a test. A single signal is known as a burst type. When these burst signals occur at a high rate the signals are described as being continuous.

The processing equipment has a comparator circuit which generates a digital output whenever the AE signal exceeds an operator selected threshold voltage. This threshold

*Background information on AE is based upon "Acoustic Emission Inspection, Pollock, Adrian A., ASTM Handbook, 9th ed., pps 278-291.

voltage level determines the sensitivity of the test. These voltage levels can be fixed or floated depending upon the acoustic environment that the test specimen is in. Signal sensitivity can also be controlled by additional gain occurring in the signal processing unit as decided by the operator. The signal processing unit provides a signal to the digital AE function modules to indicate that an input has crossed the threshold event. The AET5500 system has an AET model 208 signal processing unit (SPU2) which is a dual channel signal conditioner. The AET5500 digital AE module has two to five modules that are essential for AE monitoring and three others for more specialized testing.

The Ringdown counter/Event duration module (REM) counts threshold crossings and event duration of these threshold crossings. The REM determines event duration by counting the pulses of an event duration clock signal. The operator can select the clock period to time the events. The AET5500 system clocks are from a basic clock period of 125ns (8MHz). The periods for the event duration rise time and location clocks are 125, 250, 500, 1000, 2000, 4000 8000 and 16000ns. Once the SPU detects a threshold event, the REM starts counting the pulses of the event duration (ED) clock at a basic rate of 8MHz (125ns). The ringdown and event duration counters are 12 bits long (a maximum count of 4095 per event). The ED clock also sets a "timeout period" for the ED. The system waits 256 ED clock pulses after the last ringdown count drops below the threshold before signalling the end of the event.

The ED clock period needs to be carefully chosen. If REM event durations count is longer than 3,839 counts, the counter will overflow and read zero because of the 256 count 'timeout' period ($3,840 + 256 = 4096$) overflow). This means that the longest measurable event is 3,839 events. The computer will display the count in microseconds. If the clock period is set to 125ns, the longest measurable event is 479.9 μ S. To achieve the best ED data a clock period of ED that provides the shortest timeout period but yet gives ED values less than 65,520 μ S is desirable.

The amplitude/rise time module (ARM) measures the peak amplitude time of the the peak amplitude. The processor uses this data to compute the positive AE signal slope. The input to the ARM is the preamplifier output signal and is not affected by SPU gain adjustments.

The time difference module (TDM) measures the difference in time of arrival of an AE event at two or more different sensors. One TDM is required for linear determination of

an AE source, and two TDMs are required for planar location. The difference in time of arrival of the AE signal at two different sensors is referred to as Delta T or DT. These DT data is processed by the microcomputer to arrive at a location for the AE source event.

A simplistic explanation of what is occurring with the location feature of the AET5500 is that the first sensor to detect an event starts the location clock (a counter) and the next hit sensor stops the clock. To obtain location data at least two sensors need to be connected together in a configurations termed an array. The TDM's in these array begin data collecting sequences in two manners:

- The TDM receives an AE event
- The TDM receives a signal from another TDM in the array

When a TDM receives a signal from the first sensor in the array, it sends a pulse to the other

TDM's in the array and stops its own DT clock. Its DT counter will read zero since it never started. The TDM then inputs its DT count of zero to the processor. Once a TDM receives a signal from another TDM in the array, it will start its DT counter and will stop the counter when it receives a sensor hit. This will give a non-zero DT count to the processor. The non-zero DT count is the difference in arrival times of the AE event at different sensors. When more than two sensors are connected in an array, the order in which the sensors are struck are determined by the rank order of their DT counts. The sensor with a DT count of zero is first struck, second has the lowest non-zero counts and so forth.

Before testing can commence a sensor array must be calibrated. This calibration consists of determining the maximum DT for each pair of sensors for an artificially applied AE source. This artificial source frequently is the breaking of 0.5 mm pencil lead on the test piece surface. An operator specifies certain parameters for the tests and using these specifications (threshold voltage, locator clock period, etc.) develops a table of values of Maximum DT's the processor uses to establish the location of AE events occurring in the test piece. Data about the test can be displayed by showing the order sensors activated and the regions these AE activations occurred. Another form of tabular screen output is to show sensor order and AT values.

2.3. ACOUSTIC EMISSION PARAMETERS

Various studies have been conducted that related material characteristics to different AE responses. Studies by Berndt, Almond, Ono and others [1,2,3,6,7 8,9,10] have correlated

microstructural damage with the count rate. Many different types of cracking phenomena are involved in the total count rate. The number of pores, preexisting microcracks, number of cracks, and their growth rate all affect the count rate [1]. A large count rate could be dependent upon a large growth of a few cracks or conversely, small growth of many small cracks. Either condition could give the same count rate. It is also pointed out, that there is a difference between the “extent of cracking” and “cracking mechanisms”. The extent of cracking can be indicated by the total event count [1,8]. The total count, however, can be affected by the acoustic properties and the physical configuration of the test specimen[8]. This becomes influential during source location of acoustic emission configurations.

To investigate mechanisms of cracking, one needs to examine at the count rate and distribution[8] The count rate by virtual of if it is a monomodal plot or bimodal plot can indicate if one predominate mechanism is at work or if a different mechanism begins to come into operation overshadowing the initial mechanism [11].

The AE signal characteristics can be plotted vs time, strain or some other useful parameter. Along with event counts, other acoustic emission parameters are commonly used: energy, peak amplitude, rise time and event duration [8]. Of these parameters, the distribution of peak amplitude has been reported to yield the most information about cracking mechanisms and was found to be a useful tool in this study for investigating fracture mechanisms [2,12,13,14]. It was found during this study that an energy distribution yielded some insight but the extent of the usefulness of this information was not fully investigated [8,15]. Rise time and event duration have not been thoroughly investigated.

Energy is a measurement of the area under the rectified signal envelope. This measurement is often preferred over counts due to this parameters sensitivity to amplitude and duration and less sensitivity to operating frequency and threshold voltage. Then energy does not have a unit denotation. The AET 5500 computes energy from the formula: Energy = Peak Amplitude + 10LOG(EVENT DURATION).

2.4. BOILER TUBE STRAIN CALIBRATION

Strain gages were mounted on a bare tube prepared to the dimensional parameters of the tubes that were to be coated. The strain gages were mounted as shown in Figs.1. Strain and

AE activity were monitored during 3 pressurization runs up to 13,000 psi. The positions for the coatings were then made based upon this strain data and the needs of the AE source location array. The strain gages used for strain testing were biaxial general purpose CEA gages from Micro-measurements Group. Uniaxial general purpose CEA gages were used for strain monitoring during testing of coatings

2.5. MULTIPLE TESTING

The decision to perform multiple tests introduced the a question of the feasibility of source location and concern about possible emission paths from source to sensor [8,14] One of the more difficult configurations to perform source location studies on is a water-filled pipe. There are many possible paths for an emission to take. Three very likely paths are a point-to-point path, a spiralling of the path about the tube and a water-borne path. These different paths affect the time it takes for the emission to reach the sensor which in turn affects the accuracy of the source location computation.

2.6. KAISER EFFECT

A phenomena related to AE, “the Kaiser Effect” [2,8], played a large part in this test configuration . If a specimen is loaded up to some certain value, unloaded and then loaded again, emissions will be emitted on the initial loading and will not begin again until the reloading of the specimen approaches where the initial loading ended. The incorporation of this phenomena is detailed in the procedures portion of this study.

3. EXPERIMENTAL PROCEDURE

3.1. MATERIALS

The thermal-sprayed coating materials used for this study were an aluminum oxide (Metco 101), a stainless steel (420) and an experimental molybdenum alloy referred to as Mo-Fe blend coating. The test matrix for the materials is shown in Table I. The coatings were sprayed onto 3 inch OD AISI 1026 boiler tubes which had 0.188 inch wall thickness.

3.2. TEST SPECIMEN PREPARATION

Before coating, each boiler tube was cut to a 3 foot length. A 1.5 inch thick plug was welded onto the ends of the tubes to cap them and a pipe fitting welded into one end (Figure 3). The tubes (bare of any coating) were then pressurized to a maximum pressure of 13,000 psi. This step served the dual purpose of testing welds for leakage and minimizing of anomalous AE sources from the substrate material.

The tubes were then sprayed. Each tube was then sprayed with 3 separate coatings of the same material, each with a different thickness. On any one particular tube there was a coating of the same material sprayed at three separate sections of the tube, with each section differing by thickness and position on the tube. A total of ten tubes were sprayed. Nine tubes were strained and a tenth was used as an unstrained reference for metallographic work. The 10th tube was sprayed with each type of material but in only a single thickness. The coating placement and profile are shown in Figures 2 - 4.

3.3. MONITORING and RECORDING EQUIPMENT

The equipment used for monitoring strain and AE responses during testing included:

1. Hartford Steam Boiler Technology Model 5500 (HSBT 5500) Acoustic Emission System. The system consists of a signal processing unit, piezoelectric sensors, signal amplifier boxes and cables (Figure 5).

2. HP-386 model Vectra P.C. for data collecting, recording and displaying.

3. National Forge Isostatic/Hydraulic Pressure System for hydrostatically pressurizing the boiler tubes.

4. A specialized rack for restraining the boiler tube during pressurization in the environmental test chamber. The rack had rubber padding mounted in places where contact was made between the tube and the rack. This precaution allowed the tube to be isolated from environmental vibrations being transmitted to the tube by the rack.

5. Strain amplifier for the strain gages.

3.4. PRESSURE TESTING

In preparation for testing, the tubes were all mounted with a uniaxial strain gage positioned close to the edge of coating position #2, towards the pipe, on bare metal. The gage was used to measure the hoop strain. The tube was then filled with tap water, mounted in a test rack and the AE sensors mounted (Figures 5 and 6).

HSBT silicone-based gel grease SC-4 was used as the mounting medium and duct tape used to hold the sensors in position. The sensors were then connected to the AE monitoring system while the rack was accessible for calibrating the source location array. The tube rested on rubber pads on the test rack for isolation from the environmental noise sources. The breaking of 0.3mm Pentel pencil lead extended from a mechanical pencil was used as the artificial source for calibration purposes.

After calibration was completed the sensors were disconnected from the monitoring equipment and the rack was moved inside the environmental chamber and the tube was connected to the pressurization system. The sensors and strain gage were connected to the AE monitoring system along with a pressure signal from the pressurization system. At this time the strain gage bridge was balanced and the AE sensors were checked to see if they were monitoring correctly. A small amount of pressure was then applied to check for connection leaks, to correct pressure signal, and to check for air in the hydraulic lines.

The pressure was then backed off to zero and then reapplied at an approximate rate of 1000 psi per minute until a maximum pressure of 13,000 psi or some predetermined pressure had been achieved. The predetermined pressure were decided upon based on when AE activity was expected to begin. Those particular tubes would then be pressurized to just below this point or just after AE activity began. The tube was then de-pressurized and disconnected from the systems. The AE, strain and pressure data were stored on the P.C. for later data analysis.

3.5. DYE PENETRANT TESTS

Dye penetrant tests were performed on all coatings after straining and also on the unstrained coatings. This was done to detect any surface cracking and to determine its extent. Approximately 2/3 to 3/4 of the coating surface area was masked off with tape and paper from dye penetrant so as not to interfere with later metallographic work. A more detailed explanation of the procedure used for dye penetrant testing is covered in Appendix 1.

3.6. METALLOGRAPHY

Care was taken during sectioning so as not to further induce any more damage to the coating microstructures. The coatings sections were separated from each other by a bandsaw while mounted in a special fixture (Figure 7). Each coating sectioned was then mounted in a three-jaw chuck on a lathe. Enough bare metal was left during the bandsaw operation to give the chuck room to grip an area without coating and a plug was placed inside the tube so that the tube would not deform while being held.

A precision grinder with an abrasive cut-off blade was mounted on the tool-post of the lathe. The precision grinder was then hand-fed into the coating while the tube was being rotated to cut through the coating. Two grooves were cut through the coating the substrate

material, 3/4 inch apart from each other. These grooves were wide enough to accommodate the abrasive cut-off blade of a high speed cut-off saw. (Figure 8).

The high-speed cutoff wheel was needed to finish cutting the tube. The lathe-cutoff saw combination saved some time and kept stress on the coating itself lower than if the high-speed saw has been used exclusively. A specimen for mounting was then cut from the ring with a low-speed abrasive cut-off wheel. During all cutting operations the coatings were fully flooded with coolant application.

The specimens were cold-mounted under a vacuum with epoxide resin (EPOFIX). This is the recommended procedure for thermal-sprayed coatings for impregnating surface pores and cracks [17-25]. Specimens were taken in the longitudinal and circumferential directions, and prepared according to their material type. This generally was a 5 step operation and more details are given in Appendix II. An important factor in achieving good results with these thermal-sprayed coatings was the use of grinding paper that showed a close tolerance in the size of the grit particles used in the paper. The specimens were then examined optically with a Nikon Epiphot microscope and a Zeiss DSM-960 Scanning Electron Microscope .

3.7. SCANNING ELECTRON MICROSCOPE

Scanning Electron Microscope work was done on a Zeiss DSM-960 microscope at 20kV. Specimens were sputtered with about 200 microns of Pd-Au to alleviate charging problems.

4. RESULTS

4.1. Background Strain Analysis Results

Calibration of the strain field that the coatings experience during testing was essential. Initial strain analysis was carried out on a tube pressurized to 6,000psi, which was well within the elastic limit of the tube material. The results of this test are shown in Figure 9. The results of the initial tube testing were encouraging, and work began on a test configuration that would test multiple coatings during a single test run. The multiple coating approach allowed triplicate tests to be conducted during a single test run. In order to insure that the end-caps would not produce anomalous strain effects, generating spurious A.E. along the length of the tube, another strain analysis was undertaken. During this strain analysis, a tube (void of coating) was pressurized to 13,000psi, depressurized and then repressurized to 13,000 psi. The values for strain at different positions along the tube are shown in Figures 10a, and 10b. It can be seen that there is a difference of $.50\mu\epsilon$ between the middle and outermost gage readings. Subsequent pressurization produced a closer harmony in strain readings to a value of $.1\mu\epsilon$ between the middle and outer positions.

4.2. Coating Profile

The coating as-sprayed edge profiles did not strictly conform to Figure 4. An edge was produced, due to a masking procedure, and there was concern that these edges would serve as crack initiation sites. Neither subsequent source location nor dye penetrant tests gave clear unambiguous results indicating whether cracking was initially occurring at the edges.

4.3. Coating Placement

Based on the strain data, no coatings were located closer than 7 inches from the end-caps. This criteria along with the placement requirements of the sensors and strain gage resulted in the coating placements as shown in Figure 2.

4.4. Non-Destructive Inspection Results

4.4.1. Dye Penetrant Tests

Dye penetrant testing showed that surface cracking occurred on some Al_2O_3 and Fe-Mo blend coatings. The stainless steel coatings did not exhibit any obvious indications of cracking. For the aluminum oxide coatings on the tubes pressurized to 13,000 psi, the thinnest coatings sections showed faint signs of cracking. The thickest two coating sections on all the maximum pressurized tubes showed definite indications of extensive cracking. The cracking seemed to extend from one edge and extend in a fairly straight line to the other edge or stop if it approached the leading edge of a cracking travelling from the opposite edge. These longitudinal (parallel to the long axis of the tube) cracks girded the coating circumferentially approximately 1/4" from each other (Figures 15, 16, 17). For the aluminum oxide coatings on the tube pressurized to 8840 psi, only the thickest coating showed some evidence of cracking. Figure 18 shows that cracking began but did not extend the width of the coating. Cracks can be seen near the top of the middle portion of the coating and in a central location. The coatings on the unstrained tube showed no evidence of surface cracking (Figure 19).

It was difficult to interpret the stainless steel coating results. The coatings would uniformly exhibit a widespread indicator color but there were no clear indications of distinct surface cracking (Figures 20-23). All three coating thicknesses of the Fe-Mo blend coatings showed evidence of cracking on the tubes strained to 13,000 psi (Figures 24-26). The cracks ran in the longitudinal direction but not in quite as linear fashion as the Al_2O_3 cracks. These cracks girded the coatings in a circumferentially. The cracks in the thickest section had sustained additional cracking in the circumferential direction. The circumferential cracks served as a terminator for two or three longitudinal cracks. The net effect was a crazing appearance for the network of surface cracks. None of the Fe-Mo blend coatings on the tube pressurized to 6,000 psi showed any clear indications that surface cracking had occurred (Figures 29-31).

4.4.2. Acoustic Emission Tests

4.4.2.1. Aluminum Oxide Coatings

The source location investigation showed mixed results (Figures 32, 33, 34). For the Al_2O_3 coatings on tubes pressurized to 13,000 psi, events were recorded as occurring in

the areas of the coatings but in other areas no events were recorded where cracking had clearly occurred. The .015 coating exhibited no indications of cracking occurring. For the .030 thickness, two of the tests indicated events but the test designated ALO3 did not show any events as occurring on the source location distribution plot at that location. All tests indicated cracking occurring for the .045 coatings. On the test for the tube pressurized to only 8840 psi, some events were detected but none of the events were useful for source location purposes.

A check of the A.E. statistics for these tests show that there was scatter in how many events were accepted but the scatter was within a magnitude in value (Tables IV – V) The acceptable events ranged from around 1500 to 2650 in value. None of the parameter ranges were overwhelmed. In all of the tests a number of events were rejected because they did not occur in the region of interest or because the time of arrival of the emission exceeded the calibrated arrival time. In all tests the criteria that caused the most rejected events was the order of arrival of the emission. The percentage of events accept to the number of events rejected was between 16.5% to 19 % for this coating material.

Out of the three coating sets pressurized to a maximum value , one set of coatings seemed to have quieter and fewer emissions than the other tests. The test designated ALO2 exhibited this feature in the distribution of events plot and the test ALO4 showed something occurring at a low strain and then no more activity until the thickest coating began cracking. The distribution of events by peak amplitude for all the tests showed a sharp rise to a maximum peak amplitude from the low amplitude side of the plot. On the high side of the plot the values fall off more slowly in what appears to be a type of exponential decay.

The range for peak amplitude values is from about 30 to 58 dB (Figure 36, 37). The bulk of the activity seemed to occur around the 38dB range with two of the tests shifted slightly in value to higher dBs. The Log of Cumulative Distribution of Events by Peak Amplitude shows the shift to higher peak amplitudes but the slopes were similar to each other for this coating material (Figure 37).

There also appears to be another smaller peak of activity for two of the tests around the 48–50dB area. This type of plot seems to shift towards higher average peak amplitudes as the amount of accepted AE activity increases. The distribution of events by energy plots did not show this shift that significantly but the range in energy values became noticeably smaller as the level of AE activity dropped (Figure 38).

On all the distribution of events by energy for all materials and thicknesses a gap appears in the plot around the 43 location on the plots (Figure 38). The majority of emissions had energies around the 59–60 units. The mean energy per event plotted against strain for two of the coatings showed a tendency to increase by the end of the test. Another coating section showed a mean energy increase at the beginning of the onset of emissions (Figure 40).

Overall the plots exhibited fairly uniform values for mean energy per event. The energy vs strain plots show a difference in how each of the three coatings began to crack. After coating ALO2 began cracking, it maintained a fairly level amount of energy even towards the end of the test. Coating ALO3 began cracking at a fairly low energy value and then began a moderate rise in value. The coating ALO4 behaved very differently. It generated emissions (not in the .045 section) early on in the test. When the .045 coating began cracking, it started off at higher energies than any of the other coatings, dropped off a bit and then began a rise again up to the same level of energy values as ALO3 for that strain value. This trend for an energy increase towards the end of the test shows up in the Total Energy vs Strain plots as a change in the slopes of the plots. The slopes in the plots increased as the number of events accepted increased (Figure 39). The approximate slopes of the three tests are shown in table VII. This type of coating began emitting emissions within a strain range of $2000\mu\epsilon$ to $2100\mu\epsilon$. It did not necessarily follow that the specimen that began emitting at the lowest strain had the steepest total energy vs strain plot or emitted most of the detectable and acceptable data.

4.4.2.2. Stainless Steel Coatings

The feature that stands out the most on the source location distribution plots is the lack of distinct division between coating sections other than an area of much less emissions compared to areas of more emissions. When the distribution plots are viewed relative to the coating section positions, there was a tendency for increased emissions towards the ends of the coating sections. The test designated SS1 resulted in the least amount of emissions for the thinnest coating. The test SS3 was by far the noisiest of all the tests. Its amount of accepted and rejected amounts were much greater than the other tests.

The criteria by which most emissions were disqualified was the order of arrival at sensors in the array. An examination of the raw data showed that many emissions were too weak to activate more than one sensor in the array. The plots of the distribution of events by peak amplitude had much the same range as the aluminum oxide coatings, about 32dB to 58dB

for all coating thicknesses (Figures 41, 42). These plots show a sharp rise to an area of maximum events and then an exponential decrease as the amplitude values increase past this peak area. This peak area generally, with a few exceptions, has an appearance of a plateau more than a distinct peak. The peak of the plot appeared to be generally around the 38 dB value. Some weighted slightly towards higher values and others towards lower values. The plots of many of the sets of coatings appear to have an exponential decay in peak amplitude values that is lower than the aluminum oxide coating.

The test SS2 shows a different distribution shape in its plot from the most of the other tests. This test shows a gradual rise to a maximum and then a gradual decay for amplitudes in the higher range and the peak seems more shifted above the average 38 dB. The majority of the plots had a bimodal appearance.

The coating sets for SS3 displayed a more peaked appearance in its plots than the other tests. The energy range for the thinnest coatings was 30 – 83 units and for the other thicknesses the range was 30 – 90 units (Figures 44, 45, 46). The energy vs strain plots show that there was a trend for the thicker coatings to begin emitting significant noise at a lower strain than the thinnest coatings.

There seemed to be an increase in energy as the strain increased. The plots show that a burst of energy would occur and then drop nearly to zero when another burst would occur. In other words, the emissions were occurring in bursts and not continuously. The approximate slopes for the plots of the total energy show a thickness effect (Table VII). The general trend was for increasing slope as the coating thickened (Figure 32–34). The greatest change in slope occurred between the thinnest coatings and the other thicknesses.

Test SS3 stood out as having the steepest slopes in all of the thickness categories. The steepest slope of this test was comparable to the slopes of the aluminum oxide plots.

A comparison of the Log Cumulative Distributions of Events by Peak Amplitude between the stainless steel and the Al_2O_3 did not show any obvious differences, particularly for the thickest coating (Figures 50, 51, 52).

4.4.2.3. Molybdenum–Iron Blend Coating

There was not much differentiation between coating sections for the source location plot of the coatings on the tube pressurized to 13,000 psi. Three general areas of activity could

be detected with the greatest amount of activity corresponding to the coated areas of the tube. The coating set pressurized to 7,000psi showed a distribution of events by source location that corresponded with coating section location and the location of sensors in the array.

For the tube pressurized to 13,000 psi, a number of events were rejected based upon the fact that they overwhelmed the event duration counter. None of the other materials had events rejected based upon this criteria. An examination of the raw data revealed that all three coating thicknesses would from time to time produce an event that could not be measured by the event duration and ringdown count counter. This result was demonstrated by the ringdown count and event duration count as having exceeded the counter. That is a count of 4095 and a duration of 65302 μ s with no other AE parametric data being recorded.

The coating sets on the tube pressurized only to 6000 psi did not have these large emissions. The maximumally strained coating set also had a higher number of events rejected based upon the DT than other categories compared with other coatings.

This material also had a higher number of events rejected based upon the DT between the first hit and second hit sensors in the array. The plots of the distributions of events by peak amplitude for the maximum strained coatings showed a range in values from 32dB to 78dB (Figures 53, 54, 55).

The thickest coating showed a number of events occurring at the 78dB value and above the 63dB range.

The range for the minimally pressurized coating set was from around 28dB to 63 dB, with an average or peak occurrence around the 35–37dB range. The maximum strained coatings seemed to have peaks around the 40–43dB range with the peak appearing to move towards higher peak amplitudes as the coating thickness increased.

The Distribution of Events by Energy for the maximum strained coatings showed a range from 30 to 125. The thickest coating showed a number of very energetic events occurring in the 100+ range. These plots displayed a distinct peak in values as with the aluminum oxide coatings (Figure 56, 57,). The average for the plots seemed to be around the 80 range with the thickest coating having a somewhat higher average. The minimally strained

middle thickness coating was the only thickness of that test set to show any kind of trend. At this level of strain the average energy of the events appeared to be around 60.

The Log of Cumulative Distribution of Emissions by Peak Amplitude showed some steps in the plot for the middle and thickest coatings sections. These steps occurred around the 58–70 dB range (Figures 59, 60). The slopes of the Total energy vs Strain all showed a marked bimodal appearance for the maximally strained Fe–Mo blend coatings. The .020 inch and .030 inch coatings bent convexly to the horizontal axis while the thickest coating displayed a concave appearance to the same axis. The slopes of each part of the Total Energy vs Strain plots can be seen in table VII. (Figures 61 – 63).

4.5. MICROSTRUCTURE

4.5.1. Aluminum Oxide

One set of AL_2O_3 strained coatings and the unstrained coating were sectioned for this study. An examination of the unstrained AL_2O_3 coating showed a fairly homogeneous microstructure with some inclusions that generally had a narrow form (Figure 64). The material had pores and much micro-cracking. None of the micro-cracks were connected enough to form a surface to substrate crack. When the .015 inch coating (maximum strained) was examined, a crack was barely discernable under SEM examination. The crack can be seen in Figure 65 to begin on the right and work its way to the left in the picture (substrate side of picture).

Cracks in the .030" and .045" coatings (maximum strained) were more readily visible (Figure 66). Figures 65, 66 show multiple micro-crack paths that eventually emerge into a large continuous crack.

A close up of a crack in Figure 67 shows the right side of the crack has shifted down relative to the left portion and some grinding seems to occurred at the top of the round spot in the middle of the photograph. Figure 68 shows an optical micrograph of a through crack in a coating. The unstrained coating did not show any cracking

4.5.2. Stainless Steel

No cracks extending from surface to coating substrate interface were found upon examining the microstructure with optical or SEM means. The microstructures of the stainless steel coatings show a highly lamellar form. There are unmolten particles, pores, voids and layers of lamellae.

Areas of deformation that had the appearance of delamination between the lamellae were apparent. Figure 69 shows the unstrained coating as having some of this feature, but not to the extent as in the strained coating as shown in Figure 70. The top halves of these photographs are SEM and the bottom halves are Back-Scatter Emission (BSE)- topographical.

There appeared to be a level of correspondence of the level of deformation with the slope of the Total Energy vs Strain plots. The plot of Figure 71 had a steeper slope than the slope of the coating in Figure 72. This trend held true for most of the coatings. Figure 73 had the steepest slope of all the stainless steel coatings and appears to have the deepest level of deformation into the coating.

The optical microscope showed the mixed nature of these coatings however the Scanning Electron Microscope and Back Scattered Emissions (BSE)–topographical techniques were needed to bring out the delamination features of the coatings. Some very dark areas observed in the optical mode thought to be delamination were proven to be just very dark lamella or a dark phase between lamellae. Other similar looking areas turned out to be areas with topography consistent with a delamination effect.

4.5.3. Molybdenum–Iron Blend Coating

The microstructure of the Fe–Mo blend coatings was very complex. Figures 81 and 82 show that various compositions are present in a lamellar form. An EDX analysis of some of these phases showed that the phases tended to have either an overwhelming amount of Molybdenum or else a large concentration of Nickel (Figures 92, 93).

The unstrained coatings showed areas of inter–phasal cracking but no critical cracks or long portions of a crack (Figures 81, 82, 83). The coating sprayed in an Argon atmosphere seemed to have a small increase in this minor cracking compared to the coating sprayed in a standard atmosphere. All of the coatings pressurized to 13,000 psi exhibited critical cracking. The crack path was not as linear as the Al_2O_3 coating cracks. The Fe–Mo blend coating cracks had a tendency to zig–zag through the coating to the substrate. In the two thinnest coatings, the cracks would stop and then continue a small, horizontal distance away (Figure 84).

A close up of an arrested crack area is shown in Figure 85. Figure 86 shows a cross–section in a normal direction (circumferential) from Figures 84 and 85 (longitudinal).

No major cracking or delamination were evident. The thickest coating also exhibited this zig-zag effect but without as many of the crack arrest and start portions (Figure 87). Cracks in the circumferential direction were evident only for the thickest coating (Figure 88). All coatings that had cracking had delamination in areas adjacent to the crack path. The minimally strained coating set showed signs of cracking but no critical cracks were observed (Figures 89, 90, 91).

5. DISCUSSION

5.1. INTRODUCTION

The test method described in this body of work provided information on the variety of coating behavior that occurred under uniform strain conditions.

This method indicated changes in surface crack propagation patterns, and detected a thickness effect for all coating types. Coatings of like thicknesses could be differentiated from each other based upon different aspects of their AE signals. The tests showed that aluminum oxide and Mo–Fe blend coatings are more susceptible to cracking than the stainless steel coatings. The source location feature of AE monitoring was instrumental in detecting these thickness effects.

5.2. SOURCE LOCATION

The aluminum oxide and the stainless steel coatings showed the most marked thickness effect in regards to source location. Other AE features were needed to discern a thickness effect for the Mo–Fe blend coatings if strained to a maximum. One set of Mo–Fe blend coatings that was strained just until AE events were beginning to be detected showed a marked thickness effect. The aluminum oxide coatings would typically show a distinct region of emissions corresponding to the position of the coating on the tube. The Mo–Fe blend coatings had less correspondence to position in their plots, but the areas of highest emission events were in regions of full-thickness coating positions. The stainless steel coatings showed a continuous region of emissions for the whole length of the tube. It was hard to discern, from the source location plot, where the corresponding positions of the coatings would be on the tube. The greatest distinction for stainless steel was that one region emitted many less events than another region. The quieter region typically corresponded with the thinnest coating section and the noisier region corresponded roughly with the positions of the other two coating thicknesses.

These differences in coating responses to AE source location suggests that a selection in coating type may result in a need to limit the number of coating sections deposited on one tube if the purpose of the test were to investigate emission sources that were occurring towards the edges of the coating section.

5.3. KAISER EFFECT

The utilization of the Kaiser effect for eliminating emissions originating from the substrate material was successful. Figure 12 shows a multitude of signals occurring during the initial pressurization to 13,000 psi. Subsequent pressurizations to 13,000 psi showed a lack of emission sources within the parameters of this test when subsequent pressurization to 13,000 psi was done. A number of these subsequent pressurizations were performed to determine if emissions returned within a certain time interval. Up to a week before the tubes were sprayed (this was 8 months after the initial pressurization) a tube was pressurized and no significant emissions for source location purposes were recorded. This clearing of emissions effect was not as evident in Figures 33 and 34 for the Mo-Fe blend and stainless steel coatings as for the aluminum oxide coating due to the less exact placement of the emission sources.

By making use of the Kaiser effect to rid the tube material of background noise, the maximum strain value was reduced from what could be obtained from an initial 13,000 psi. pressurization. A comparison of Figure 10a with Figure 10b shows a drop from a strain of 3000–3500 $\mu\epsilon$ to about 2500 $\mu\epsilon$ for a subsequent pressurization.

The strain at maximum pressure was large enough to crack the more brittle coatings such as Al_2O_3 and Mo-Fe blend, but no evidence of cracking could be discerned for the stainless steel coatings. The possibility of rupturing the boiler tube limited attempts to reach a strain value large enough to cause cracking in the stainless steel coatings. During preliminary testing, one tube was ruptured upon its initial pressurized to 13,500 psi.

5.4. Aluminum Oxide Coating

The thickest coating section of each Al_2O_3 test set had similar plot profiles. In Figure 32 a few emissions are shown located in a zone that was bare of coating material. These zones are shown as being filled with emission source sites for the other two coating material types. This raises the question whether or not the base material had really been cleared of

emission sources. This can be answered by comparing source location figures. If the tubes had not been cleared and the emissions showing up on the plots in coating free zones arose from extraneous sources, the aluminum oxide plots would have also shown emission sources throughout the extent of the tube. Figure 32 shows that this does not happen and so it can be assumed that the majority of signals are arising due to some action taking place in the coatings; notwithstanding their apparent location. The distribution of events by location plots do show definite thickness effects for the aluminum oxide. What is shown is that the thickest coating section was the only section that typically had significant amounts of emissions recorded.

An analysis of the raw data did not show evidence that placeable emissions were occurring in the .030" and .015" thick coating sets. The fact that cracking had occurred though, is shown by Figures 32, 33, and 34 and the dye penetrant tests results.

The dye penetrant tests became more distinct as the coating thicknesses increased as if the dye could penetrate the cracks in the thicker coatings more readily than the .015" coating. Cracks were barely discernable by the unaided eye and not by photograph for the .015" coating. The .030" and .045" coatings were more easily detected by the unaided eye and recorded by photographic means.

Microscopic analysis of the unstrained coating specimen did not show any signs of connected (surface to substrate) cracking. As the coatings thickness for maximum strained sets increased, it became easier to visually locate the cracks while observing them under magnification. It is possible that preexisting microcracks were coalescing and as the thickness increased that these cracks then dilated. Residual stresses in the coatings could be a factor in this effect.

The lack of detected AE events was puzzling. Crack coalescence would be a low energy process, so low that AE events were not being detected. Another possibility could be that the events detected were crack edge friction as crack edges moved against each other in the thicker coatings. Some shifting of crack edges relative to each other can be seen in Fig 67.

At the threshold voltage of 1.0V and a Signal Processing Unit (SPU) gain of 3.5 HI, the sensitivity of the lower peak amplitude threshold is 29dB. A natural assumption would be to drop the threshold voltage or raise the gain of the SPU to "find" the missing data. A look

at Figure 32 indicates that this may not be a solution. The plot shows a fairly symmetrical plot about the 38dB position. This indicates that not much is occurring at lower amplitudes and there is a probability not much could be found out unless there was a second peak of amplitude events occurring in that lower region indicating that events of a different nature from what is now being recorded were taking place.

A look at the raw data however indicates that lowering the threshold may prove useful. Many events were activating only one sensor in the array, and the activity is very low in counts and duration, even though the peak amplitude is reasonable, but on the low side (around 34 dB).

Another possibility is usage of a linear test array instead of a planar array sensor set-up. A planar array would be more able to deal with spiraled and water-borne signals which could be exciting sensors at times other than a straight path from source to the sensor and throwing off the delta T times for location purposes [8,14].

Reading through the raw data shows that the E.D. clock period may be too long for this type of coating. The clock was set at 16,000ns to accommodate the Mo-Fe blend coating but an E.D. clock period of 2,000ns would be quite adequate for Al_2O_3 coatings. The raw data also reveals that all sensors were receiving data but some sensors were not being activated very frequently which again shows that emissions were not being detected and not just being rejected because they didn't fit the test array parameters.

To answer the question of where the "missing" data is, it probably would be advisable to test one coating of less than .045" thickness with the same test configuration and record the actual signal with a frequency analyzer to determine if the test parameters (E.D. clock, threshold voltage, etc.) were adequate or even if the signal was being detected by the sensor. A broadband sensor would probably be appropriate for this test.

It would be very useful to be able to examine the strained microstructure of the rest of the Al_2O_3 coating sets to see if any differences were apparent and if the minimally strained coating set showed evidence of connected surface to substrate cracking or not.

5.5. Stainless Steel

The stainless steel thickness differences, as a rule, showed up between the thinnest section and the other two thicker sections (Figure 16) . Between the two thickest sections, no effect

was discernible. The one coating set designated SS3 stood out from the other coating sets as having greater amounts of emissions for all three coating sections.

As the results show, in order to test stainless steel to cracking, a change in test methodology will be needed such as a change in substrate material. It is known from preliminary testing that stainless steel coatings can be cracked, but that this is in the plastic deformation zone (an initial pressurization) of unstrained boiler tubes.

In a paper by Pollack [14], he states that it is difficult to locate the source of low energy emissions. If the testing of the stainless steel coatings could have produced some cracking, a better sense of source location was expected to have been produced then the early pre-cracking behavior that was achieved. This early pre-cracking behavior exhibited low energies of relatively long event durations compared to the Al_2O_3 coatings.

Figure 69 shows how the unstrained microstructure appears. When this figure is compared with Figures 70 and 71, there is a noticeable area of distortion in the upper portions of the coatings that is not as widely present in the unstrained coating. The width of this area increases as the thickness of the coatings increase. There was also a noticeable increase of distorted area in the coatings from the test SS3 compared to the other coatings. This distorted area had a tendency to extend at intervals deeper into the material than at other intervals. It is thought that these distorted areas are regions of delamination. BSE topography work shows that these areas have some depth to them as if they were cracks or separation between lamella. Many regions in SEM and optical observation appeared dark like cracks but BSE work showed that only some of those dark areas had some depth. It is hypothesized that the areas of deeper occurring (from surface to substrate) delamination were the areas that would be the most likely to experience cracking, or ductile tearing, if enough strain could have been gained. This carried over into the data received in that the emissions plots indicated that the coatings undergoing damage at a much higher rate than the other coatings exhibited more and deeper regions of distortion than other, quieter coating sets. It was anticipated that since the Al_2O_3 peak amplitude signature and the stainless steel's appeared much the same that a layer of oxides was present between lamella, and a low energy, brittle deformation was taking place.

An examination of the raw data showed that these coatings had a tendency towards longer event durations than the Al_2O_3 coatings. An E. D. clock period of 4000 ns would be adequate for this type of material. There is some evidence of wrap-around signals with this

material in the deltaT times . Some of the delta T times are quite long as if the signal took an indirect path before activating a sensor in the test array.

The total energy vs strain plots were the most readily usable method for discerning the Al_2O_3 coating from the stainless steel coatings (same thicknesses) . When all thicknesses were compared to each other, the more noisy stainless steel coatings had slopes similar to the quieter Al_2O_3 coatings.

Overall, the stainless steel coatings were very similar in their responses to the Al_2O_3 except for the total energy slopes and at what strain significant emissions began. If a more detailed statistical analysis of the peak amplitudes could have been done a more discernible difference may have been achieved. Papers by Almond and Pollock [2,13] suggest that finding the b-factor of a power-law amplitude distribution or a chi -square analysis can yield information about crack processes. Such a study was outside the scope of this thesis. This type of undertaking would have necessitated developing a program that would convert the binary data of the AET 5500 software into an ASCII format to transfer the data for more sophisticated analysis. A partial attempt was made but was not in a complete enough form to be used for this investigation. Such a statistical analysis was made between alumina and molybdenum coatings with reported success[2].

5.6. Molybdenum–Iron Blend Coating

The Mo–Fe blend coating showed some sense of emission source location but with some misplacement. There was a trend for more emissions to be located towards the centers of areas between sensors than towards the ends of the three areas. This corresponds with the thickest portion of the coating profiles being located centrally between sensors.

The Mo–Fe blend coating exhibited behavior that was distinctly different from the Al_2O_3 and the stainless steel coatings. This material was much noisier, it emitted many more events of higher energy and amplitude. It was not very hard to discern when one was viewing data from a Mo–Fe blend coating test.

The distribution of events by source location did not show any obvious differences between thicknesses. The thickest coating showed one area that had a slight rise in emission sources compared to the rest of thicknesses. The plots that showed the greatest difference between thicknesses were the total energy vs. strain. The two thinnest coatings were quite similar to each other in their profile. The curves for all thicknesses were bimodal in appearance.

This bimodal appearance indicates that more than one type of emission source type was in operation. The thinnest coatings plots had a slope discontinuity that bent concavely to the strain axis. The thickest coating had a discontinuity that bent in a convex fashion to the strain axis. The log of cumulative distribution of events by peak amplitude also showed this difference between the thicknesses. The thinner coatings had a fairly linear slope, less steep than the Al_2O_3 or stainless steel and exhibited a small series of steps near the upper peak amplitudes. The thickest coating however exhibited a step about two-thirds down its slope and then continued on for a bit with no change then ended in a large cutoff at the largest peak amplitude value as if an upper limit in peak amplitude had been reached. There was a correlation between these different AE behaviors in the appearances of the strained microstructure and the dye penetrant test results. The dye penetrant tests showed that the thinner coatings had longitudinal surface cracking in a wavy pattern, more so on the middle thickness than the thinnest. The thickest section also had wavy longitudinal surface cracks but there were also present short circumferential cracks that would intersect the longitudinal cracks and then intersected and terminated each other. This gave the thickest coating a jig-saw puzzle cracking appearance.

Examination of the microstructures showed what was occurring. The thinner coatings definitely had critical, surface to substrate, cracks in the longitudinal direction. An examination in the circumferential direction did not show any major cracking occurring. The microstructure of the thickest coating showed cracking in the longitudinal direction and in the circumferential direction. The cracks in the longitudinal direction extended from the surface to the substrate but the circumferential cracks extended only a partial amount into the coating. It is conceivable that such a coating might have a tendency to spall off if a load tangential to the top surface were exerted on such a strained coating due to this cracking in two directions along with some accompanying delamination in much evidence about the areas of cracks.

An examination of the raw data showed that the test parameters or equipment were not adequate to capture the true essence of the Mo-Fe blend signals, particularly for the thickest coatings. In the output of data, it was noticed that periodically, events would occur that would totally overwhelm the system and an overflow event was barely recorded. Due to the overflow nature of the event, the event was rejected by the test array and could only be found in the reject statistics or in the raw data. The E.D. period clock was set at the maximum of 16,000ns and so the clock could not be extended to encompass these events. These events did not begin at the first part of the test, but towards the later part. They began first for the thickest section, and then the middle thickness, and finally the thinnest. The coating set that was minimally strained did not exhibit these over-flow events in the raw data.

An examination of the strained microstructures showed some differences. In the maximally strained coatings, cracking extended from the free surface to the substrate. In the minimally strained coatings, there was no evidence of surface to substrate cracks, nor a dye penetrant of wavy longitudinal surface cracks. There was some cracking and delamination but no critical cracks in the minimally strained coating. The cracks appear in different phases of the lamellae but thick lamellae were largely uncracked. As the coating thickened, more areas of delamination and cracking could be seen, but again the thicker lamellae and inclusions were largely uncracked. It is suggested that these large events seen in highly strained coatings are thick portions of the lamellae and inclusions undergoing cracking. There did not seem to be any particular phase or inclusion that was experiencing more cracking than another.

6. CONCLUSIONS

- This test configuration was able to differentiate different material types.
- This method was able to show a thickness effect for pre-cracking behavior in stainless steel coatings.
- The method was not able to produce cracks in the stainless steel coatings.
- For same thicknesses, this method was able to discern between brittle cracking and delamination.
- This method was not sensitive enough to detect brittle cracking in all cases as shown by the lack of emission data for the two thinnest cracked Al_2O_3 coatings.
- This method was able to show differences in cracking behavior as shown by the bimodal shapes of the total energy vs. strain plots.
- Total counts or total energy vs. strain and the log cumulative distribution of events by peak amplitude were useful tools for discerning different types of microstructural damage under constant strain conditions.
- There is a large range in coating responses and the test parameters of the sensor source location array were not adequate to give each type of response the best treatment.

7. RECOMMENDATIONS

- Conduct additional tests with the same test configuration and a frequency analyzer to discern the nature of cracking in Al_2O_3 coatings of thicknesses less than .045".
- If a researcher was interested in studying edge effects, test one, possibly two coatings at one time.
- If interested in studying cracking of ductile materials, change the substrate materials or test parameters to allow for increased elastic strains.
- Develop a conversion program for the AET5500 so that binary data can be converted to ASCII data for more latitude in post-data gathering analysis and presentation.

8. APPENDIX 1 – Metallography Procedures

A. Aluminum Oxide

STEP	SURFACE	ABRASIVE	TIME	FORCE lb/mount	SPEED
Grinding	Diamond grinding disc	30 μm	3 min	5	240
Polish	Metal disc	6 μm	2 min	5	100
Polish	Texmet	1 μm	2 min	5	100
Final Polish	Microcloth	Master polish	1 min	2.5	100

B. Stainless Steel 420

STEP	SURFACE	ABRASIVE	TIME	FORCE lb/mount	SPEED
Grinding	Si – C paper			5	240
Diamond Polish	Cotton Cloth	6 μm	2 min	2.5	100
Diamond Polish	Cotton Cloth	3 μm	2 min	2.5	100
	Texmet	1 μm	2 min	2.5	100
OP	Microcloth	OP – 5	1 min	2.5	100

C. High Energy Coating

STEP	SURFACE	ABRASIVE	TIME	FORCE lb/mount	SPEED
Grinding	Si - C paper			5	240
Diamond- Polish	Cotton Cloth	6 μm	2 min	2.5	100
Diamond Polish	Cotton Cloth	3 μm	2 min	2.5	100
Diamond Polish	Texmet	1 μm	2 min	2.5	100
OP	Microcloth	OP - 5	1 min	2.5	100

9. APPENDIX 2 – Procedure for Dye Penetrant Testing of Coatings

1. Clean coating with acetone
2. Spray with Dye Penetrant
3. Wait 10 minutes
4. Wipe with dry cloth
5. Wipe with acetone soaked cloth
6. Spray coating with remover
7. Wipe with dry cloth
8. Spray with developer
9. Wait 5 minutes
10. Photograph
11. Wait 2 more minutes
12. Photograph
13. Rinse with acetone and wipe with dry cloth
14. Wait 5 minutes
15. Rephotograph

10. APPENDIX 3 – Typical A.E. Test Parameters Display

The following shows an example of the output displayed by the A.E.T. 5500 system.

```

1  00:0:03      320      1000      16000      250
TST RDC RNG  ED RNG(US) AMP RNG(DB)  RT  RNG(US) SLP  RNG(MV/US) ENERGY
RNG
1  5  1000      100 300          0  117          1  1000      0 65520      0
165

```

```

TST PAR  1 RNG(MV)  PAR  2  RNG(MV)  PAR  3  RNG(MV)
1          0 10240          0  10240          0 10240

```

```

TST L  SEN  H SEN  L LOC  H LOC  DT  VEL
1    1    2    50   150   62  16
1    2    3    150  250   70  14
1    3    4    250  350   65  15

```

```

TST RGN  LOWER  LIMIT  UPPER  LIMIT
1    1          0      60
1    2          90     130
1    3         180     220
1    4         240     250
1    5         270     310
1    6         340     360
1  INVALID EVENTS TO REGION 0

```

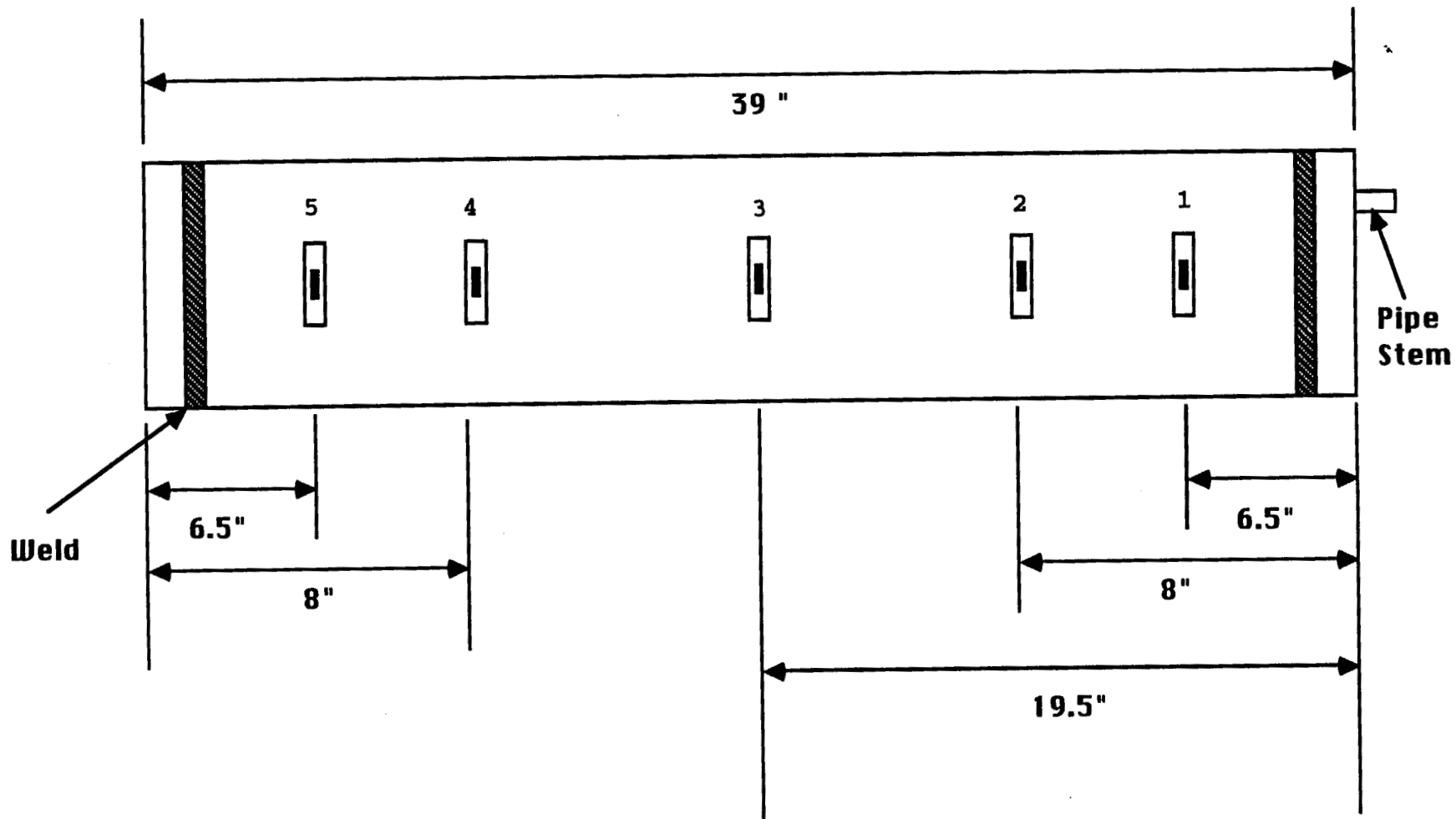


FIGURE 1 - LOCATION OF STRAIN GAGES FOR STRAIN ANALYSIS

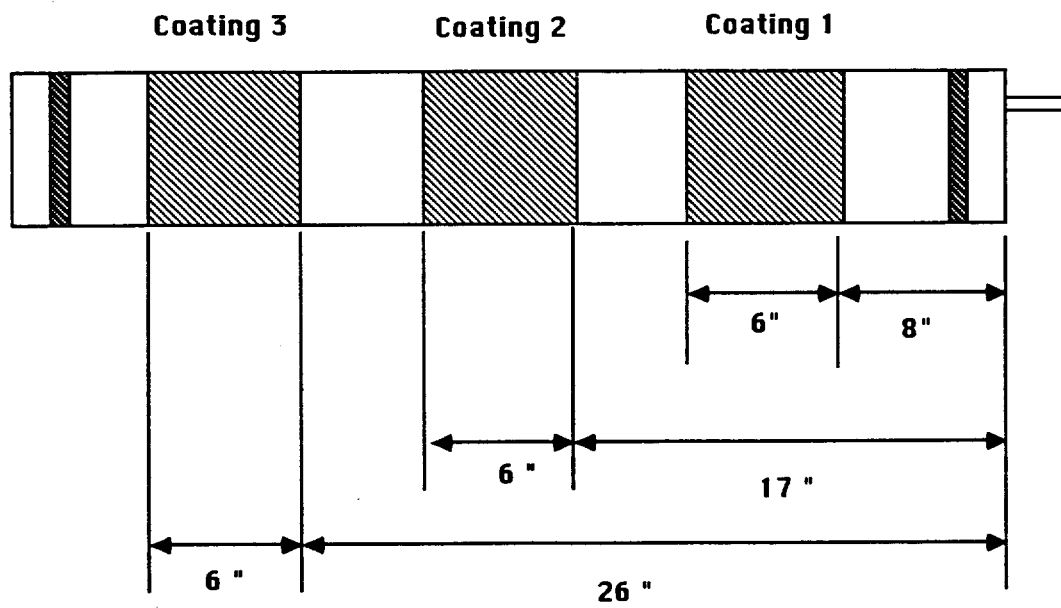


Figure 2 – COATING PLACEMENT

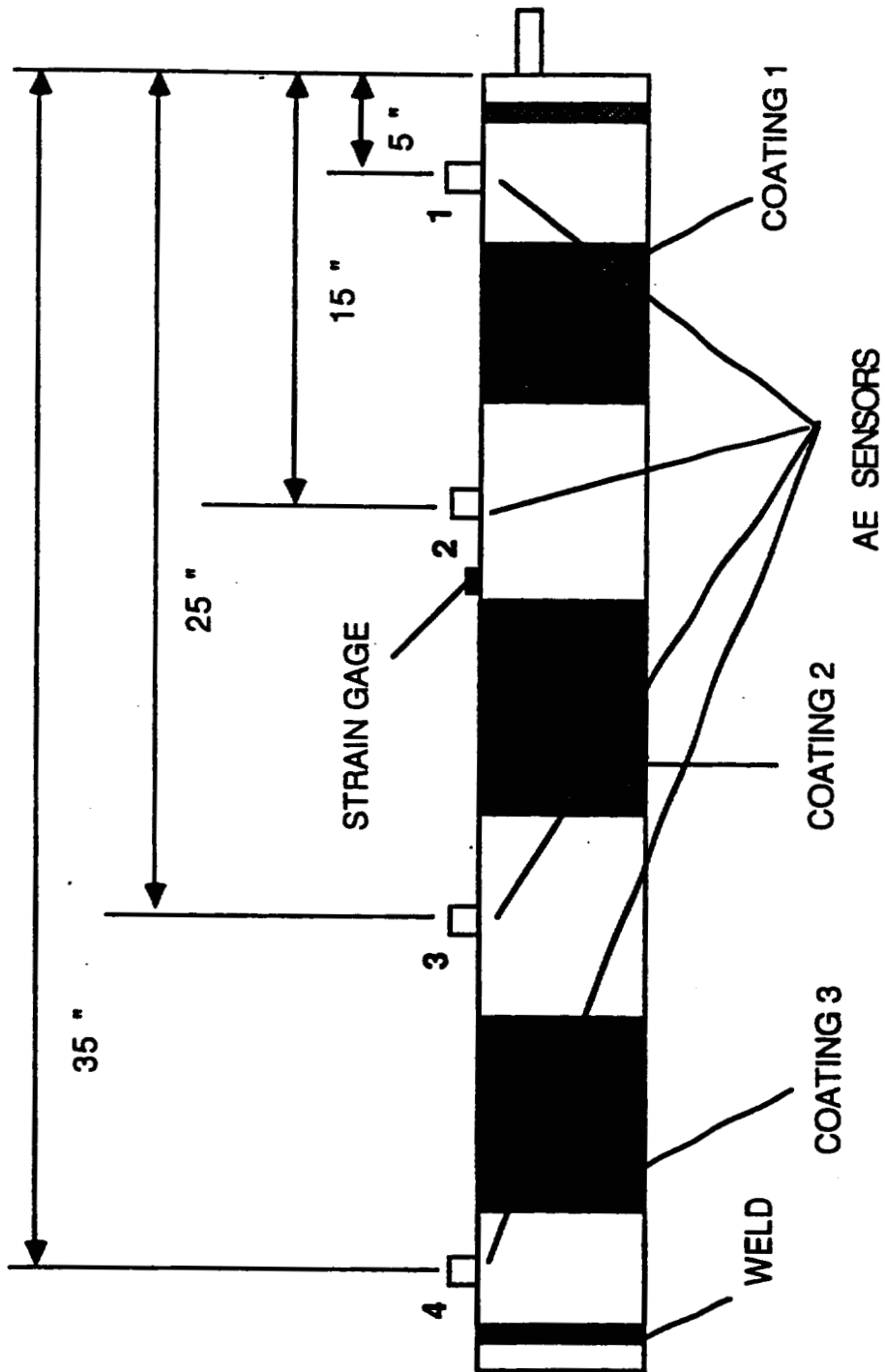


FIGURE 3 - ACOUSTIC EMISSION SENSOR LAYOUT

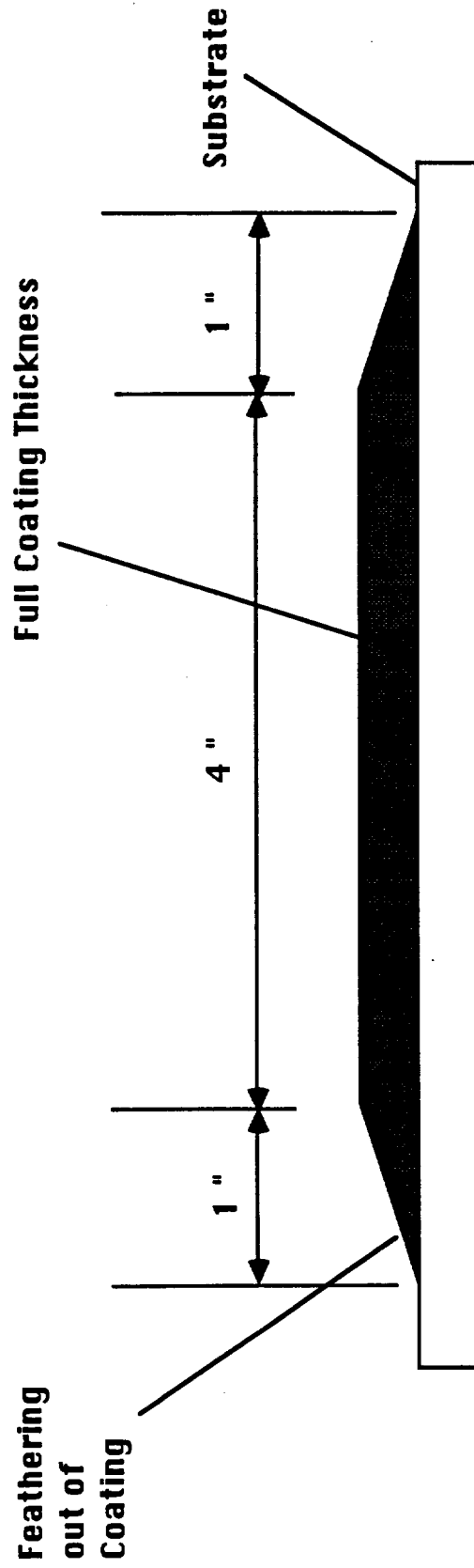


FIGURE 4 - COATING PROFILE

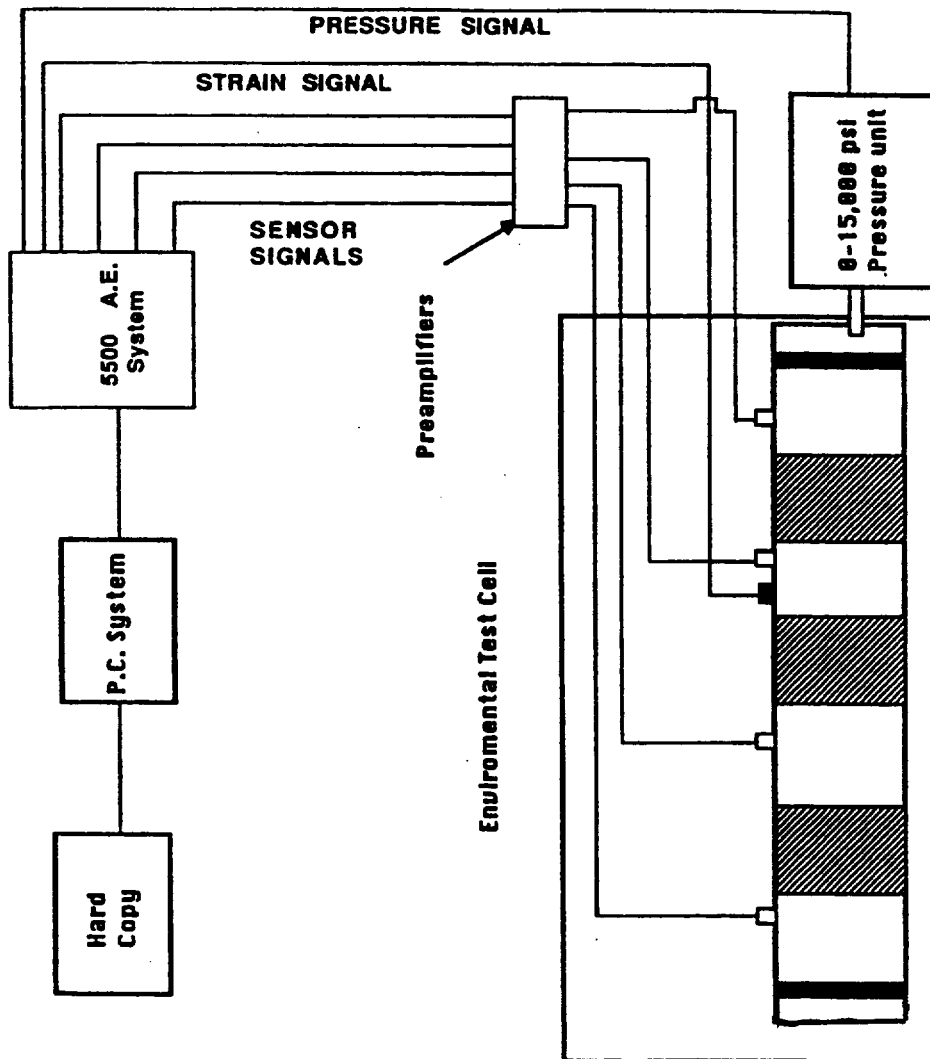


FIGURE 5 - TEST SYSTEM CONFIGURATION.

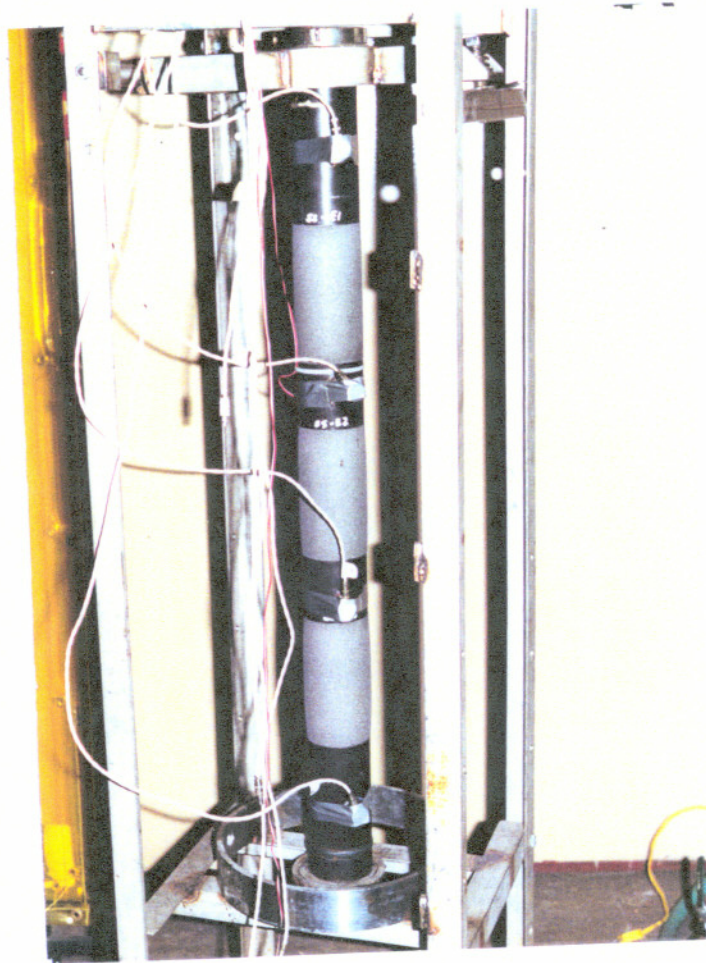


Figure 6 – ACOUSTIC EMISSION SENSORS IN POSITION ON COATED TUBING.



Figure 7 – BANDSAW SECTIONING OPERATION

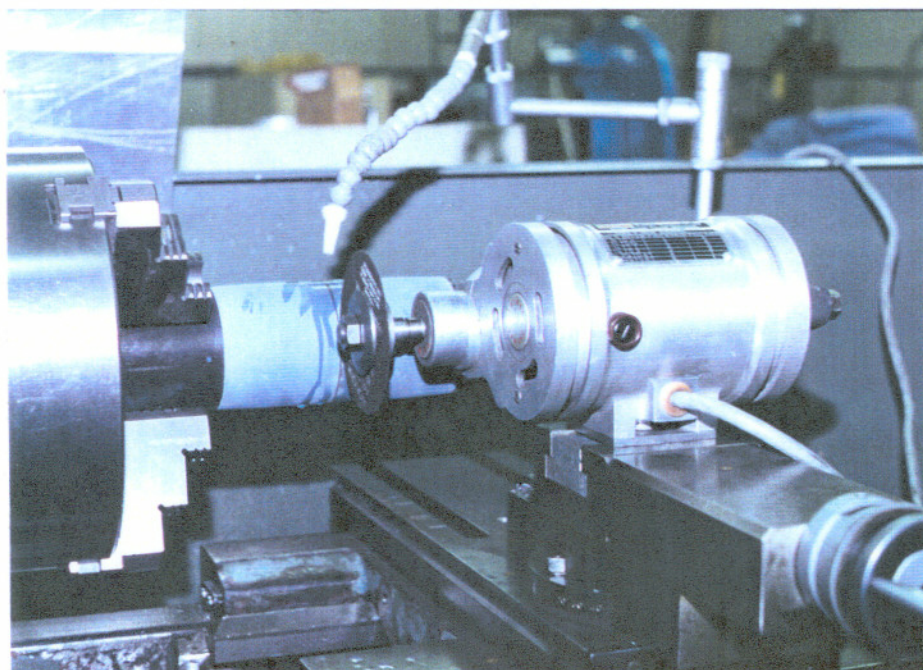


Figure 8 – LATHE SECTIONING OPERATION

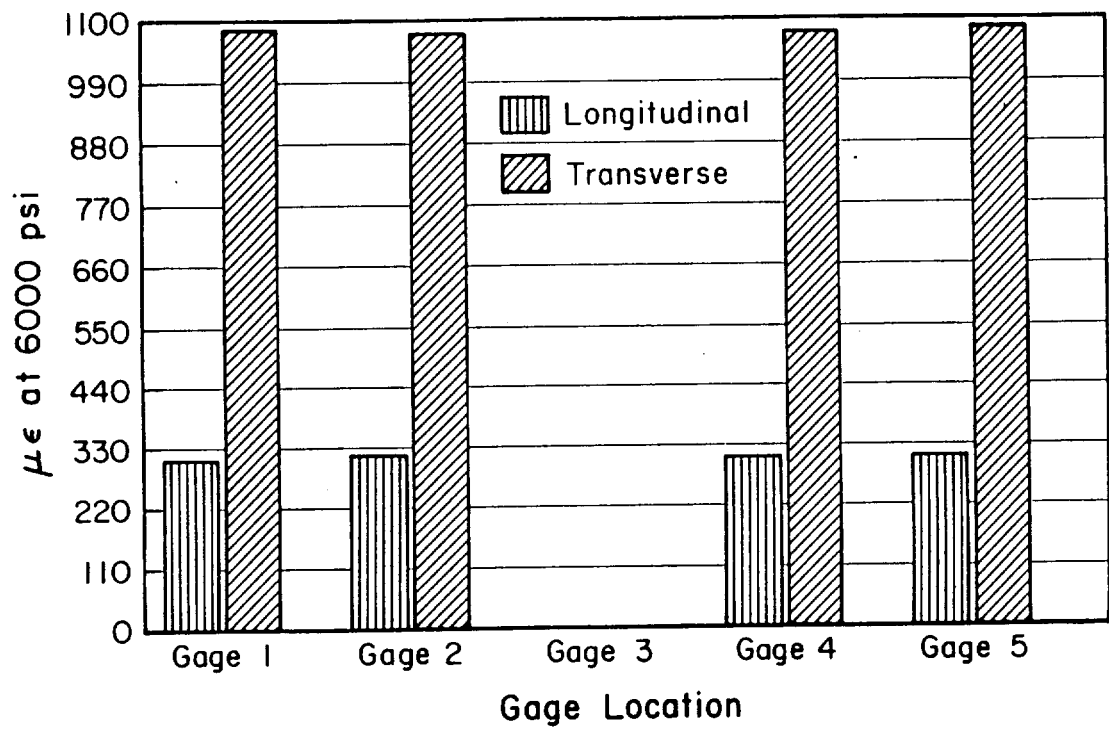


Figure 9 – STRAIN VALUES AT VARIOUS POSITIONS ALONG UNSPRAYED BOILER TUBE. PRESSURIZATION TO 6,000 PSI.

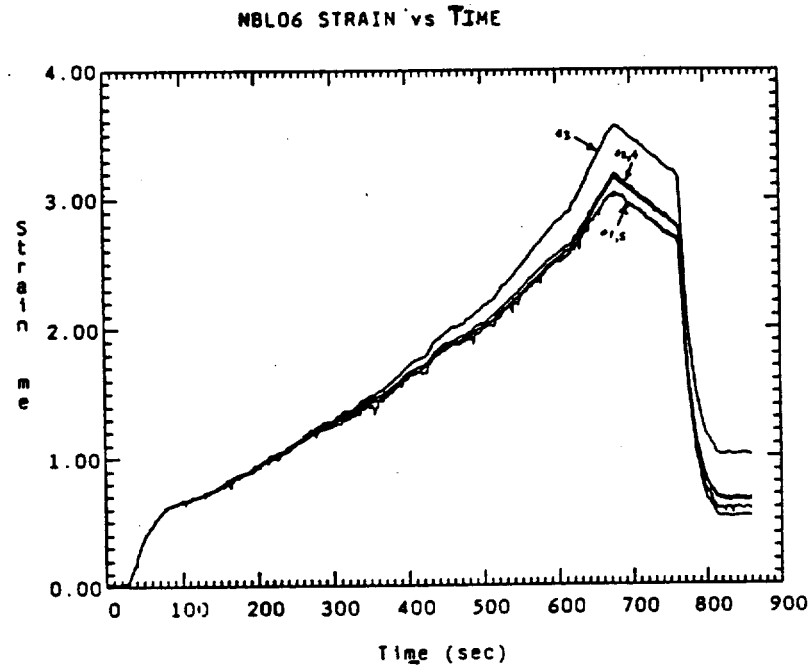


Figure 10a – STRAIN VALUES AT VARIOUS POSITIONS ALONG UNSPRAYED BOILER TUBE. INITIAL PRESSURIZATION TO 13,000 PSI.

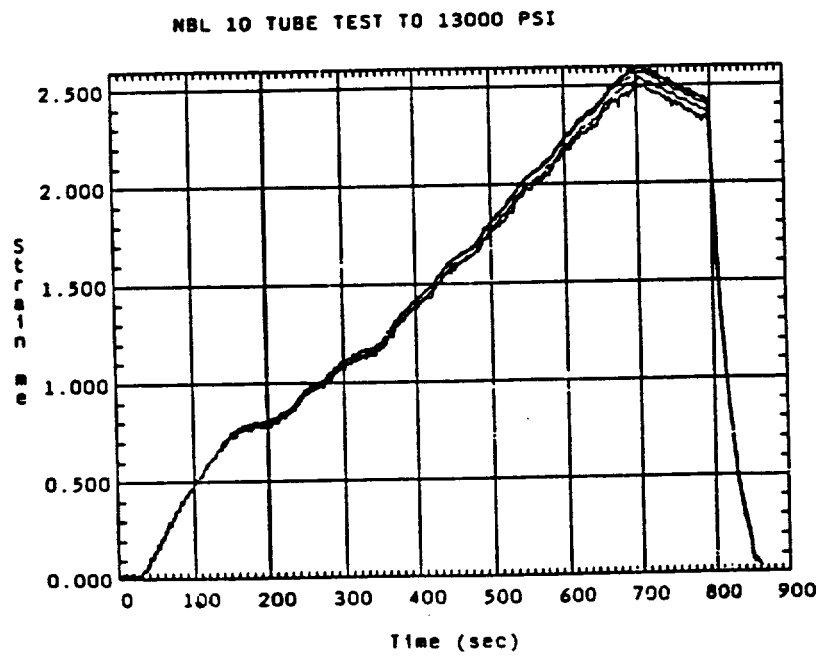


Figure 10b – STRAIN VALUES AT VARIOUS POSITIONS ALONG UNSPRAYED BOILER TUBE. SUBSEQUENT PRESSURIZATION TO 13,000 PSI.

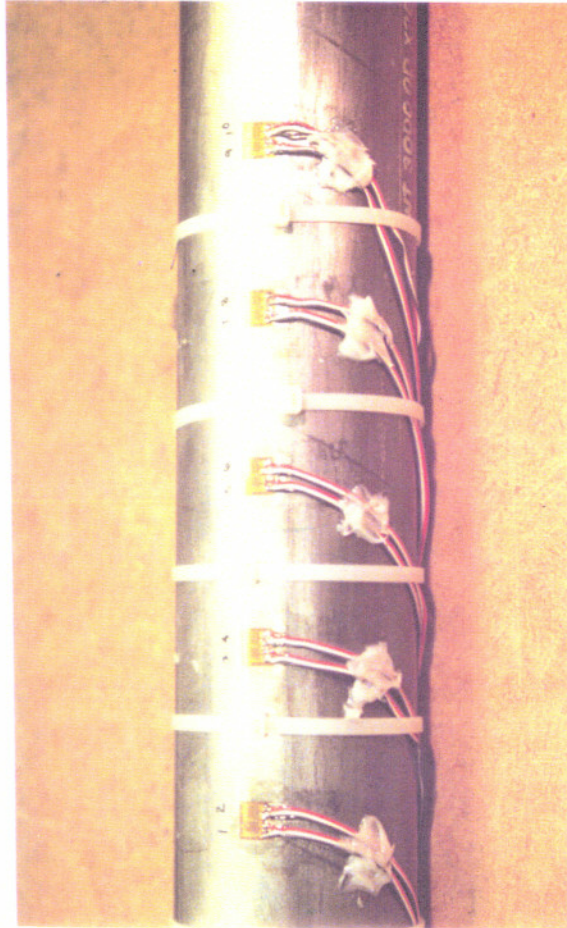


Figure 11 – STRAIN GAGES FOR STRAIN ANALYSIS MOUNTED ON BARE BOILER TUBE, 6000 PSI MAXIMUM PRESSURE.

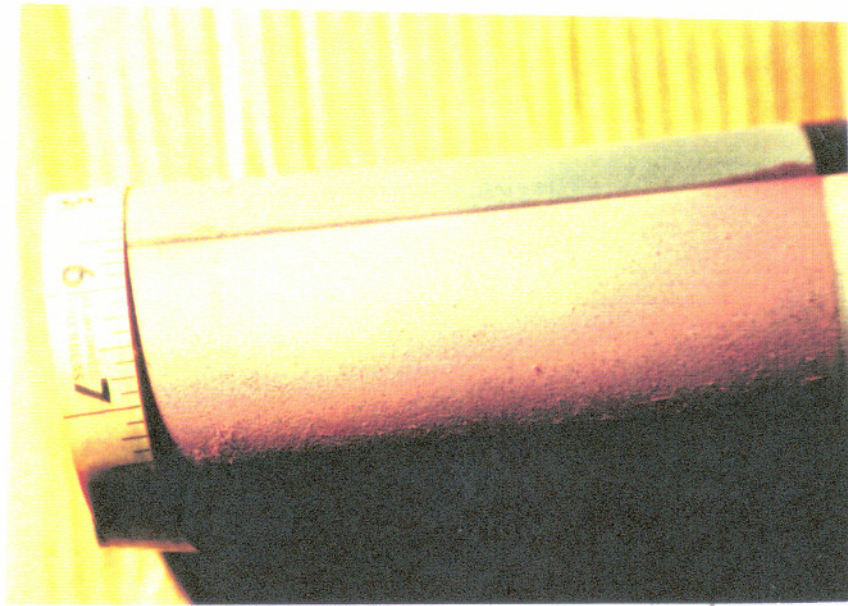


Figure 13 – DYE PENETRANT TEST FOR .015" THICK Al_2O_3 COATING
MAXIMUM STRAIN CONDITION

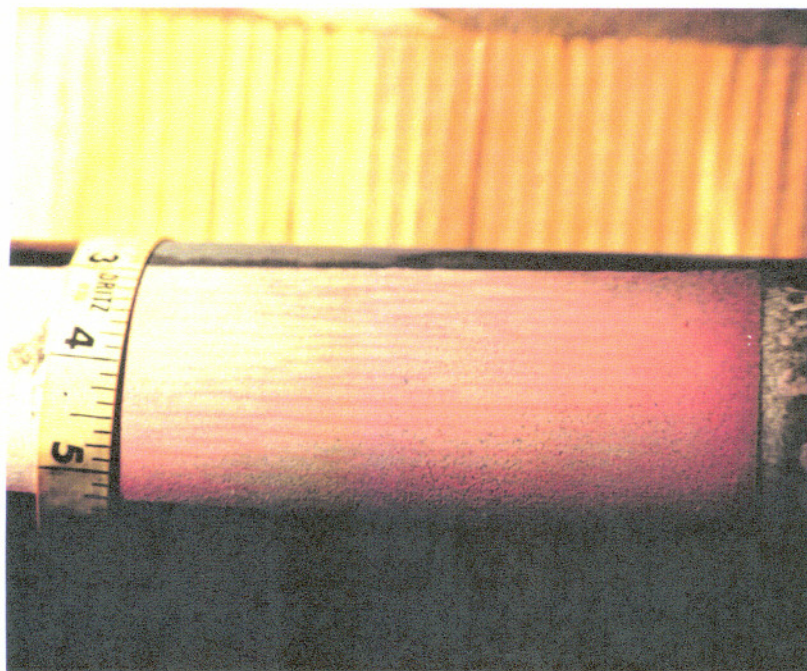


Figure 14 – DYE PENETRANT TEST FOR .030" THICK Al_2O_3 COATING
MAXIMUM STRAIN CONDITION

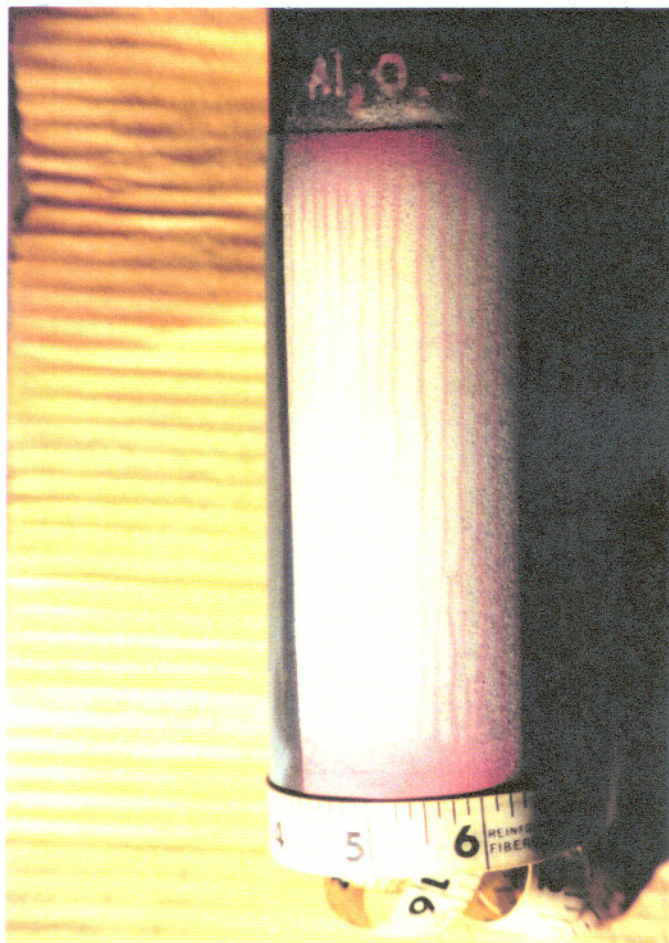


Figure 15 – DYE PENETRANT TEST FOR .045" THICK STRAINED AL₂O₃ COATING, MAXIMUM STRAIN CONDITION



Figure 16 – DYE PENETRANT TEST FOR .045" THICK Al_2O_3 COATING, MINIMUM STRAIN CONDITION.

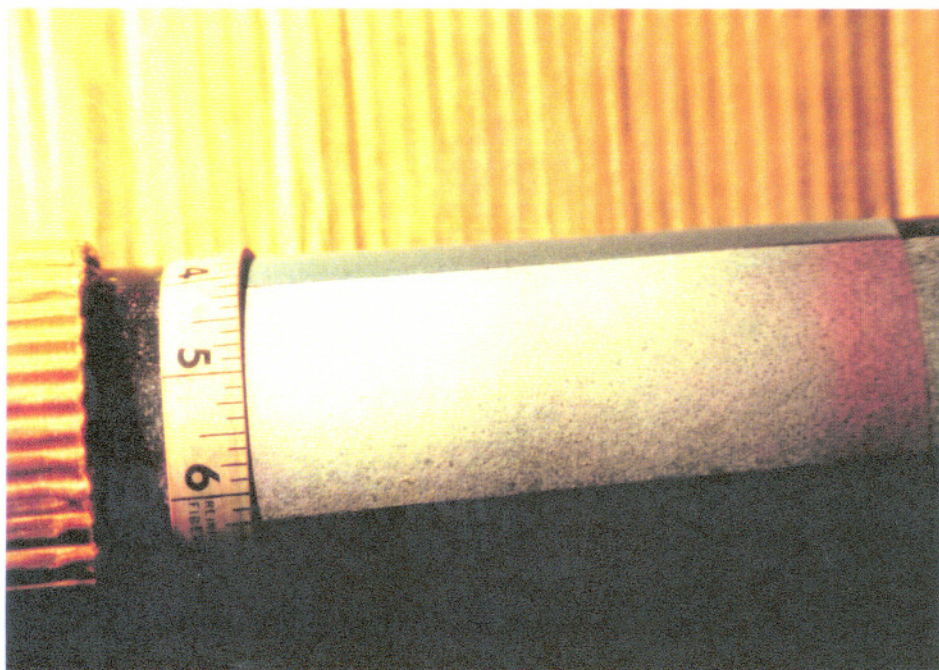


Figure 17 – DYE PENETRANT TEST FOR .030" THICK AL₂O₃ COATING, UNSTRAINED CONDITION.

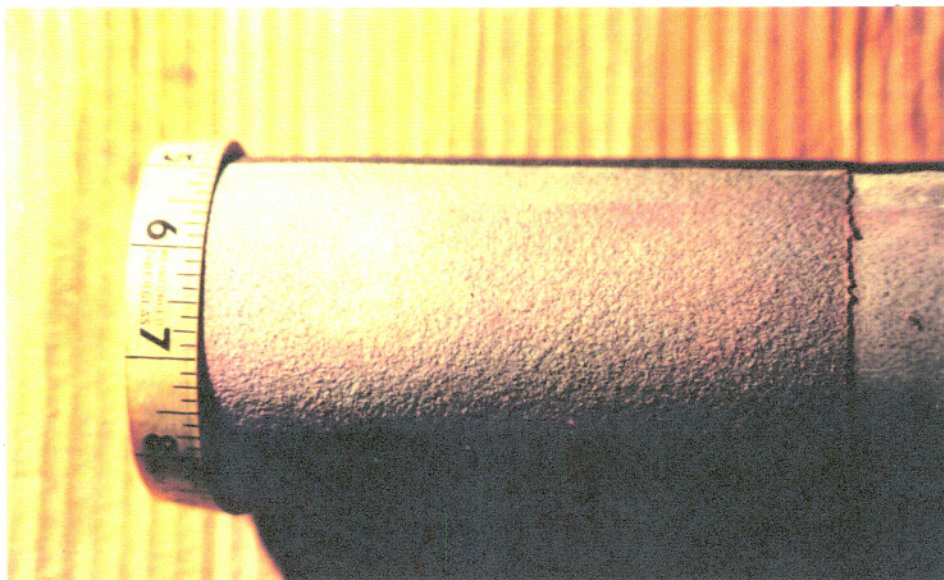


Figure 18 – TYPICAL DYE PENETRANT TEST FOR .045" THICK STAINLESS STEEL COATING, MAXIMUM STRAIN CONDITION.

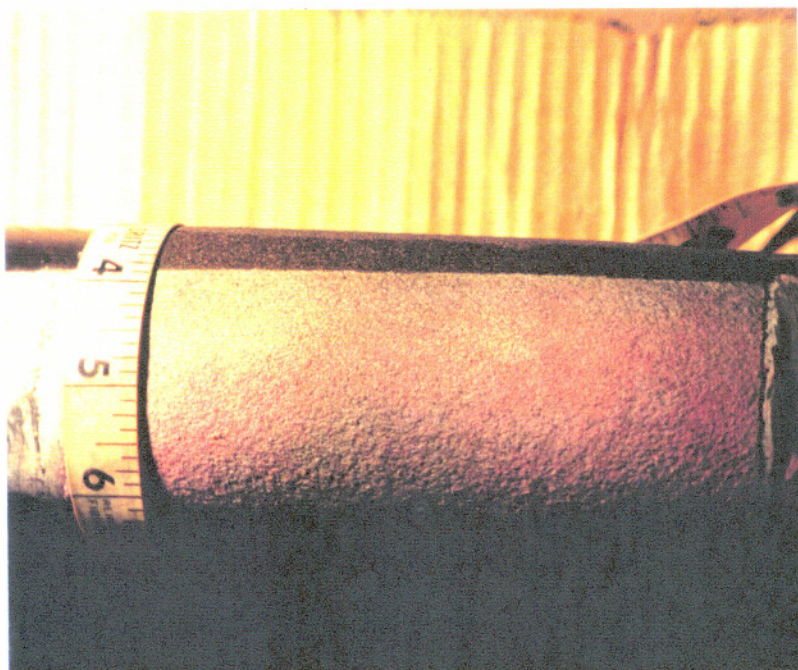


Figure 19 – TYPICAL DYE PENETRANT TEST FOR .070" THICK STAINLESS STEEL COATING, MAXIMUM STRAIN CONDITION.

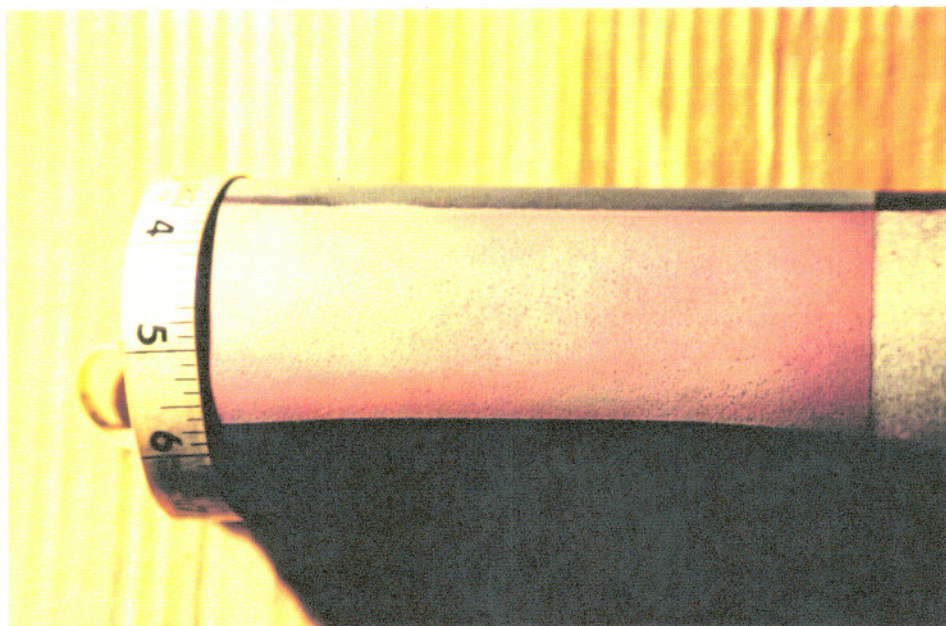


Figure 20 – TYPICAL DYE PENETRANT TEST FOR .100" THICK STAINLESS STEEL COATING, MAXIMUM STRAIN CONDITION.

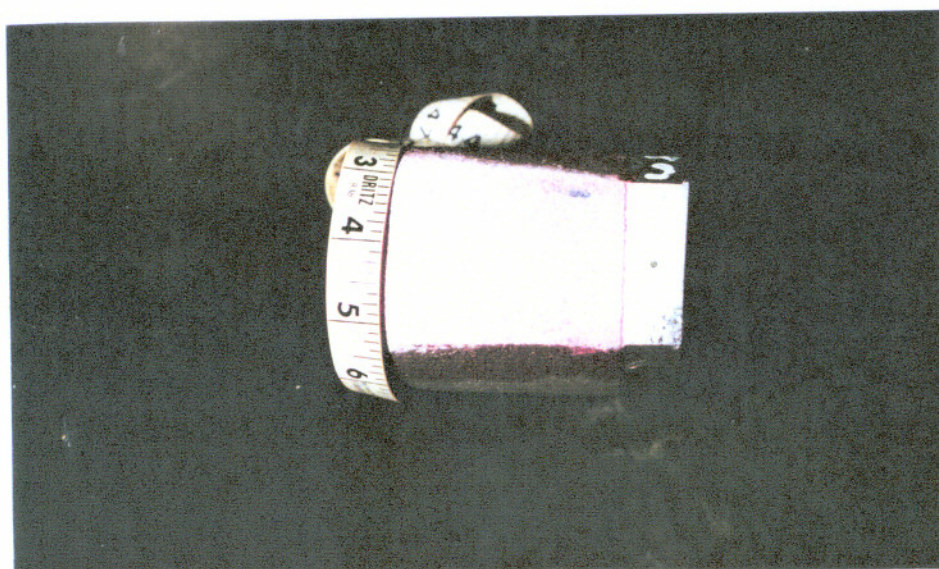


Figure 21 – DYE PENETRANT TEST FOR STAINLESS STEEL COATING, UNSTRAINED CONDITION.

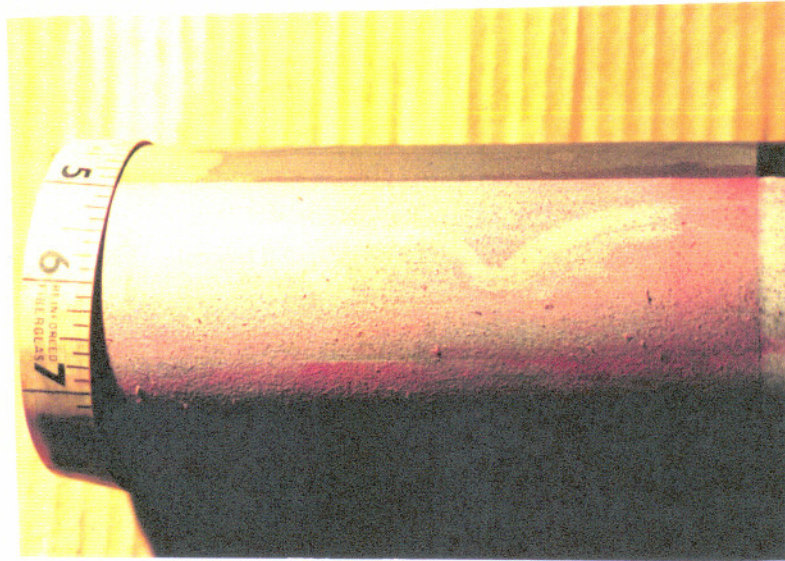


Figure 22 – DYE PENETRANT TEST .020" THICK Mo-Fe BLEND COATING, MAXIMUM STRAIN CONDITION.

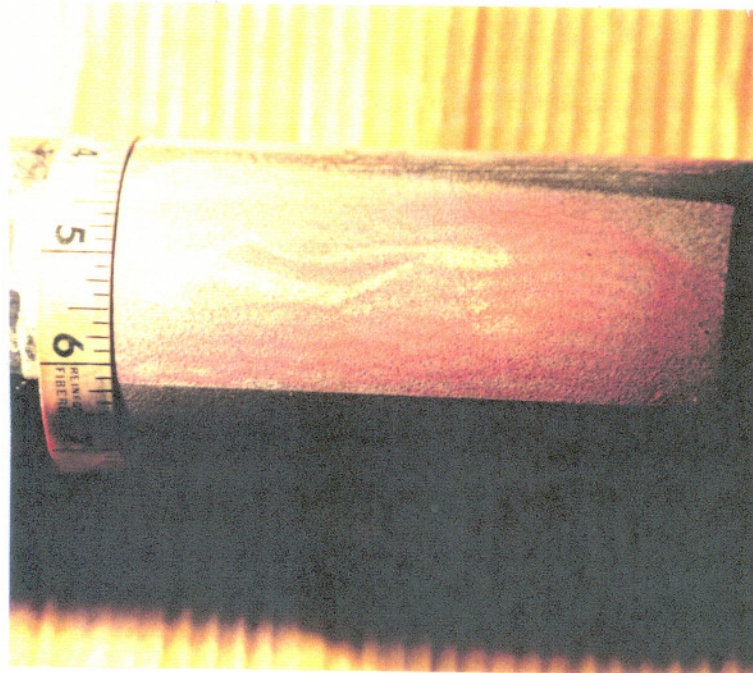


Figure 23 – DYE PENETRANT TEST .030" THICK Mo-Fe BLEND COATING, MAXIMUM STRAIN CONDITION.

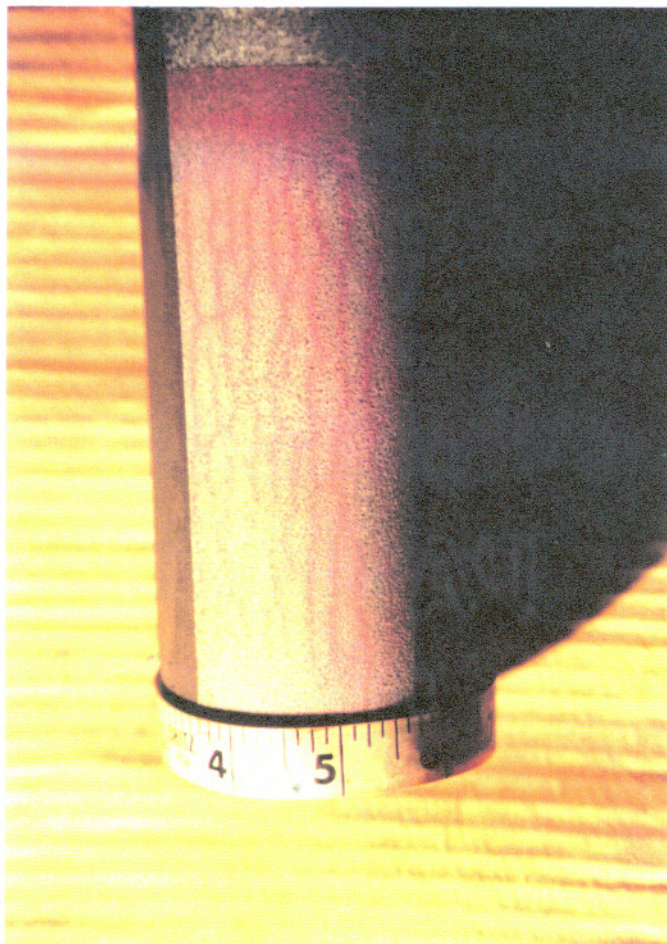


Figure 24 – DYE PENETRANT TEST FOR .040" THICK Mo-Fe BLEND COATING, MAXIMUM STRAIN CONDITION.

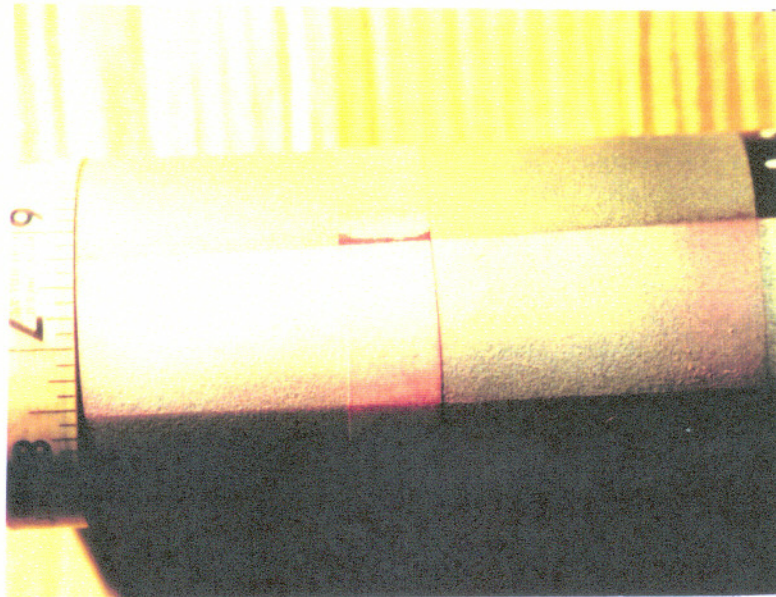


Figure 25 – DYE PENETRANT TEST FOR .030" THICK Mo-Fe BLEND COATING (INERT GAS ATMOSPHERE), UNSTRAINED COATING.

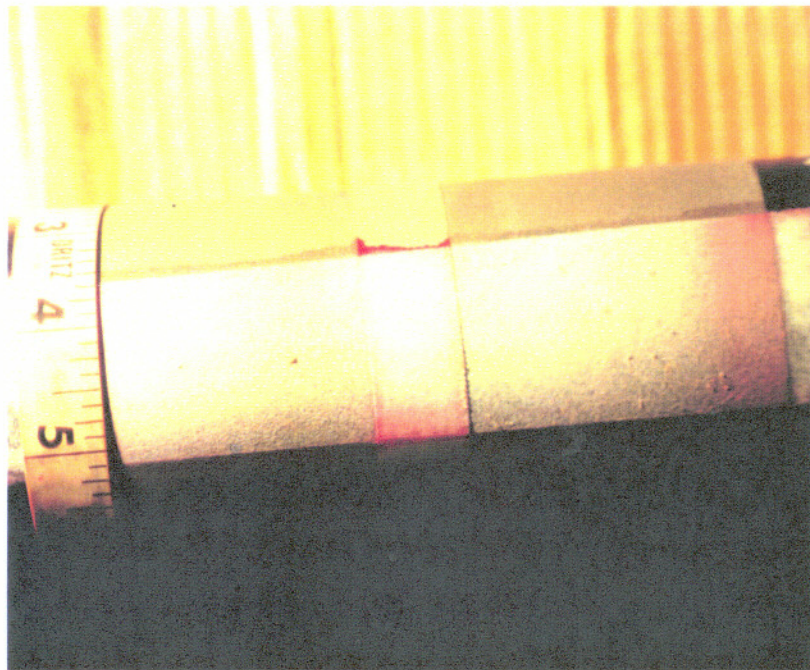


Figure 26 – DYE PENETRANT TEST FOR .030" THICK Mo-Fe BLEND COATING (STANDARD GAS ATMOSPHERE), UNSTRAINED COATING.



Figure 27 – DYE PENETRANT TEST FOR .020" THICK Mo-Fe BLEND COATING, MINIMUM STRAIN CONDITION.



Figure 28 – DYE PENETRANT TEST FOR .030" THICK Mo-Fe BLEND COATING, MINIMUM STRAIN CONDITION.

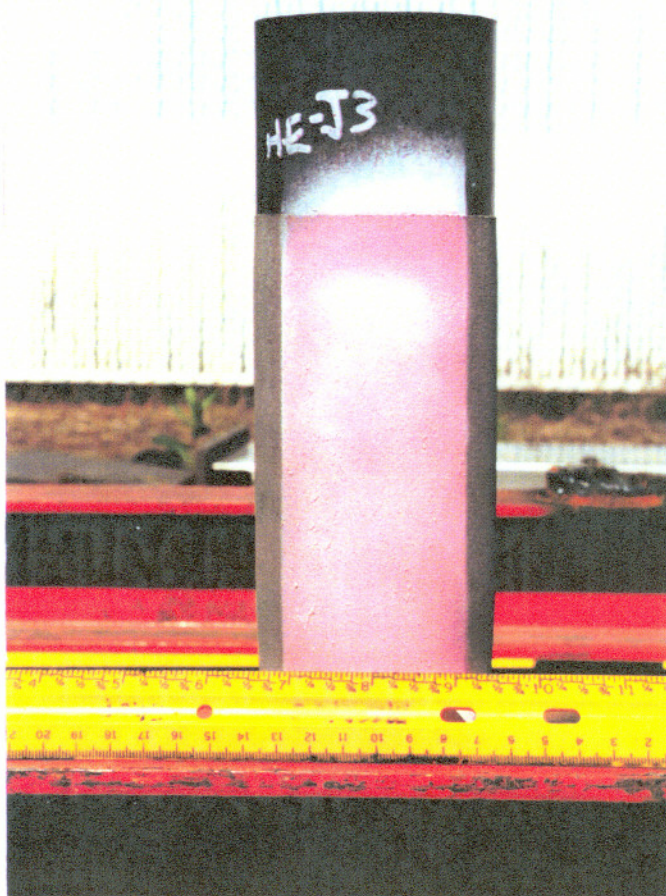


Figure 29 – DYE PENETRANT TEST FOR .040" THICK Mo-Fe BLEND COATING, MINIMUM STRAIN CONDITION.

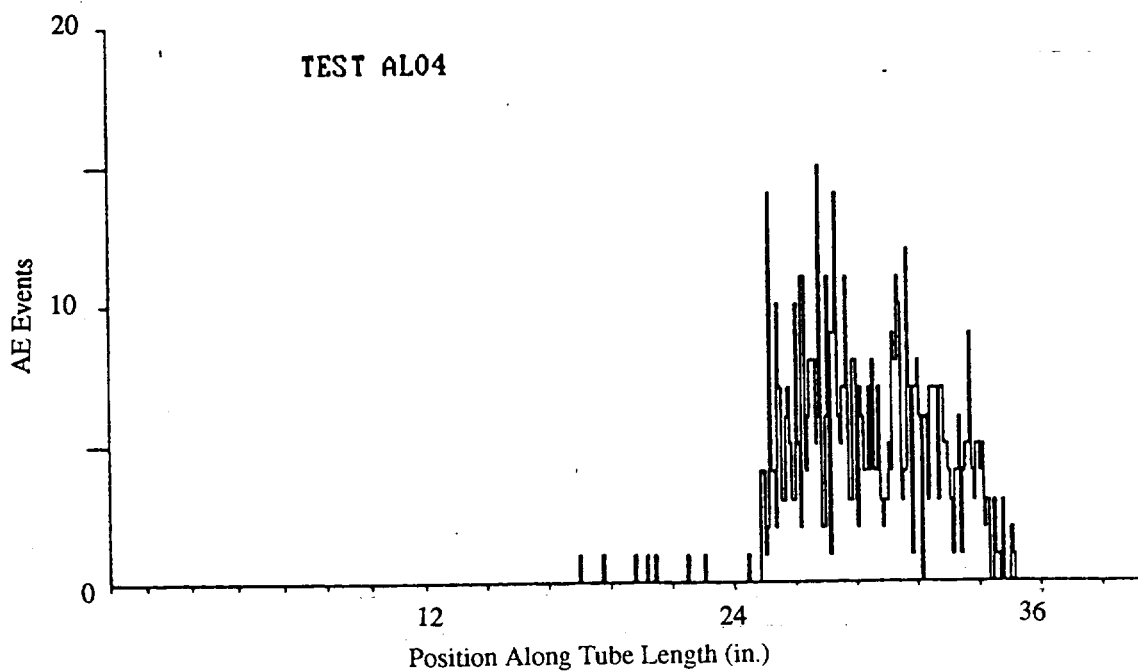


Figure 30 - TYPICAL DISTRIBUTION OF EVENTS BY LOCATION FOR AL_2O_3 COATINGS.

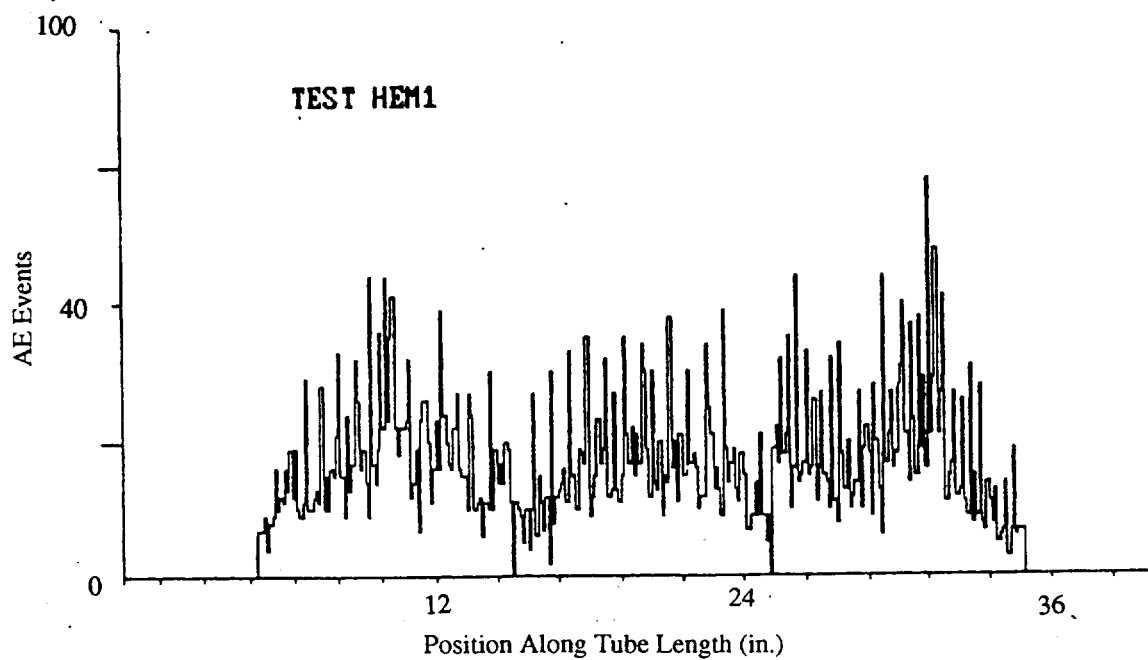


Figure 31 - TYPICAL DISTRIBUTION OF EVENTS BY LOCATION FOR Mo-Fe BLEND COATINGS.

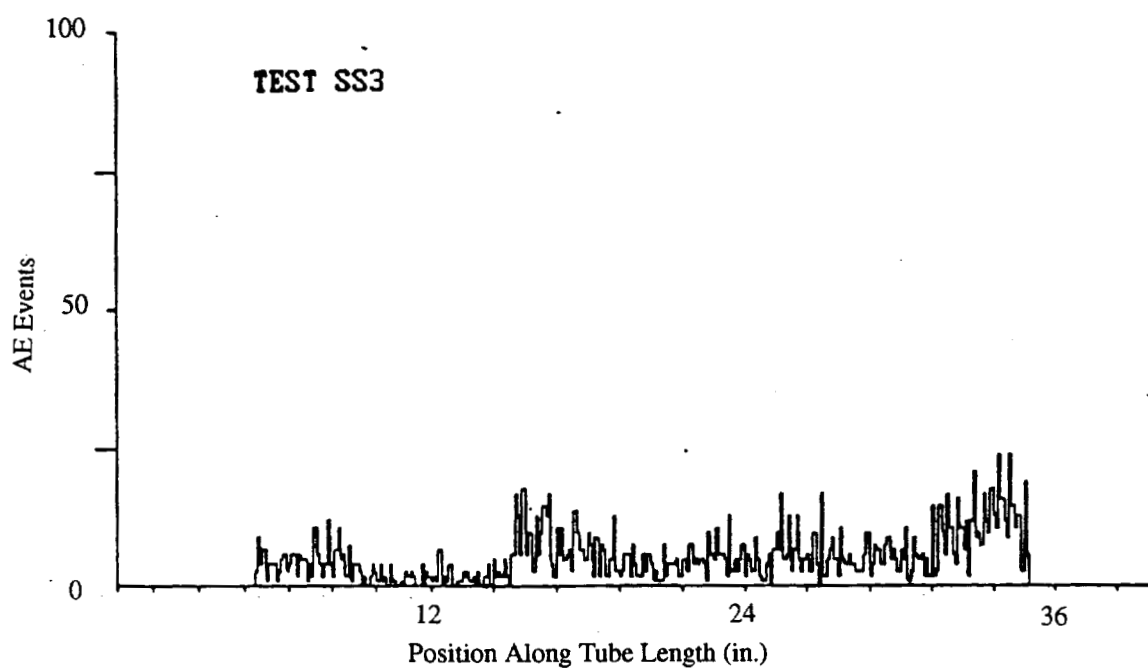


Figure 32 – TYPICAL DISTRIBUTION OF EVENTS BY LOCATION FOR STAINLESS STEEL COATINGS.

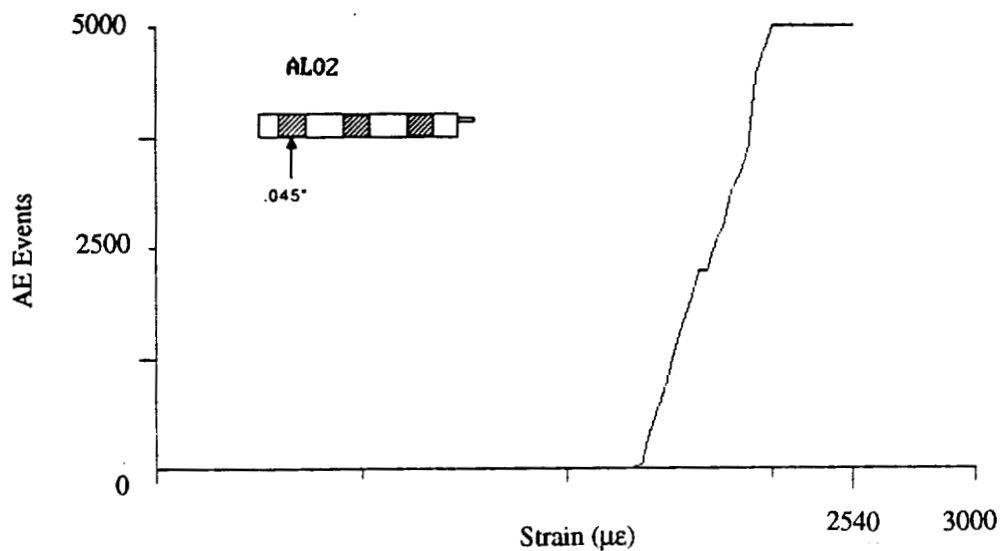


Figure 33 – TYPICAL PLOT OF TOTAL ENERGY VS. STRAIN FOR .045" THICK Al_2O_3 COATING.

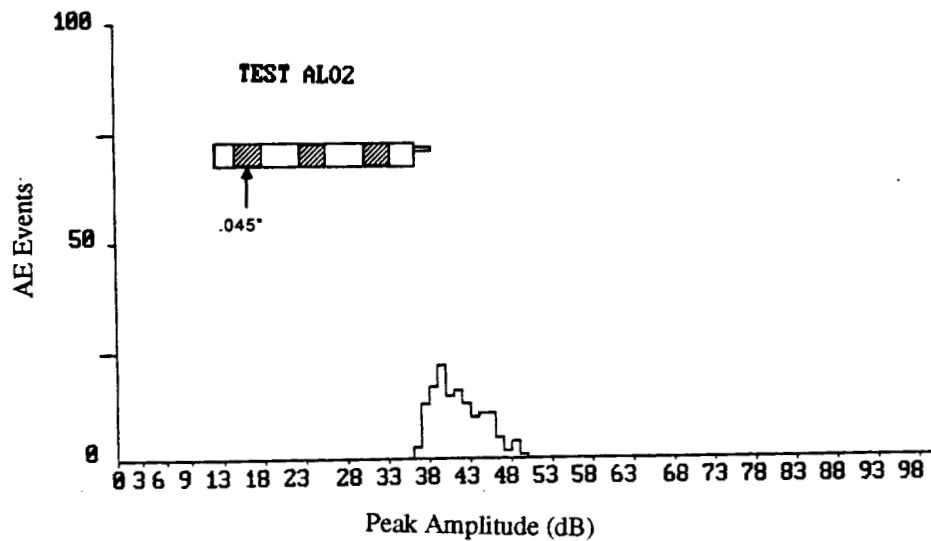


Figure 34 – TYPICAL PLOT OF DISTRIBUTION OF EVENTS BY PEAK AMPLITUDE (dB) FOR .045" THICK Al_2O_3 COATING, MAXIMUM STRAIN CONDITION.

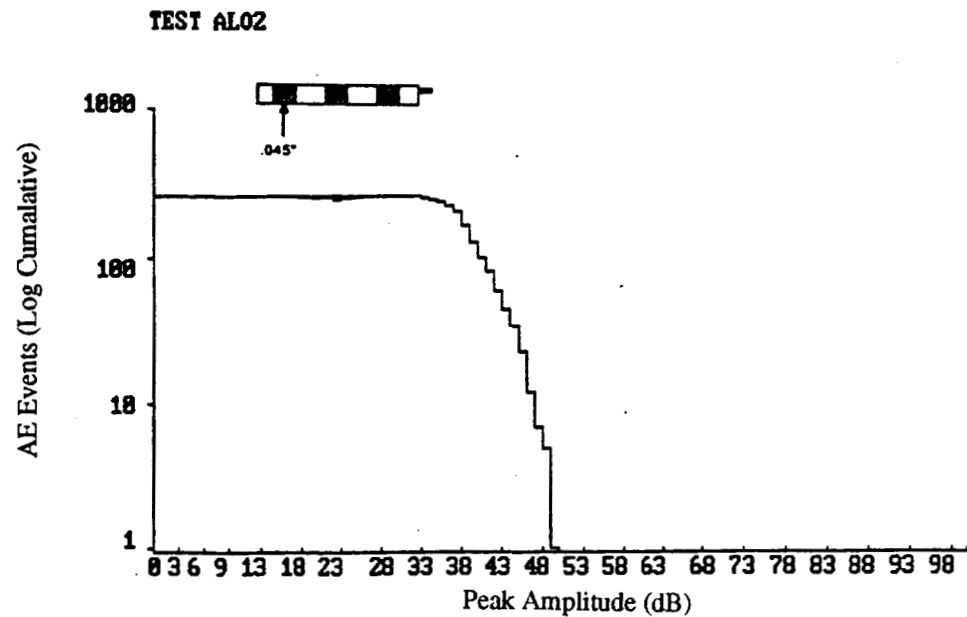


Figure 35 – TYPICAL PLOT OF LOG OF CUMULATIVE DISTRIBUTION OF EVENTS BY PEAK AMPLITUDE (dB) FOR .045" THICK Al_2O_3 COATING, MAXIMUM STRAIN CONDITION.

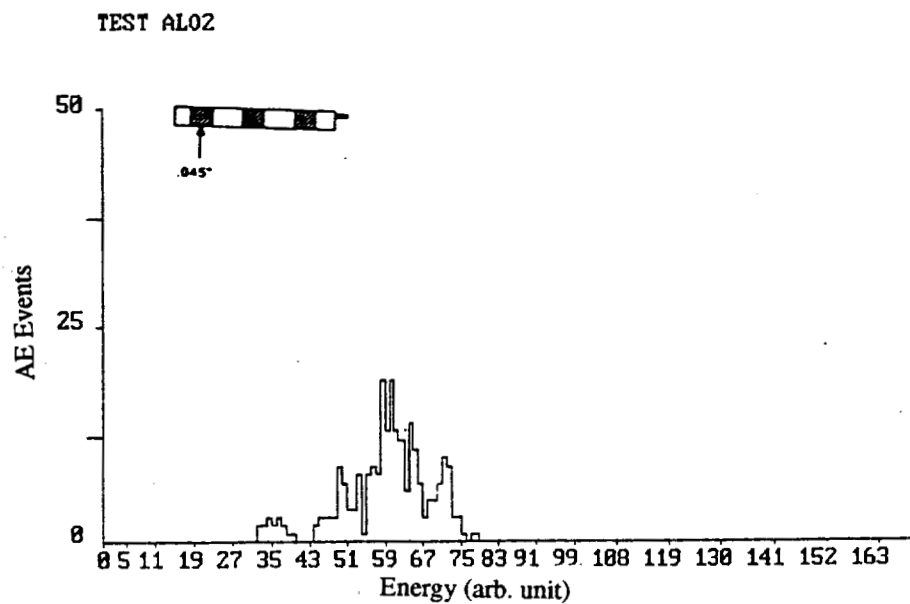


Figure 36 – TYPICAL DISTRIBUTION OF EVENTS BY ENERGY FOR .045" THICK Al_2O_3 COATING, MAXIMUM STRAIN CONDITION.

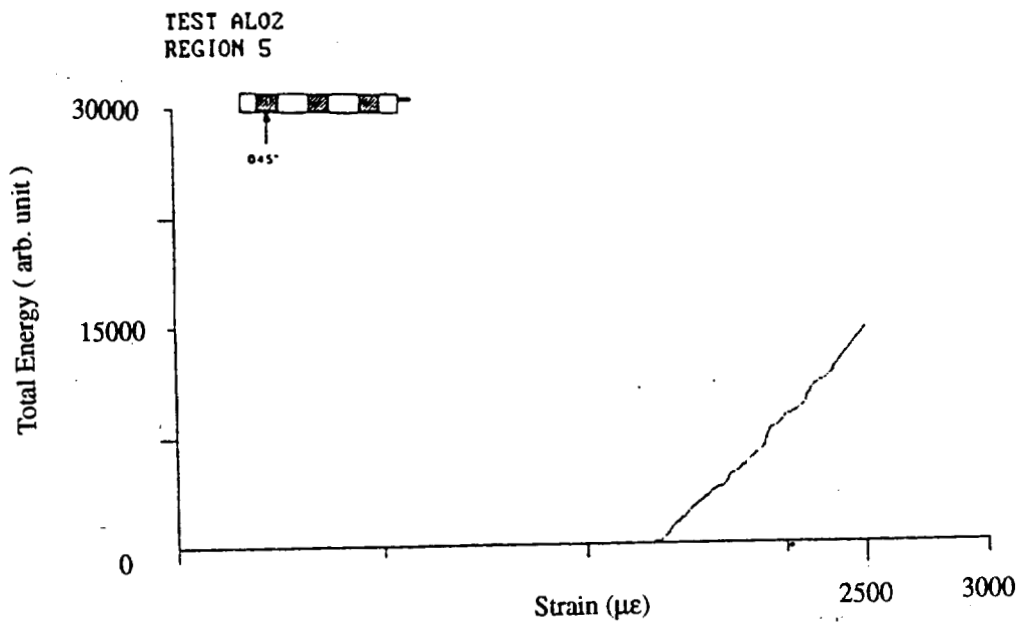


Figure 37 – TYPICAL TOTAL ENERGY VS. STRAIN FOR .045" THICK AL_2O_3 COATINGS, MAXIMUM STRAIN CONDITION.

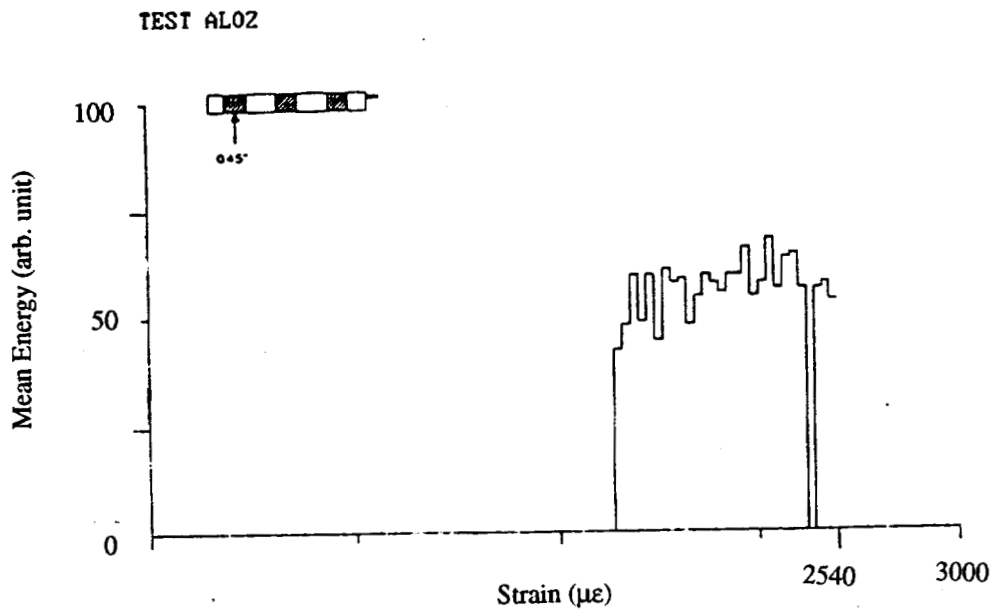


Figure 38 – TYPICAL PLOT OF MEAN ENERGY VS. STRAIN FOR .045" THICK AL_2O_3 COATINGS, MAXIMUM STRAIN CONDITION.

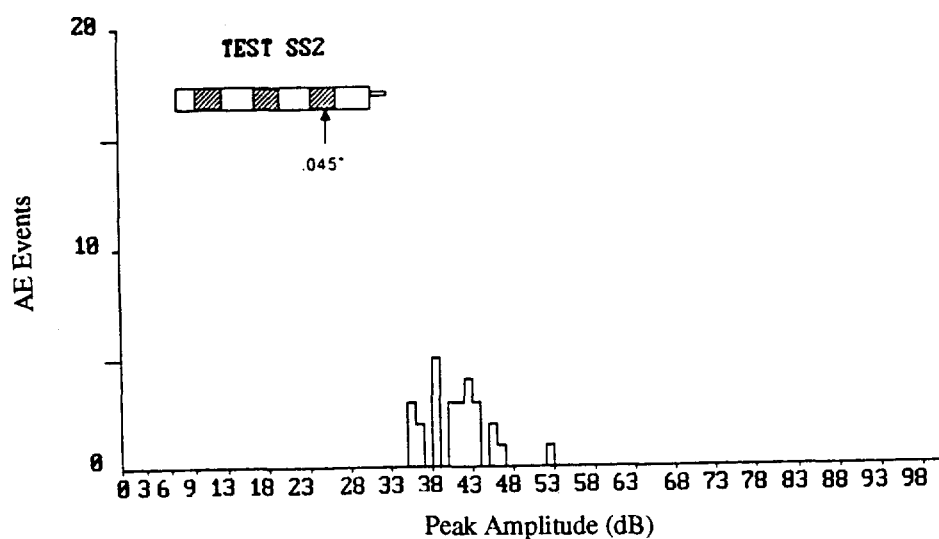


Figure 39 – TYPICAL DISTRIBUTION OF EVENTS BY PEAK AMPLITUDE (dB) for .045" THICK STAINLESS STEEL COATING, MAXIMUM STRAIN CONDITION.

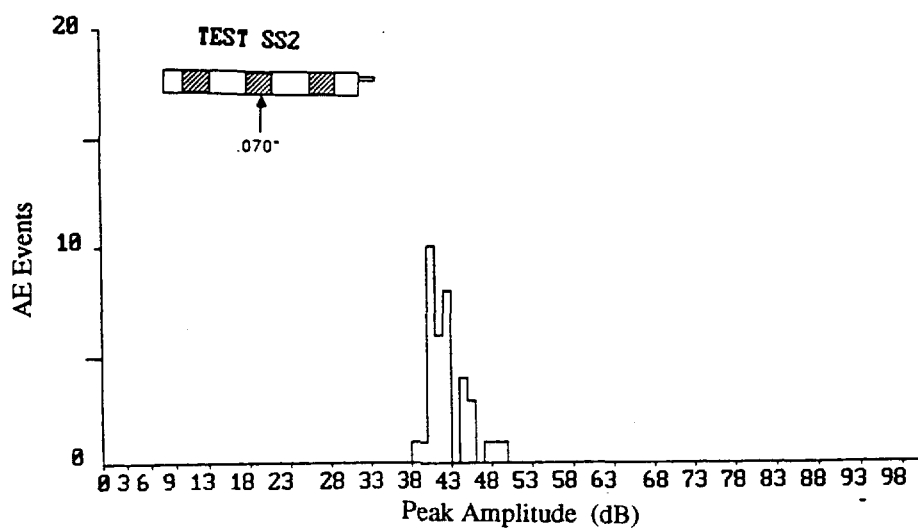


Figure 40 – TYPICAL DISTRIBUTION OF EVENTS BY PEAK AMPLITUDE (dB) for .070" THICK STAINLESS STEEL COATING, MAXIMUM STRAIN CONDITION.

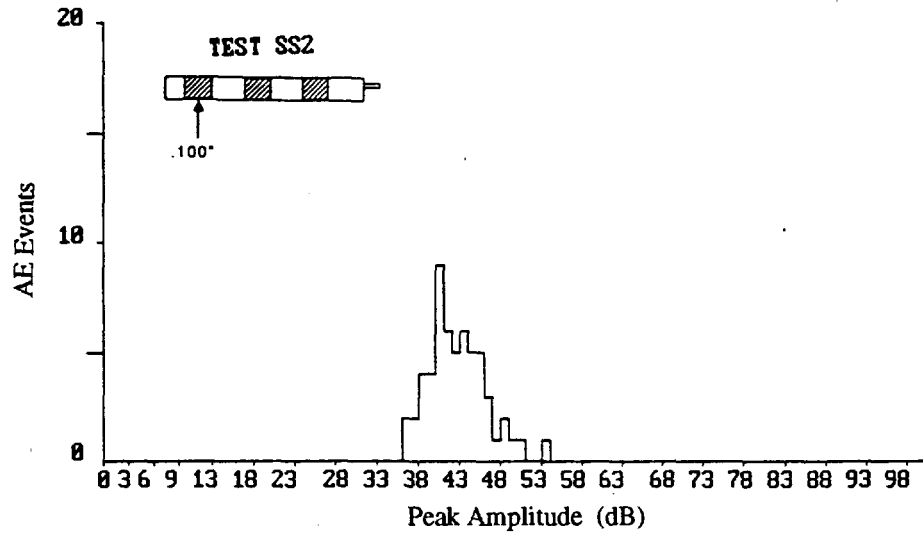


Figure 41 – TYPICAL DISTRIBUTION OF EVENTS BY PEAK AMPLITUDE (dB) for .100” THICK STAINLESS STEEL COATING, MAXIMUM STRAIN CONDITION.

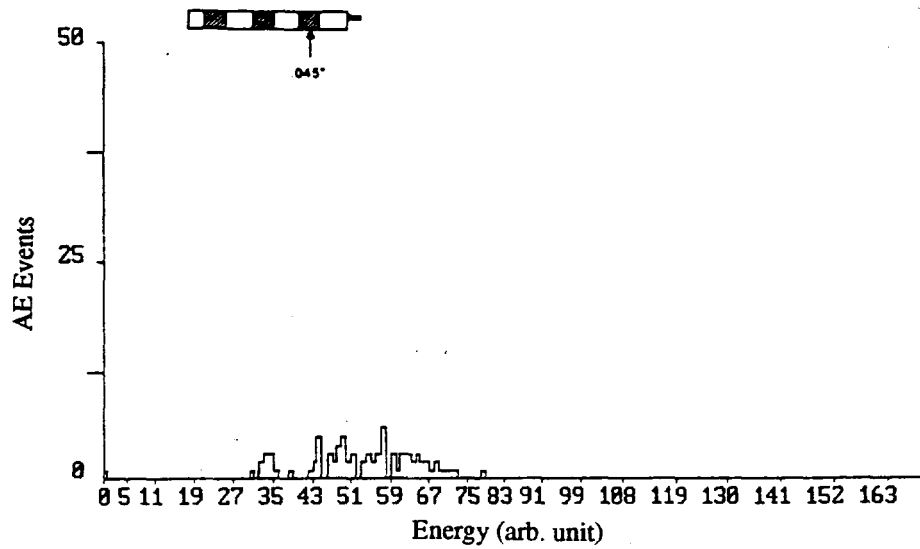


Figure 42 – TYPICAL DISTRIBUTION OF EVENTS BY ENERGY FOR .045” THICK STAINLESS STEEL COATINGS, MAXIMUM STRAIN CONDITION.

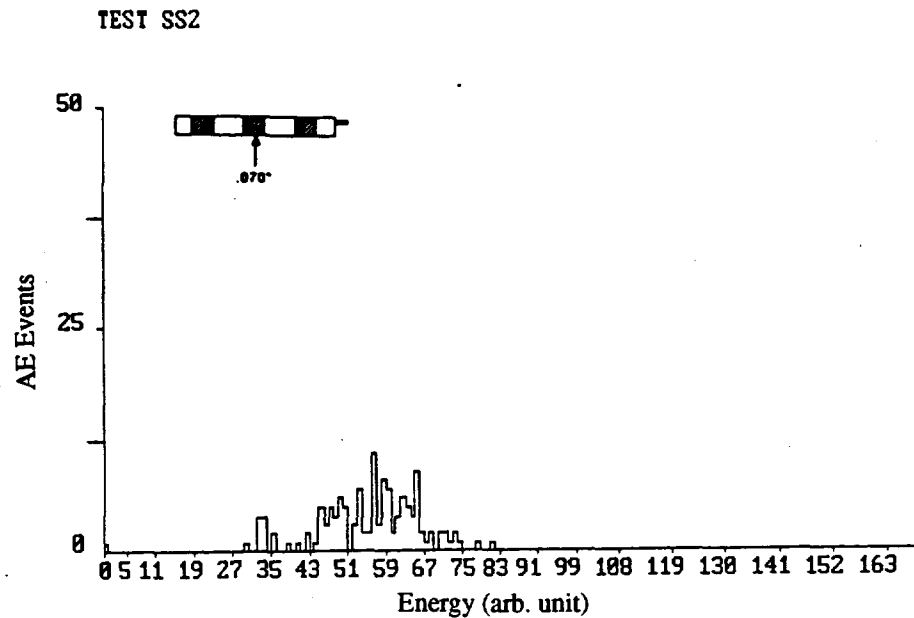


Figure 43 – TYPICAL DISTRIBUTION OF EVENTS BY ENERGY FOR .070" THICK STAINLESS STEEL COATINGS, MAXIMUM STRAIN CONDITION.

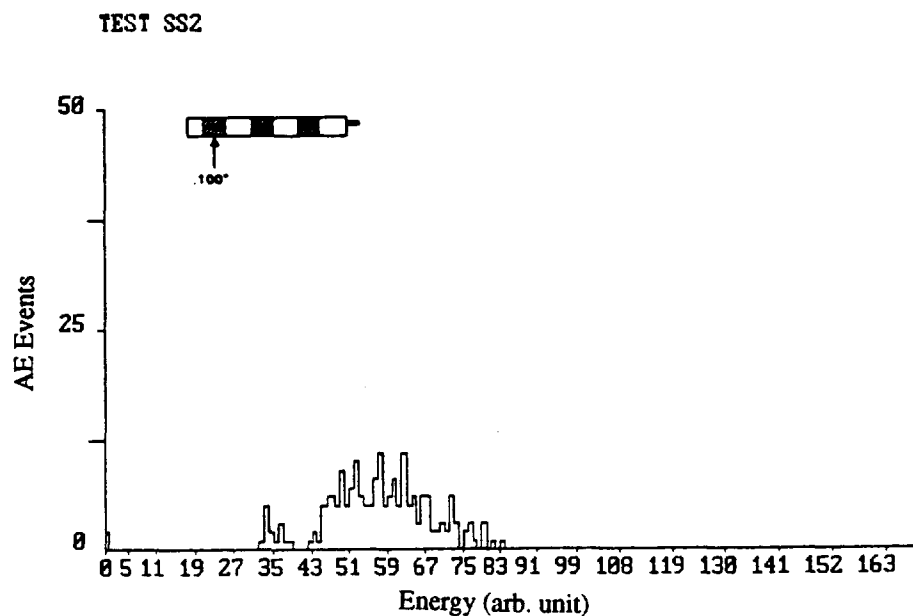


Figure 44 – TYPICAL DISTRIBUTION OF EVENTS BY ENERGY FOR .100" THICK STAINLESS STEEL COATINGS, MAXIMUM STRAIN CONDITION.

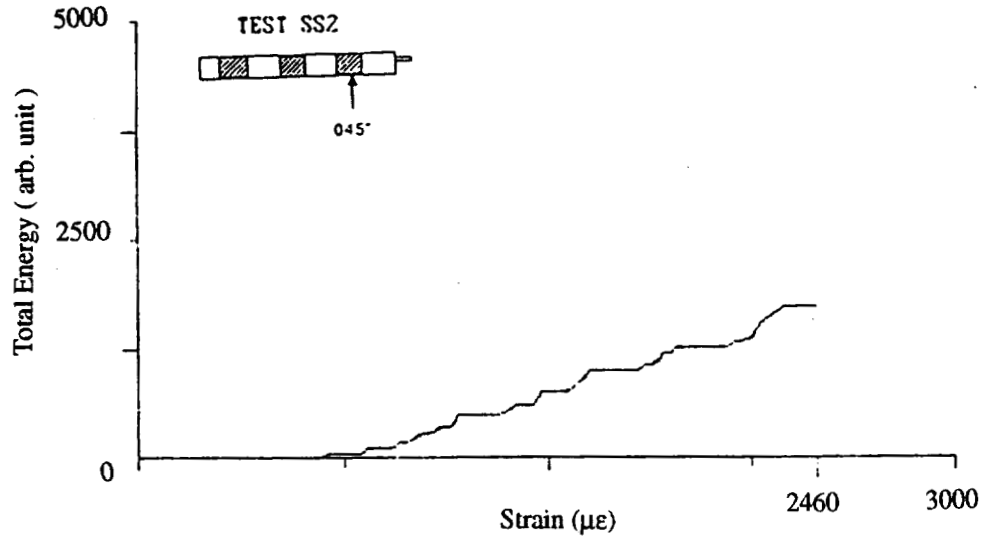


Figure 45 – TYPICAL TOTAL ENERGY VS. STRAIN FOR .045" THICK STAINLESS STEEL COATING. MAXIMUM STRAIN CONDITION.

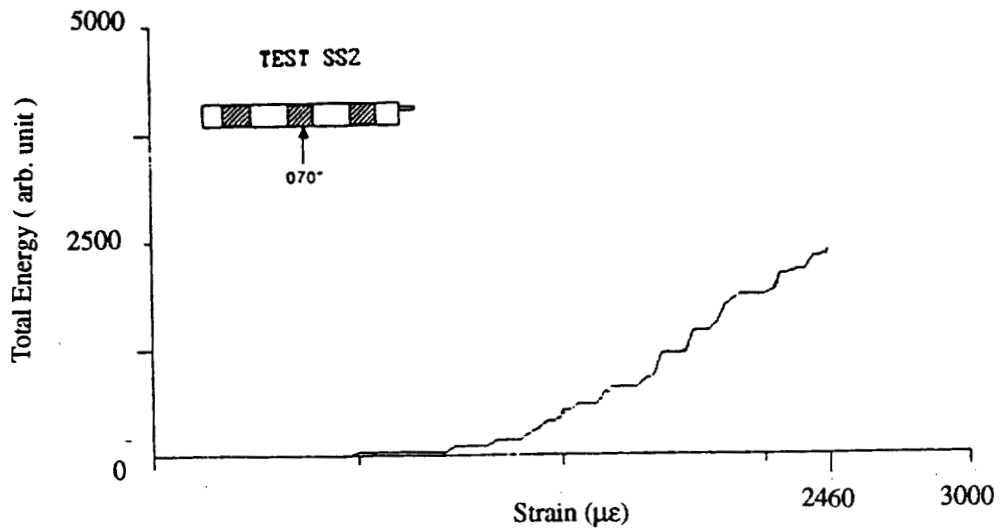


Figure 46 – TYPICAL TOTAL ENERGY VS. STRAIN FOR .070" THICK STAINLESS STEEL COATING. MAXIMUM STRAIN CONDITION.

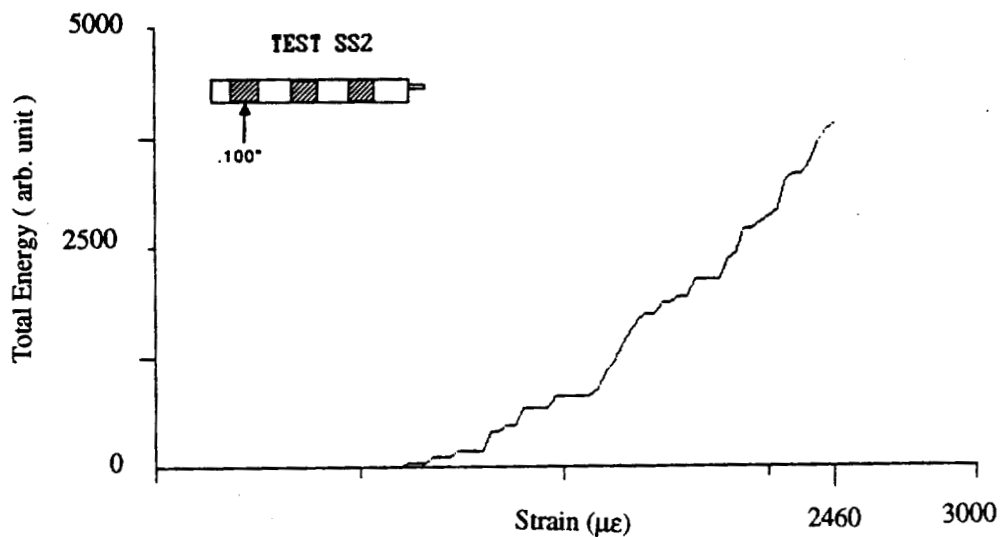


Figure 47 – TYPICAL TOTAL ENERGY VS. STRAIN FOR .100" THICK STAINLESS STEEL COATING. MAXIMUM STRAIN CONDITION.

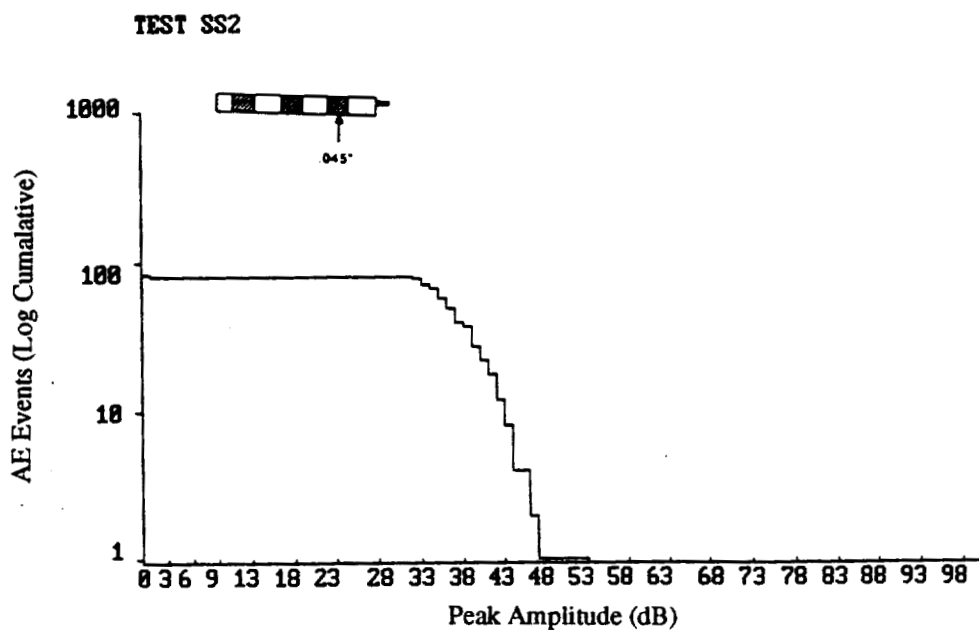


Figure 48 – TYPICAL LOG OF CUMULATIVE DISTRIBUTION OF EVENTS BY PEAK AMPLITUDE FOR .045" THICK STAINLESS STEEL COATING.

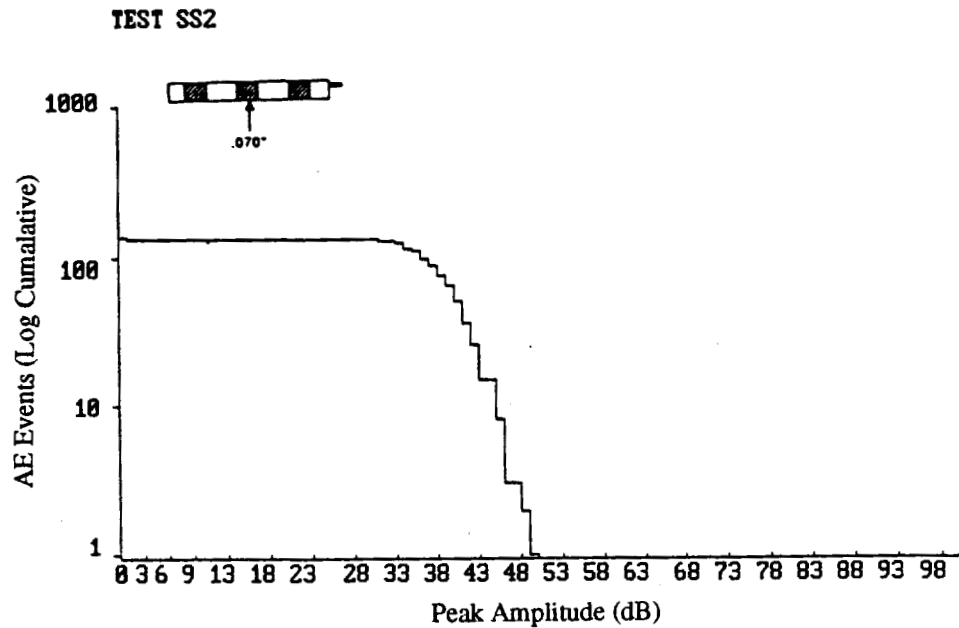


Figure 49 – TYPICAL LOG OF CUMULATIVE DISTRIBUTION OF EVENTS BY PEAK AMPLITUDE FOR .070" THICK STAINLESS STEEL COATING.

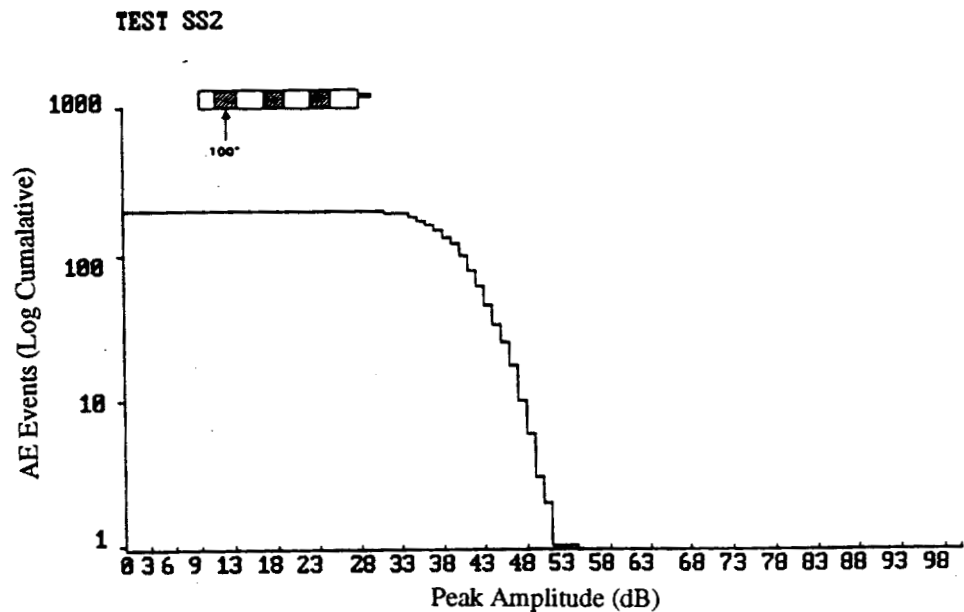


Figure 50 – TYPICAL LOG OF CUMULATIVE DISTRIBUTION OF EVENTS BY PEAK AMPLITUDE FOR .100" THICK STAINLESS STEEL COATING.

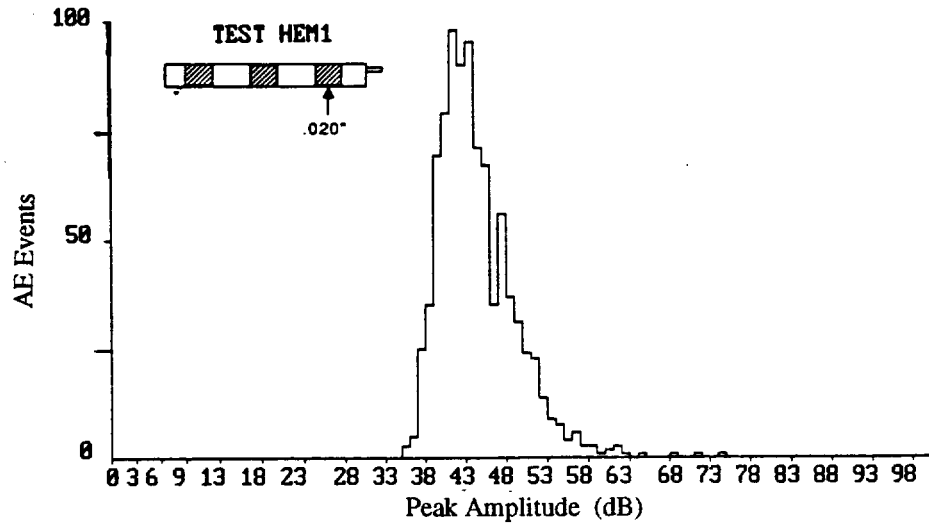


Figure 51 – DISTRIBUTION OF EVENTS BY PEAK AMPLITUDE (dB) FOR .020" THICK Mo-Fe BLEND COATING, MAXIMUM STRAIN CONDITION.

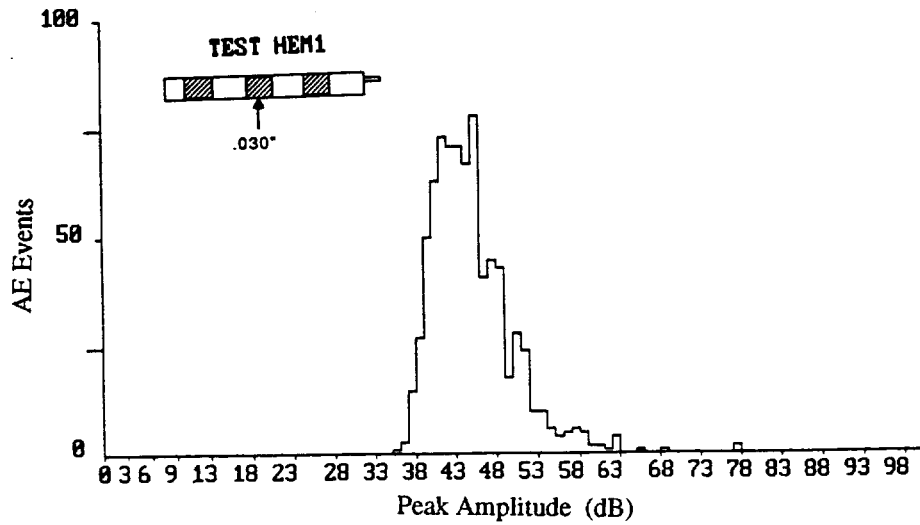


Figure 52 – DISTRIBUTION OF EVENTS BY PEAK AMPLITUDE (dB) FOR .030" THICK Mo-Fe BLEND COATING, MAXIMUM STRAIN CONDITION.

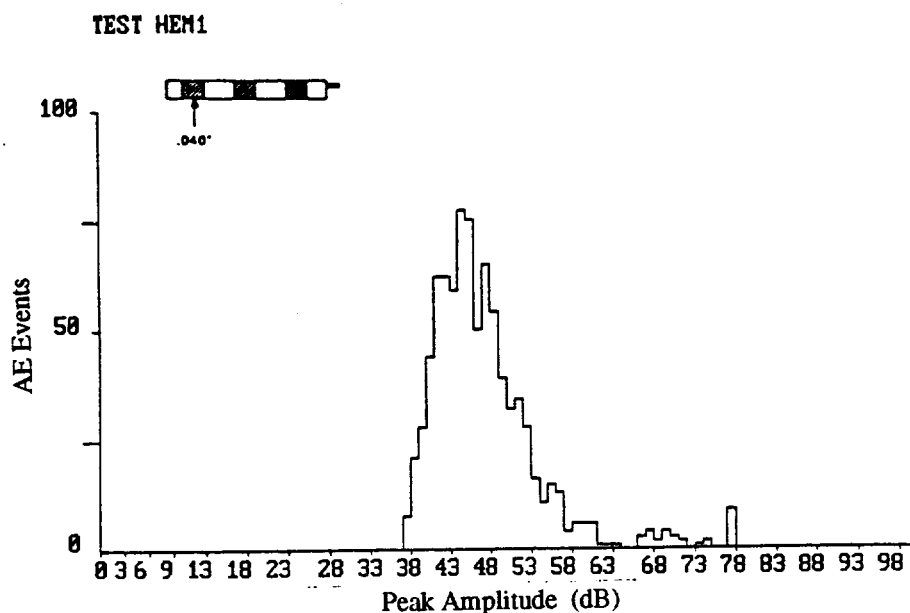


Figure 53 – DISTRIBUTION OF EVENTS BY PEAK AMPLITUDE (dB) FOR .040" THICK Mo-Fe BLEND COATING, MAXIMUM STRAIN CONDITION.

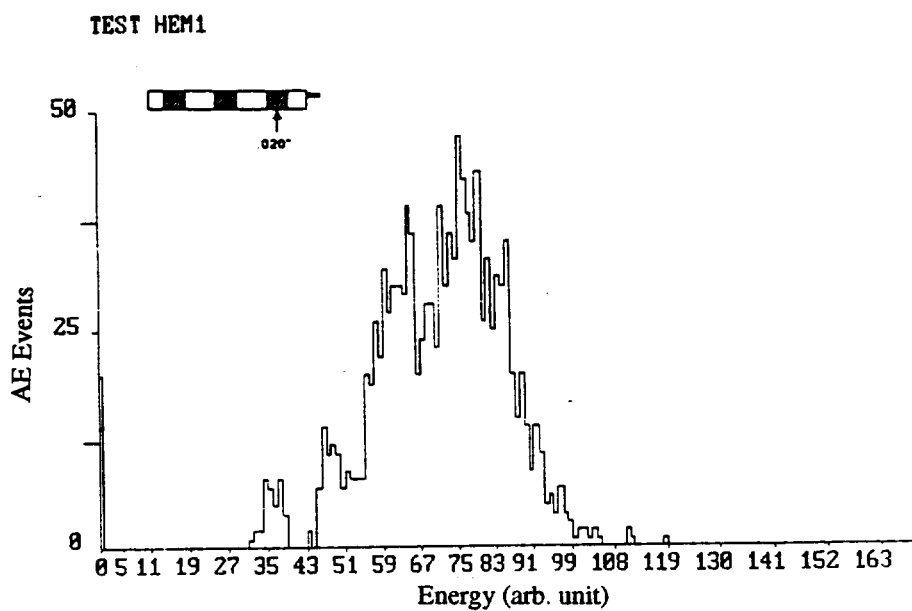


Figure 54 – DISTRIBUTION OF EVENTS BY ENERGY FOR .020" THICK Mo-Fe BLEND COATING, MAXIMUM STRAIN CONDITION.

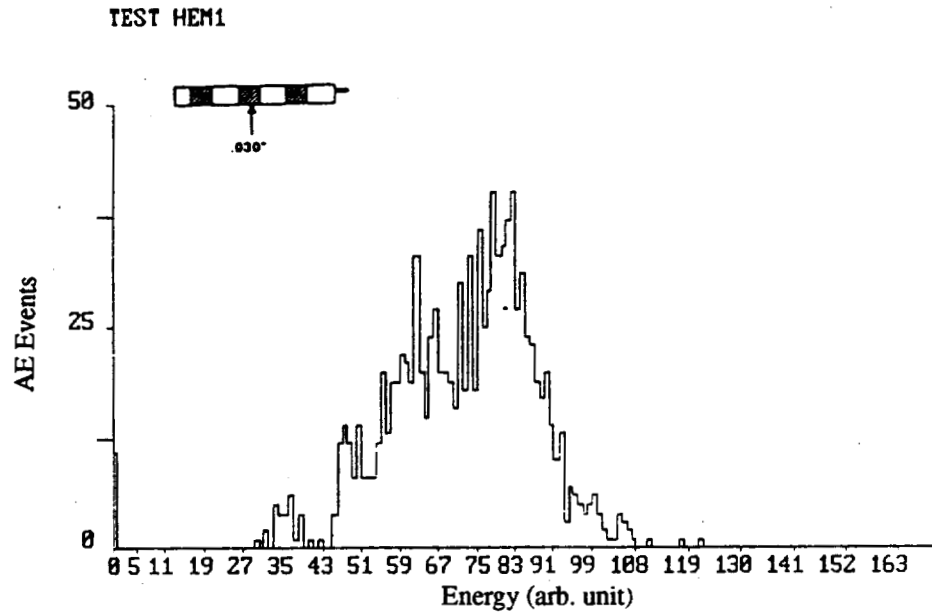


Figure 55 – DISTRIBUTION OF EVENTS BY ENERGY FOR .030" THICK Mo-Fe BLEND COATING, MAXIMUM STRAIN CONDITION.

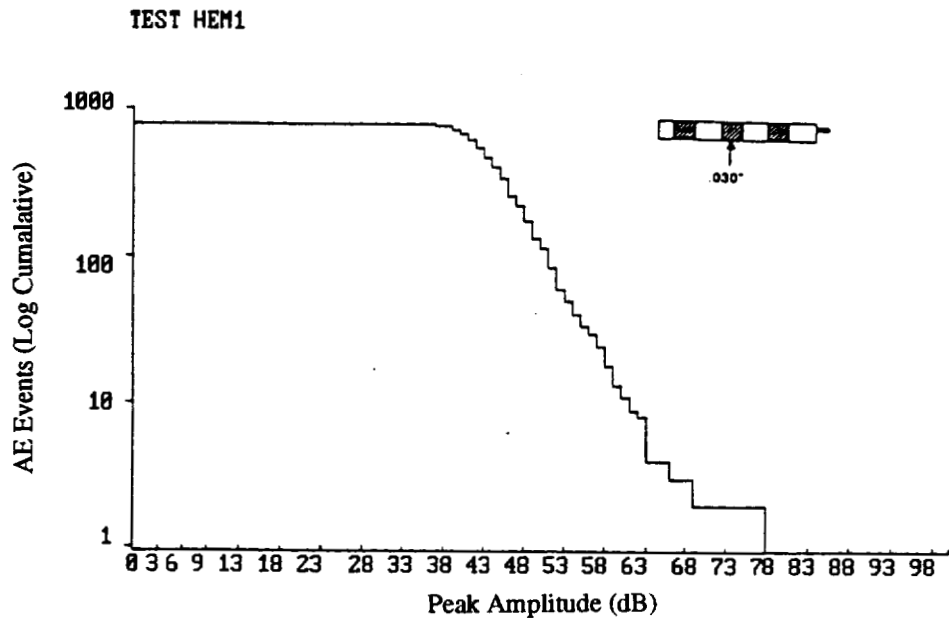


Figure 56 – LOG CUMULATIVE DISTRIBUTION OF EVENTS BY PEAK AMPLITUDE FOR .030" THICK Mo-Fe BLEND COATING. MAXIMUM STRAIN CONDITION.

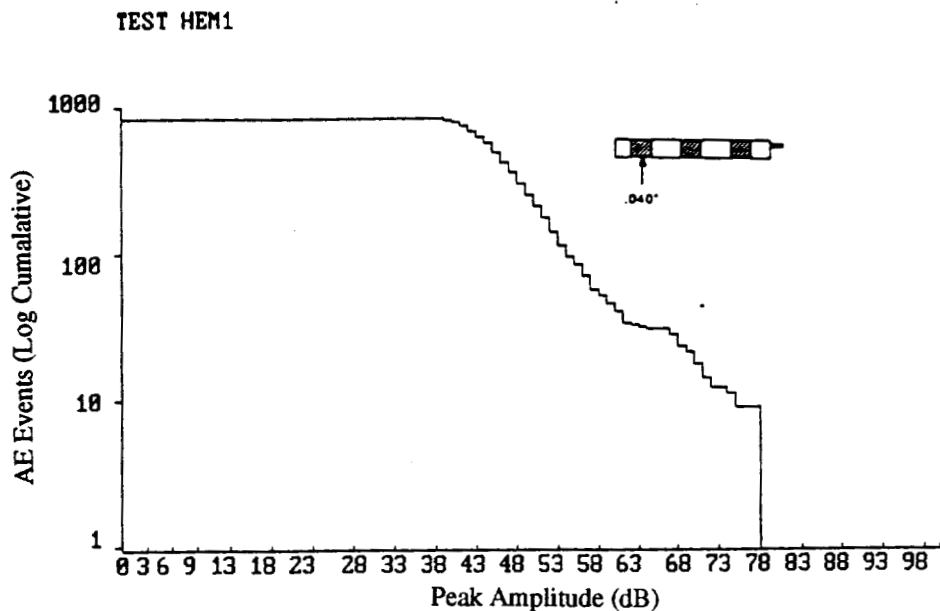


Figure 57 – LOG CUMULATIVE DISTRIBUTION OF EVENTS BY PEAK AMPLITUDE (dB) FOR .040" THICK Mo-Fe BLEND COATING. MAXIMUM STRAIN CONDITION.

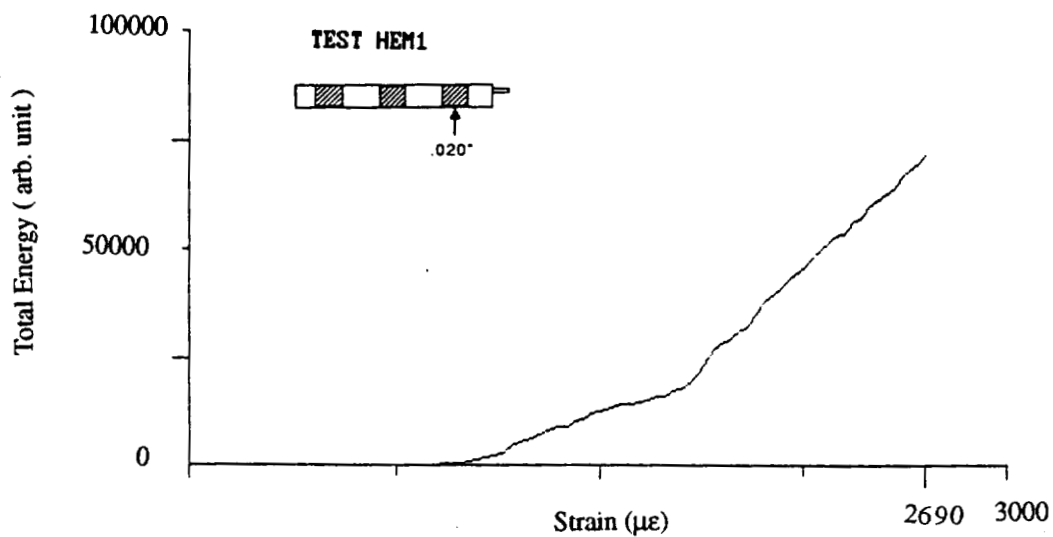


Figure 58 – TOTAL ENERGY VS. STRAIN FOR .020" THICK Mo-Fe BLEND COATING. MAXIMUM STRAIN CONDITION.

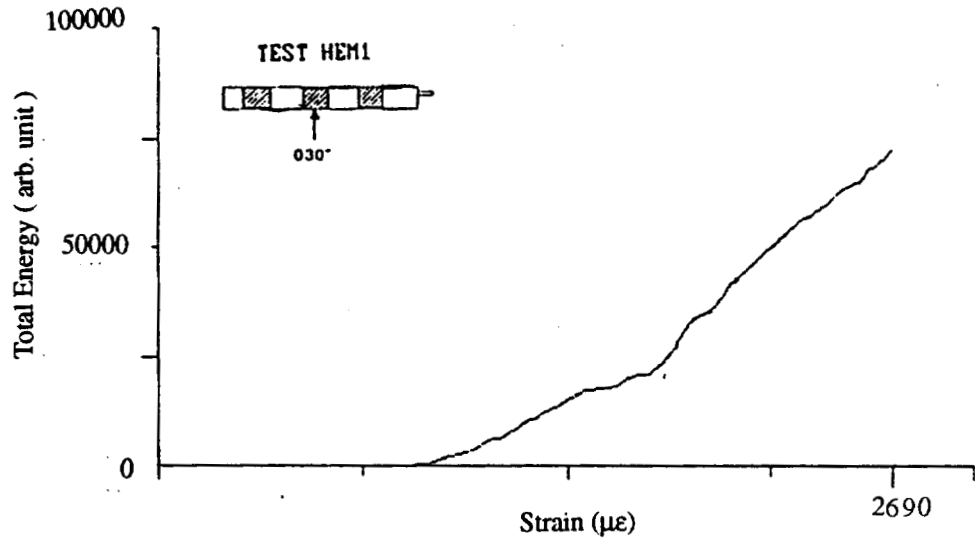


Figure 59 – TOTAL ENERGY VS. STRAIN FOR .030" THICK
Mo-Fe BLEND COATING. MAXIMUM STRAIN CONDITION.

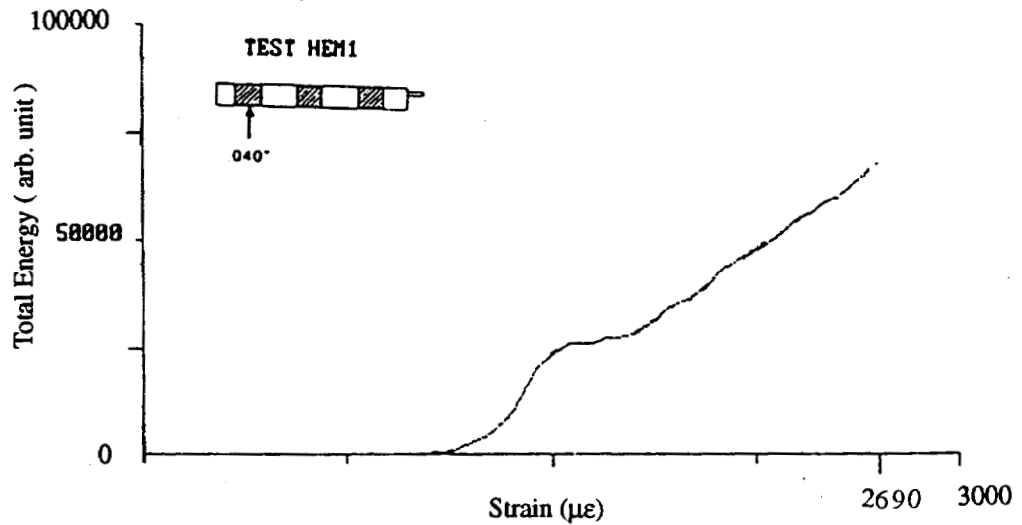


Figure 60 – TOTAL ENERGY VS. STRAIN FOR .040" THICK
Mo-Fe BLEND COATING. MAXIMUM STRAIN CONDITION.

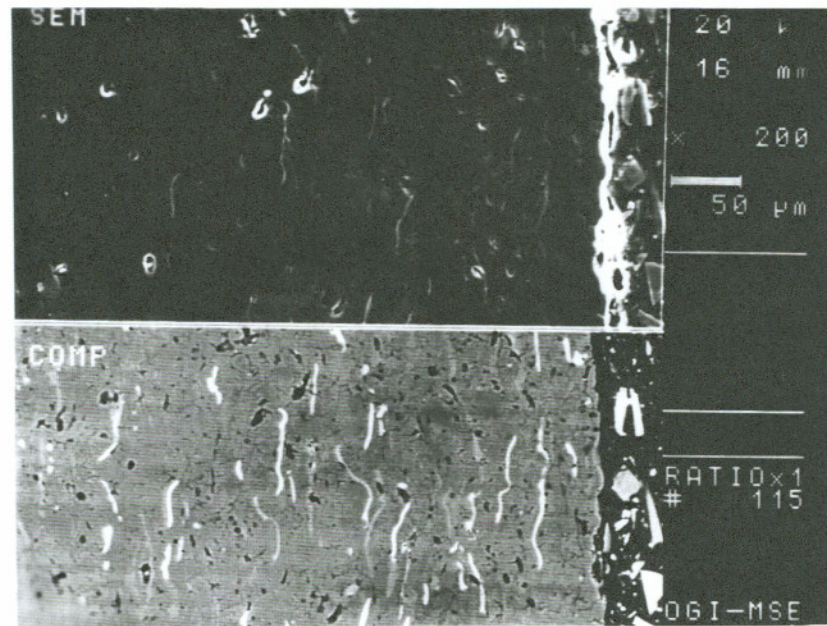


Figure 61 – SEM MICROGRAPH OF TYPICAL MICROSTRUCTURE OF UNSTRAINED .030" AL_2O_3 COATING. TOP IS SEM AND BOTTOM IS BSE-COMPOSITION, 200X.

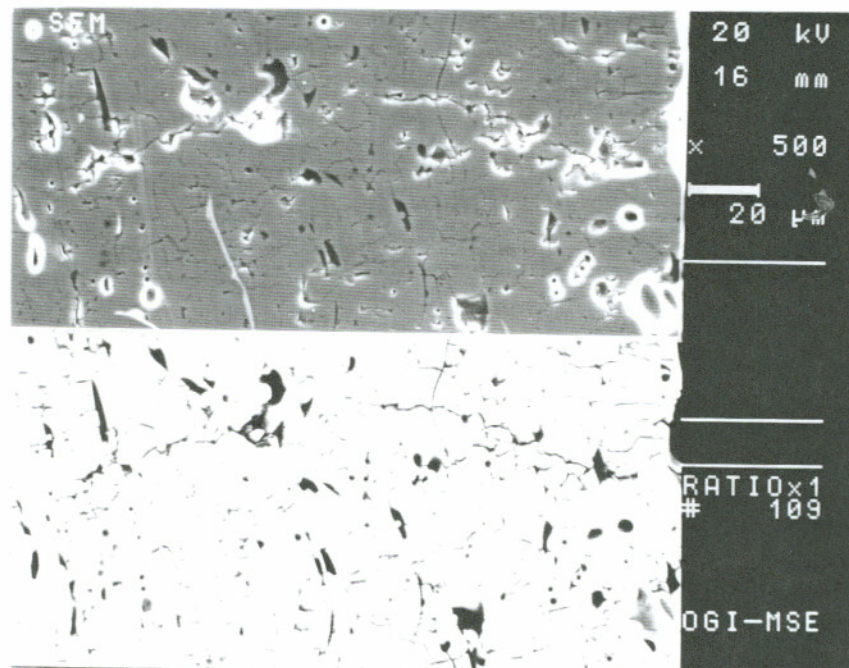


Figure 62 – SEM MICROGRAPH OF TYPICAL CRACKED AREA IN .015" THICK AL_2O_3 COATING. TOP IS SEM AND BOTTOM IS BSE-COMPOSITION, 500X.

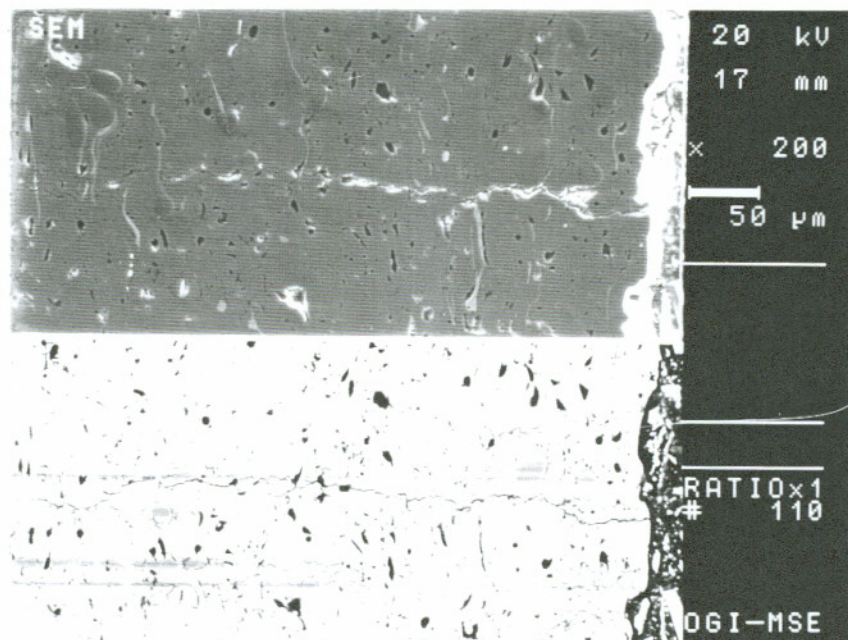


Figure 63 – SEM MICROGRAPH OF TYPICAL CRACKED AREA IN .030" THICK Al_2O_3 COATING. TOP IS SEM AND BOTTOM IS BSE-COMPOSITION, 200X.

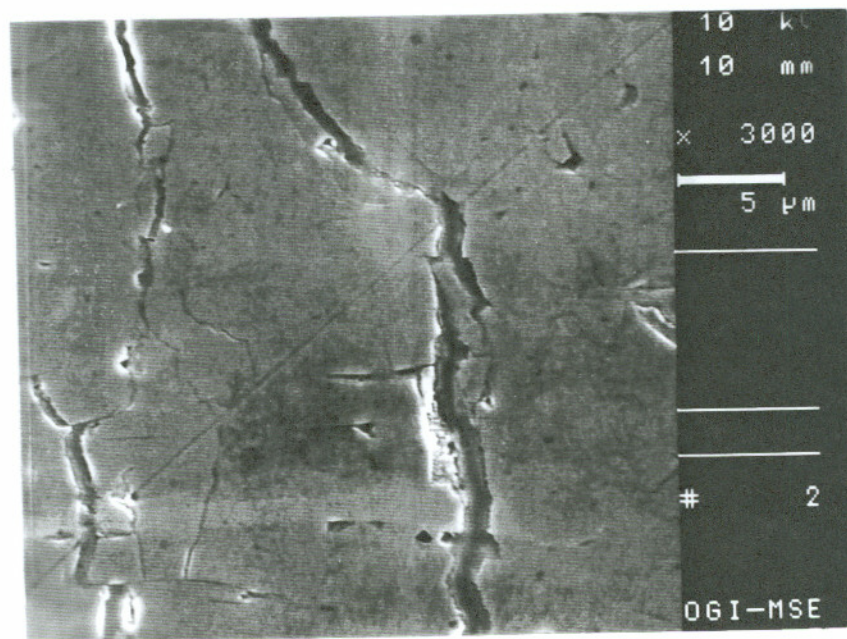


Figure 64 – SEM CLOSE UP OF A CRACK IN .045" THICK Al_2O_3 COATING 3000X.



Figure 65 – OPTICAL MICROGRAPH OF CRACKED AREA IN .045" THICK
AL₂O₃ COATING. 50X.

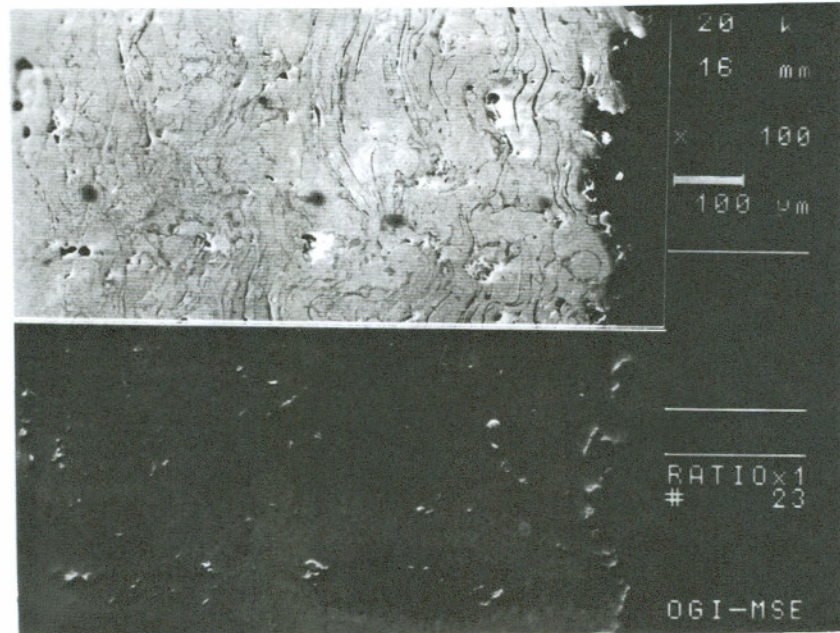


Figure 66 – SEM MICROGRAPH OF THE MICROSTRUCTURE OF .030" THICK STAINLESS STEEL COATING, UNSTRAINED CONDITION. TOP IS SEM AND THE BOTTOM IS BSE – TOPOGRAPHY. 100X.

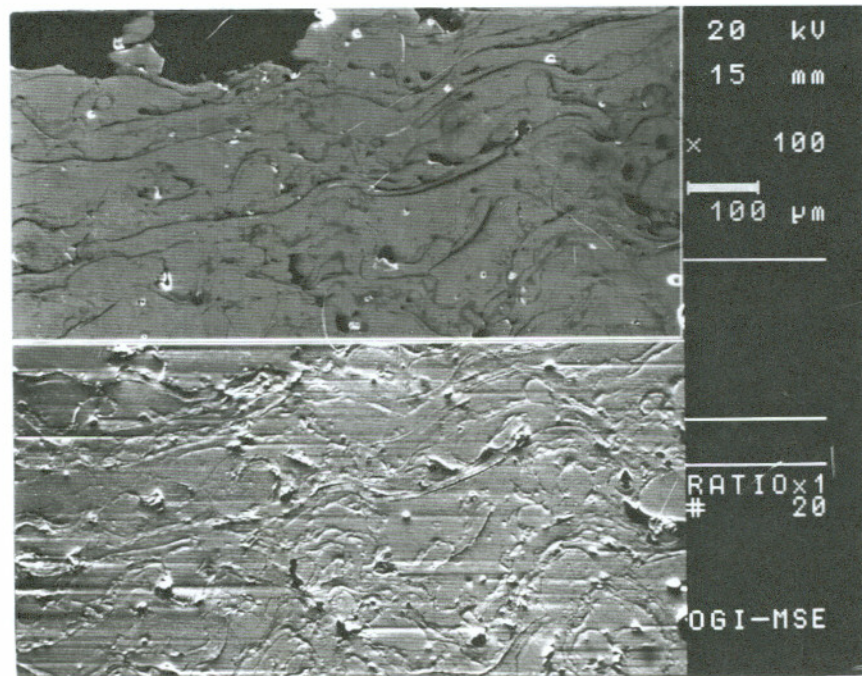


Figure 67 – SEM MICROGRAPH OF THE MICROSTRUCTURE OF .100" THICK STAINLESS STEEL COATING, STRAINED CONDITION. TOP IS SEM AND THE BOTTOM IS BSE – TOPOGRAPHY. 100X.

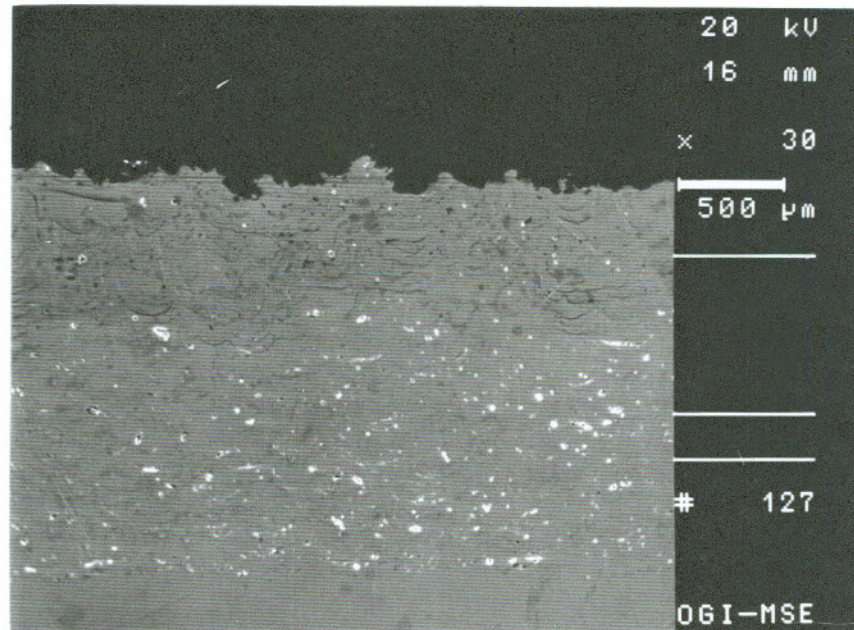


Figure 68 – SEM MICROGRAPH OF THE MICROSTRUCTURE OF .070" THICK STAINLESS STEEL COATING. STRAINED CONDITION.

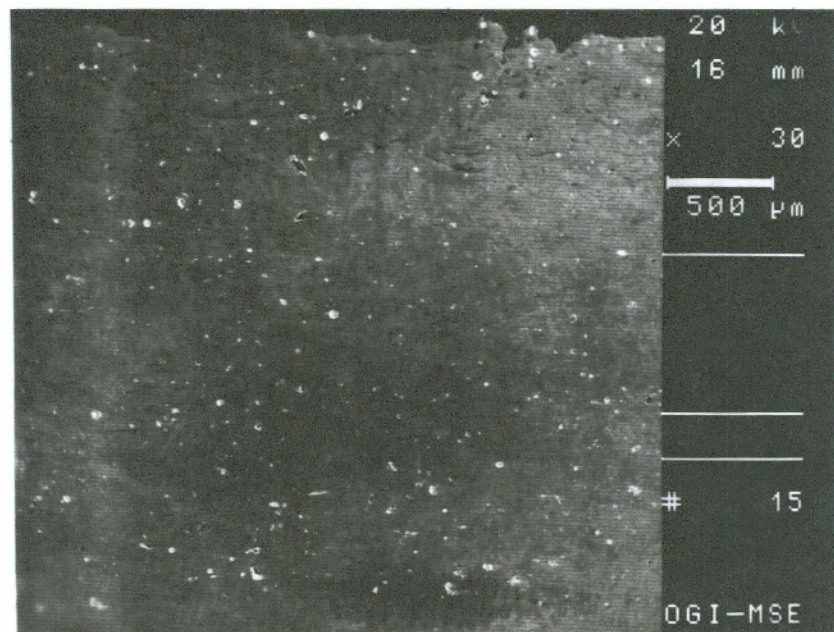


Figure 69 – SEM MICROGRAPH OF THE MICROSTRUCTURE OF .100" THICK STAINLESS STEEL COATING. STRAINED CONDITION. 30X.

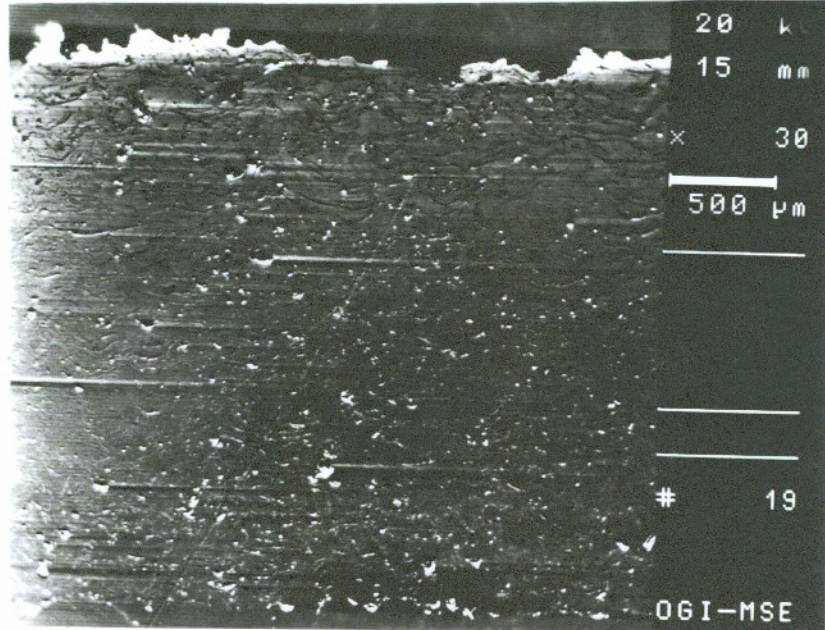


Figure 70 – SEM MICROGRAPH OF .100" THICK STAINLESS STEEL COATING. STRAINED CONDITION. BSE – TOPOGRAPHY 30X.

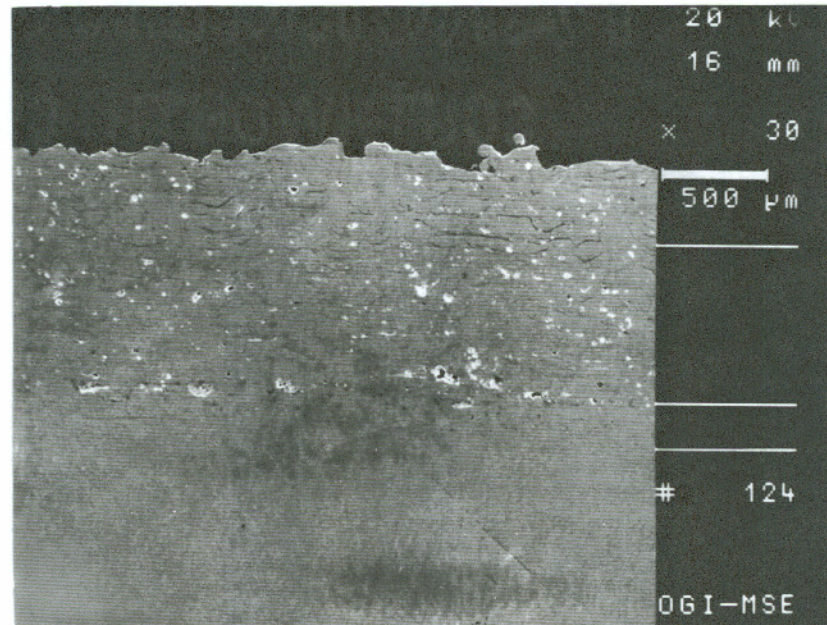


Figure 71 – SEM MICROGRAPH OF .045" THICK STAINLESS STEEL COATING. 30X.

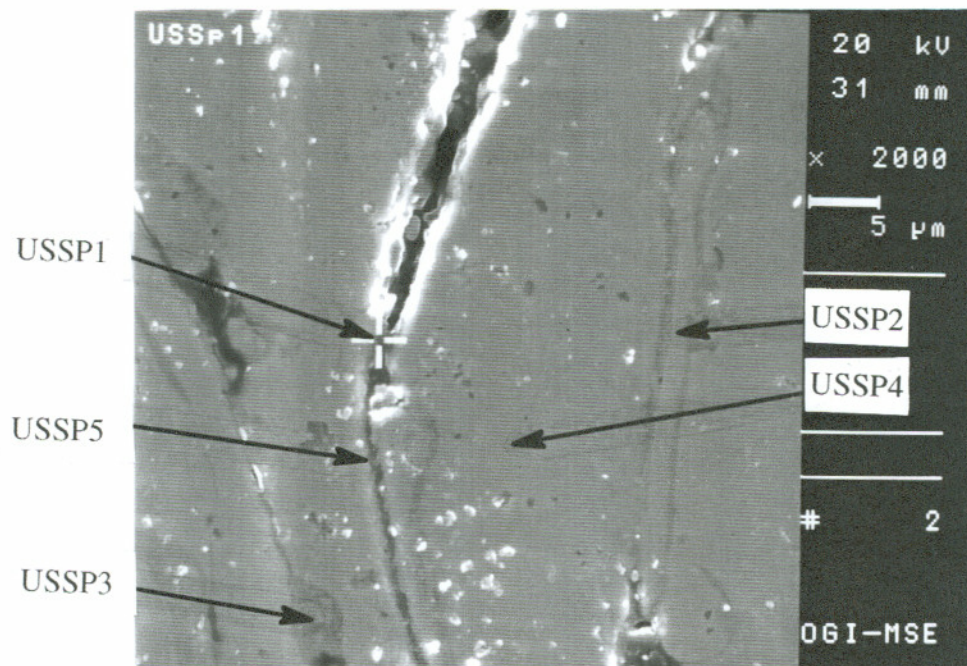


Figure 72 – MICROGRAPH OF EDX ANALYSIS AREAS. 2000X.

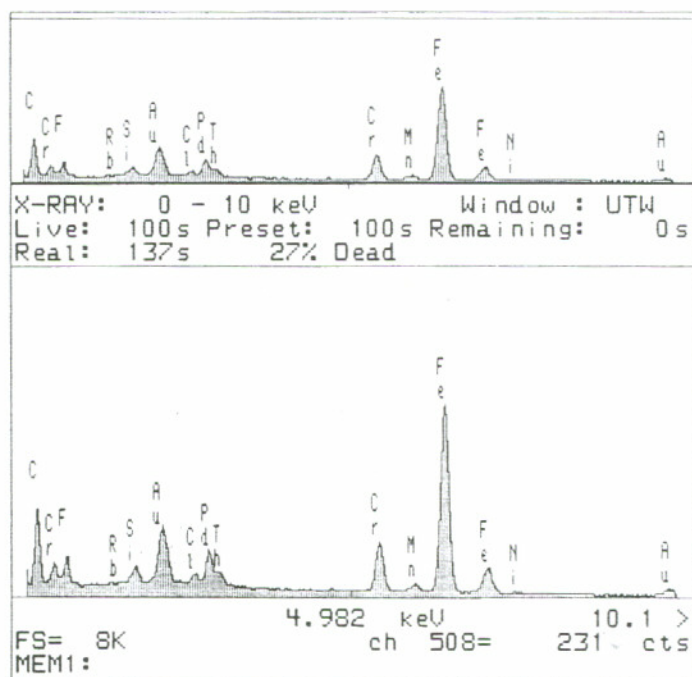


Figure 73 – EDX ANALYSIS OF AREA USSP1

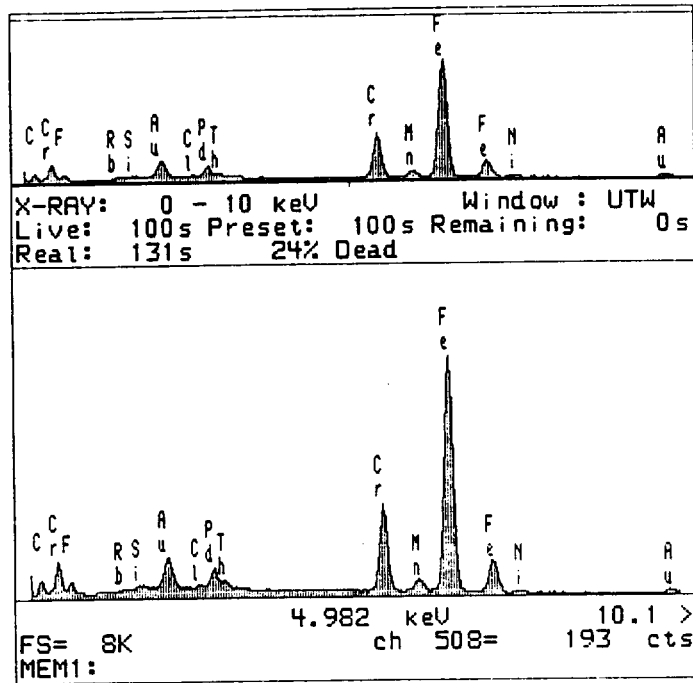


Figure 74 - EDX ANALYSIS OF AREA USSP2

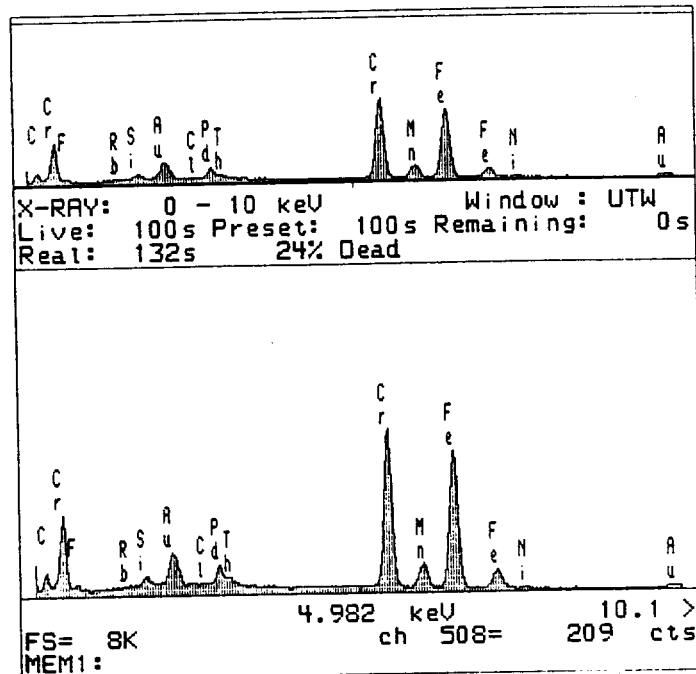


Figure 75 - EDX ANALYSIS OF AREA USSP3

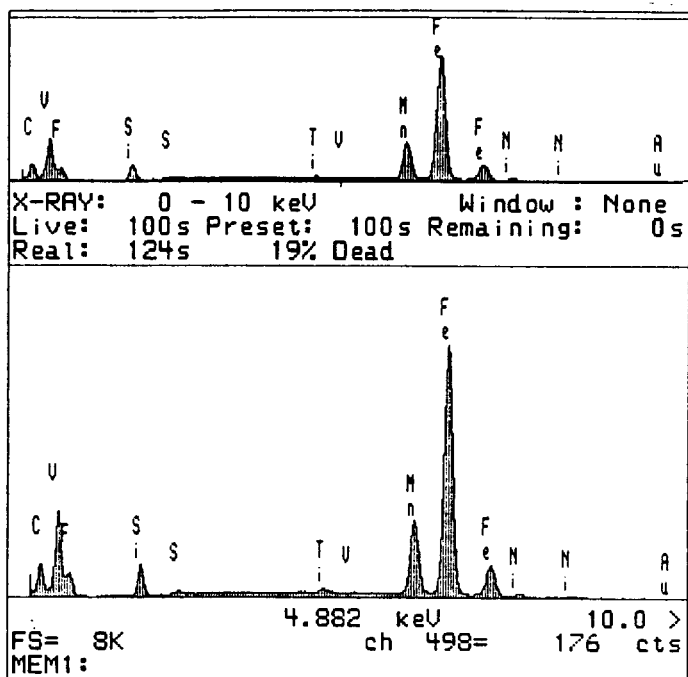


Figure 76 - EDX ANALYSIS OF AREA USSP4

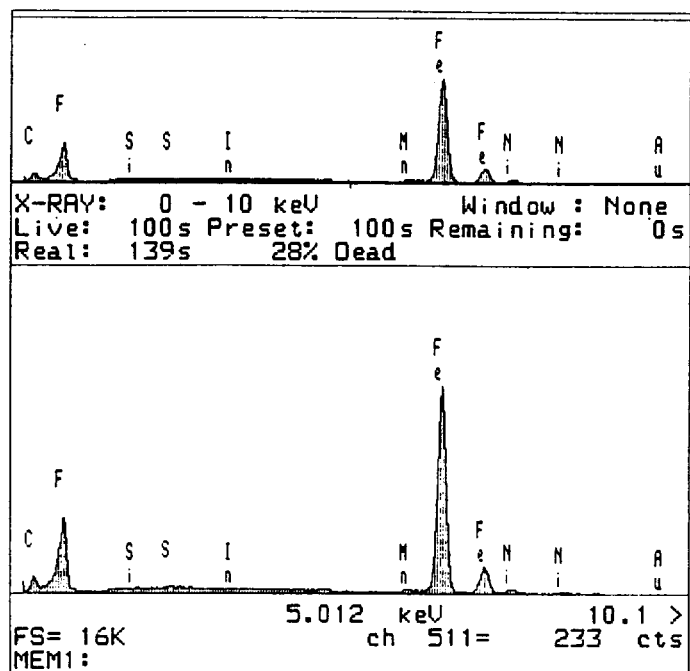


Figure 77 - EDX ANALYSIS OF AREA USSP5

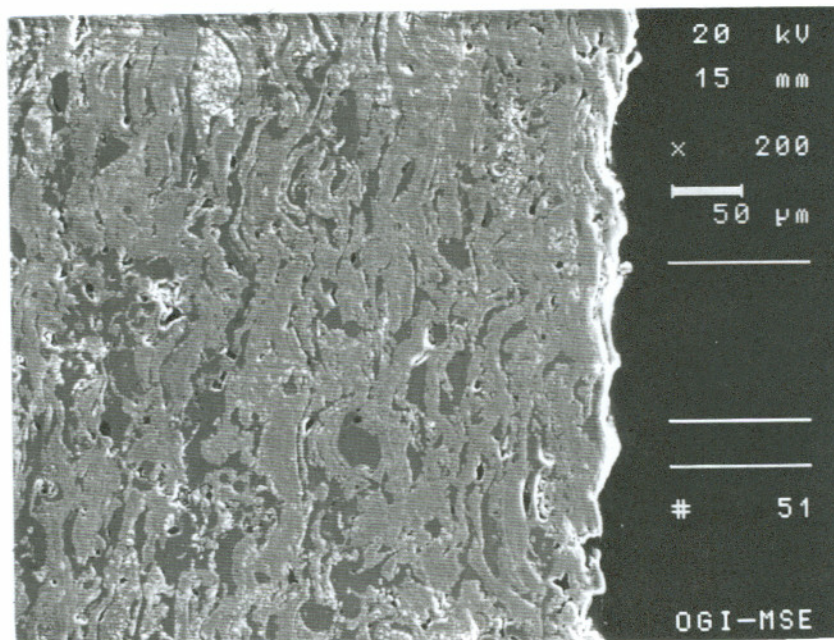


Figure 78 – SEM MICROGRAPH OF .030" THICK Mo-Fe BLEND COATING UNSTRAINED CONDITION (STANDARD ATMOSPHERE). SEM. 200X.

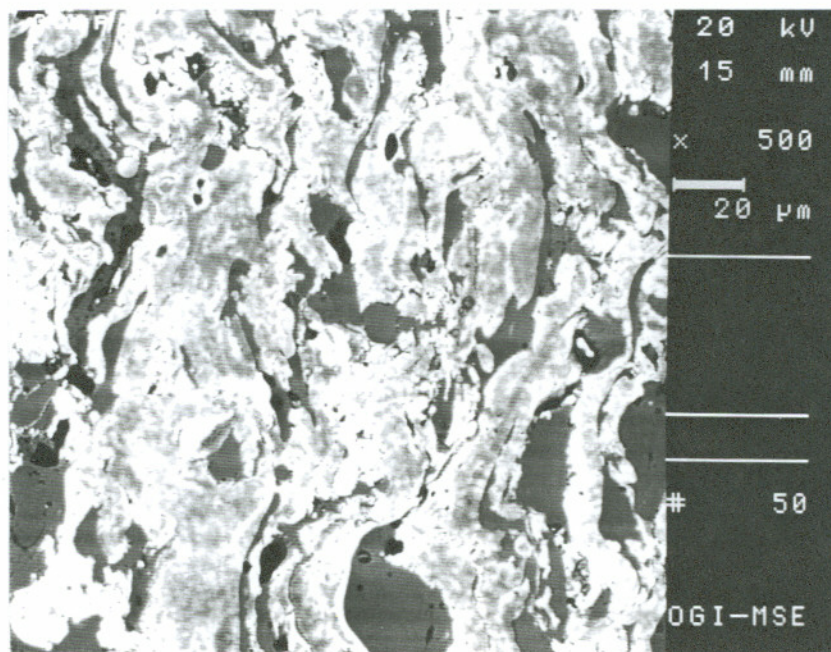


Figure 79 – SEM MICROGRAPH OF .030" THICK Mo-Fe BLEND COATING UNSTRAINED CONDITION (STANDARD ATMOSPHERE). BSE-COMPOSITION. 500X.

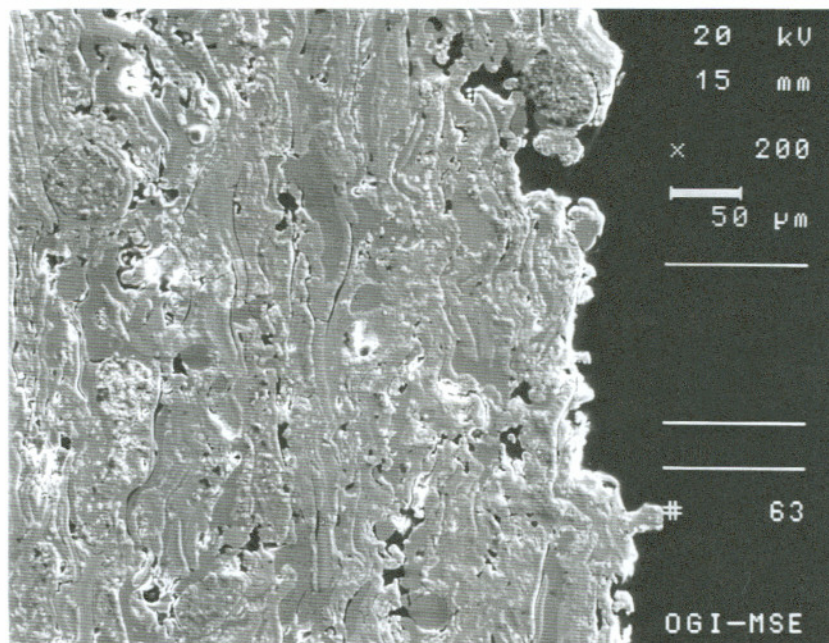


Figure 80 – SEM MICROGRAPH OF .030" THICK Mo-Fe BLEND COATING. UNSTRAINED CONDITION. (ARGON ATMOSPHERE). SEM. 200X.

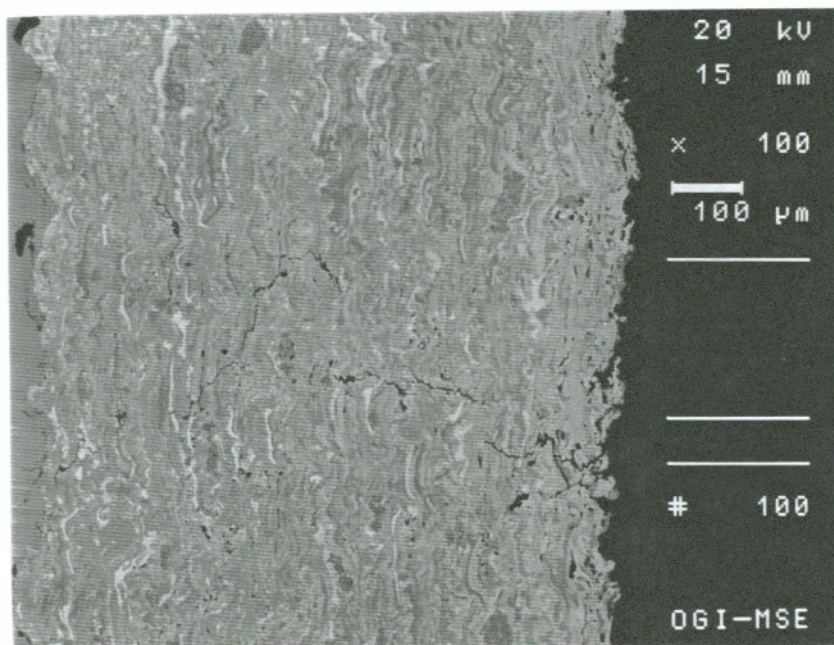


Figure 81 – SEM MICROGRAPH OF CRACKING IN .030" THICK Mo-Fe BLEND COATING. BSE-COMPOSITION. 100X.

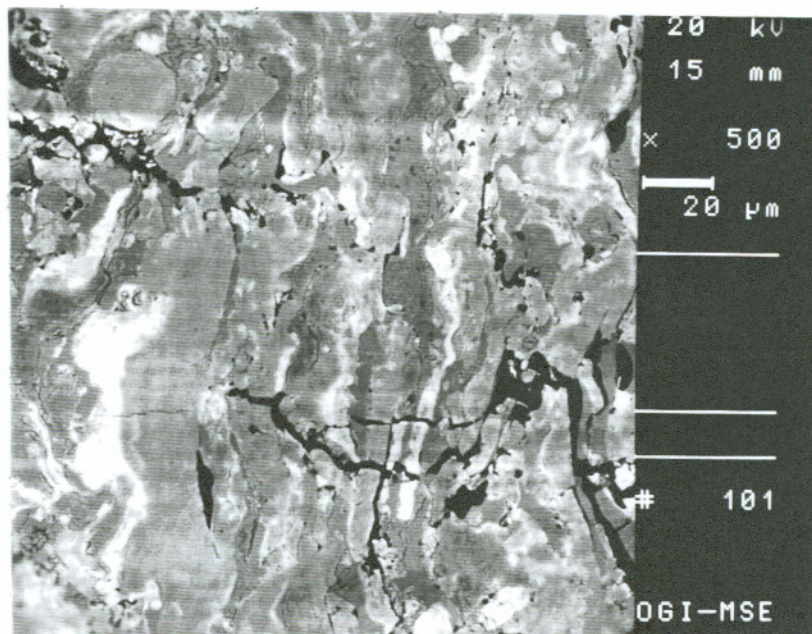


Figure 82 – SEM MICROGRAPH CLOSE UP OF CRACK FROM FIGURE 84. BSE-COMPOSITION. 500X.

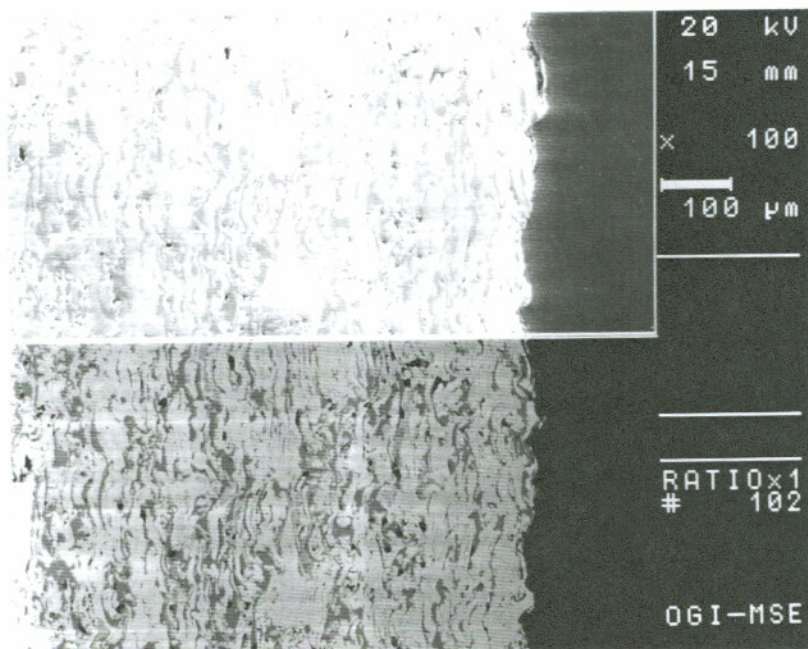


Figure 83 – SEM MICROGRAPH OF CIRCUMFERENTIAL CROSS SECTION OF COATING FROM FIGURES 84 AND 85. TOP IS SEM AND BOTTOM IS BSE-COMPOSITION 100X.

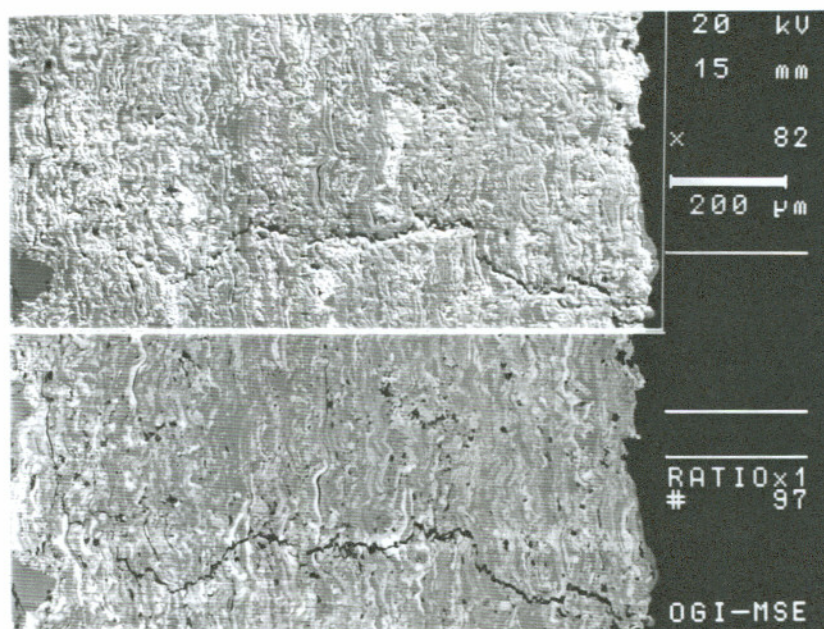


Figure 84 – SEM MICROGRAPH OF CRACKING IN .040" THICK Mo-Fe BLEND COATING. TOP IS SEM AND BOTTOM IS BSE-COMPOSITION. 100X.

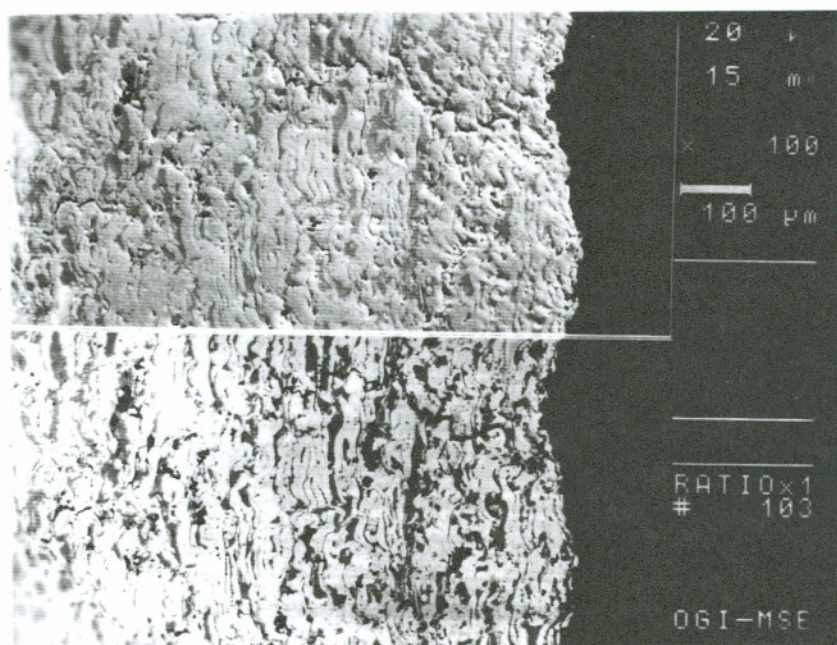


Figure 85 – SEM MICROGRAPH OF CRACKING IN .043" THICK Mo-Fe BLEND COATING. TOP IS SEM AND BOTTOM IS BSE-COMPOSITION. 100X. CIRCUMFERENTIAL DIRECTION

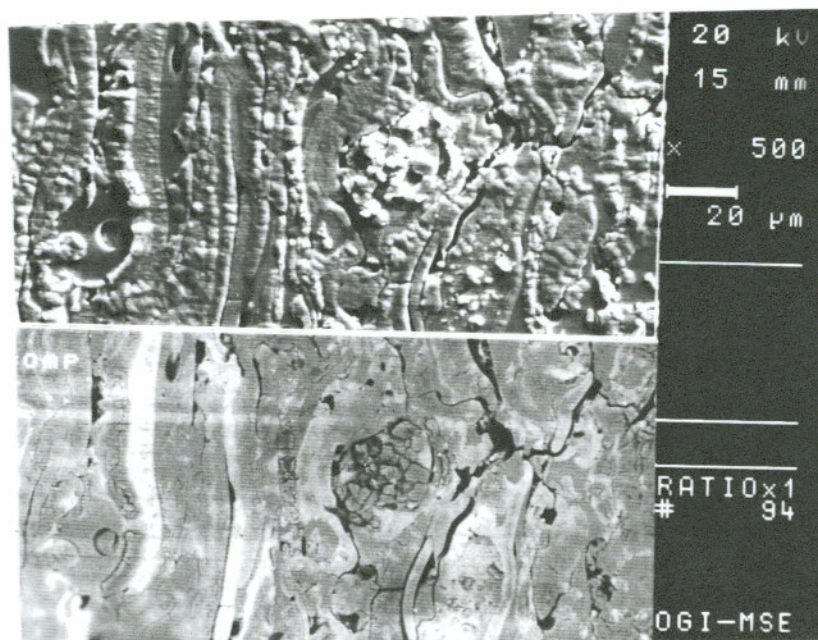


Figure 86 – SEM MICROGRAPH OF MINOR CRACKING IN .020" THICK Mo-Fe BLEND COATING, MINIMUM STRAIN. TOP IS SEM AND BOTTOM IS BSE-COMPOSITION. 500X.

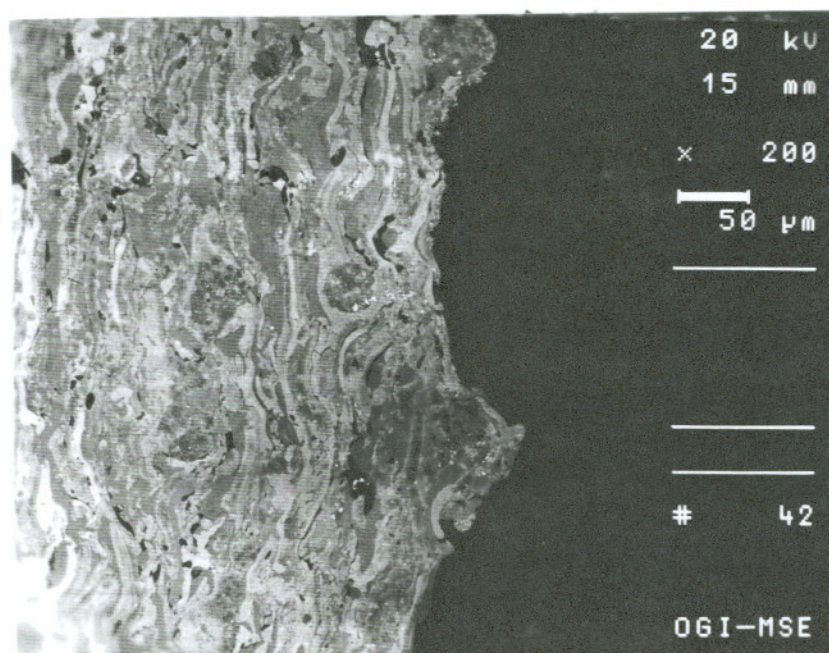


Figure 87 – SEM MICROGRAPH OF MINOR CRACKING IN .030" THICK Mo-Fe BLEND COATING, MINIMUM STRAIN. BSE-COMPOSITION. 500X.

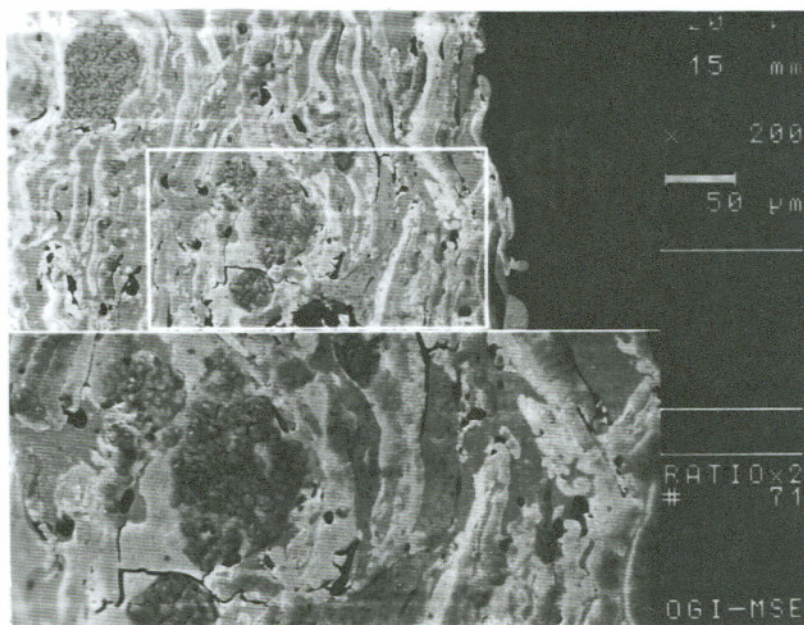


Figure 88 – SEM MICROGRAPH OF MINOR CRACKING IN .040" THICK Mo-Fe BLEND COATING, MINIMUM STRAIN. BSE-COMPOSITION. 200X. INSET = 400X.

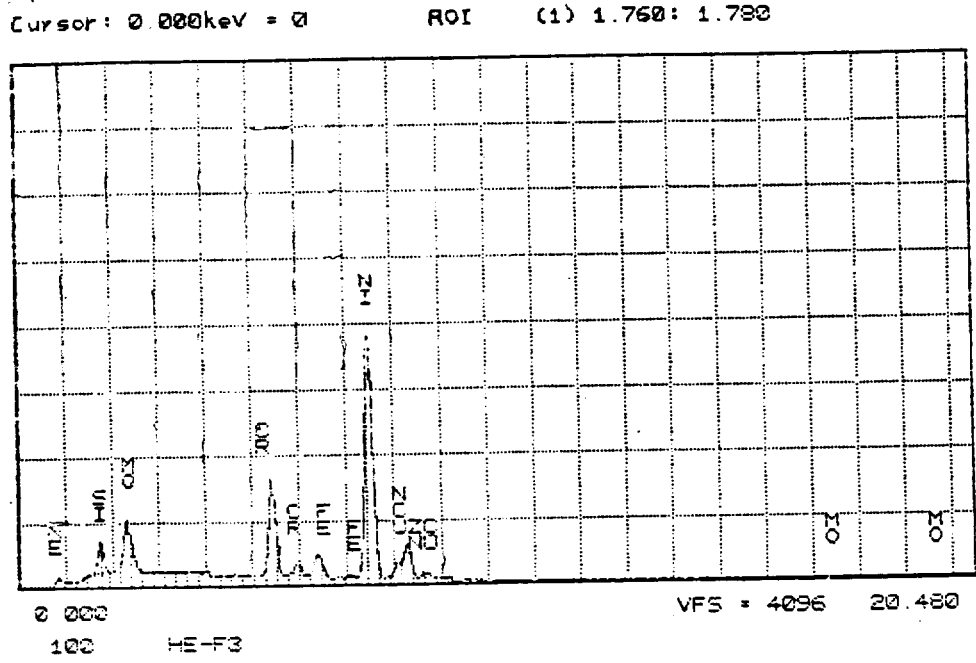


Figure 89 – EDX ANALYSIS OF Mo-Fe BLEND COATING.

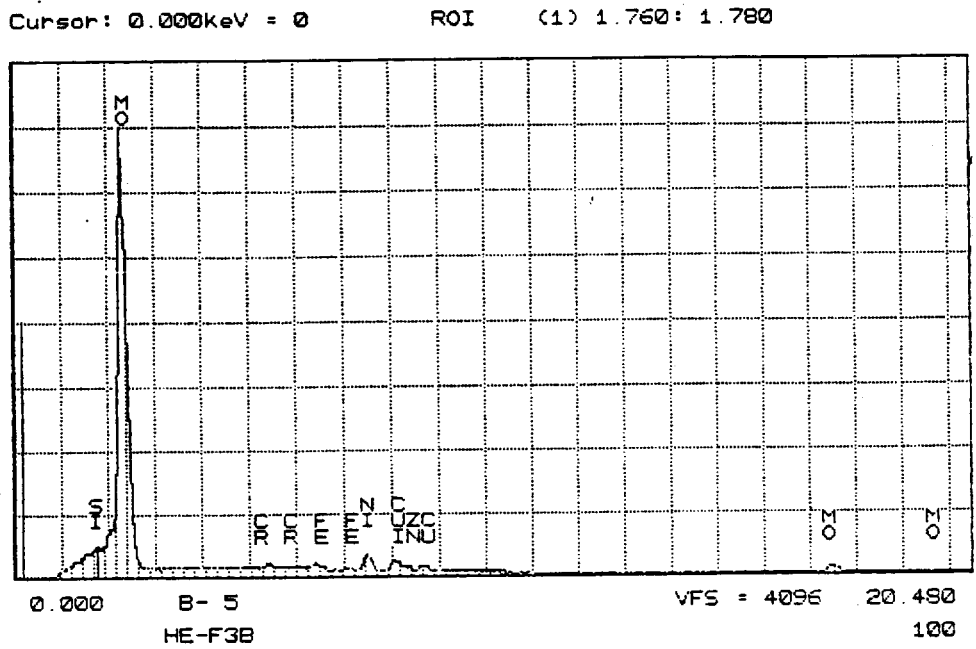


Figure 90 – EDX ANALYSIS OF Mo-Fe BLEND COATING.

11. TABLE I – Coating Matrix

TUBE CODE	COATING	LOCATION	THICKNESS, in.
A,B,C,D	Al ₂ O ₃ (METCO 101)	1	0.015
		2	0.030
		3	0.045
E,F,G,H	Stainless Steel (SS420)	1	0.045
		2	0.070
		3	0.100
I,J	Molybdenum Blend (Mo – Fe with some Ni and Cr)	1	0.020
		2	0.030
		3	0.040
K	Sprayed with alloys of each type. For metallographic observation with no strain. One thicknes only.		

12. TABLE II – Test Code Designation

TEST CODE	TUBE CODE
AL02	A
AL03	B
AL04	C
AL05	D
HEM1	I
HEM3	J
SS1	G
SS2	H
SS3	F
SS5	E

13. TABLE III – Maximum Strain Reached By Each Tube

TUBE CODE	STRAIN ($\mu\epsilon$)
A	2540
B	2400
C	2400
D	1480
E	2260
F	2420
G	2340
H	2460
I	2690
J	680
K	NO STRAIN

14. TABLE IV – Test Statistics of Accepted Events

TEST	COATING SECTION 1	COATING SECTION 2	COATING SECTION 3
ALO2	0	0	250
ALO3	0	4	377
ALO4	0	13	481
SS1	58	230	115
SS2	82	133	198
SS3	174	589	537
HEM1	1255	1095	1119
HEM3	18	182	8

15. TABLE V – Test Statistics of Rejected Events

TEST	RING DOWN COUNT	EVENT DURA- TION	PEAK AMPLI- TUDE	OUT OF REGION	OUT OF ORDER	DELTA TIME
ALO2	0	0	0	194	1055	286
ALO3	0	1	0	268	1674	425
ALO4	0	0	0	398	1754	501
ALO5	0	0	0	0	25	10
SS1	0	1	0	526	5349	2152
SS2	0	3	0	643	10857	2618
SS3	0	21	0	2038	17165	8928
HEM1	0	70	0	3298	8309	10407
HEM3	0	0	0	229	841	497

16. TABLE VI – Strain At Which Onset of Significant AE Activity Began

COATING	STRAINING ($\mu\epsilon$)
A1	
A2	
A3	1760
B1	
B2	
B3	1560
C1	
C2	1680
C3	
D1	
D2	
D3	
E1	510
E2	420
E3	390
F1	760
F2	340
F3	360
G1	700
G2	540
G3	800
H1	660
H2	740
H3	1110
I1	630
I2	840

Table VI Continued

COATING	STRAING ($\mu\epsilon$)
I3	910
J1	460
J2	320
J3	390

**17. TABLE VII – Approximate Slope of Total Events vs. Strain Plots
(events/mv)**

TEST	SECTION 1	SECTION 2	SECTION 3
ALO2			1851
ALO3			3831
ALO4			4227
SS1	135	833	534
SS2	264	461	756
SS3	529	1618.5	1800
SS5	370	679	1053
HEM1	2749	3290	2237
HEM3	6667	5802	5144

18. REFERENCES

1. Berndt, C. C. "Acoustic Emission Evaluation of Plasma-Sprayed Thermal Barrier Coatings," in Transactions of ASME, Vol. 107, January 1985, pp.142-146.
2. Almond, D., Moghisi, M., and Reiter, H., "The Acoustic Emission Testing of Plasma-sprayed Coatings," Thin Solid Film, Vol. 108,1983, pp. 439-447.
3. Wen, L., Zhang, H., Zhou, X., Guan, K., Liao, B., and Cao, S., "Acoustic Emission Research on the Fracture Behaviour of Plasma Sprayed Ni-Al Coating During Bend Testing," Surfacing Journal International, Vol. 1(4), 1986, pp. 151-153 .
4. American Society for Testing and Materials, "Standard Test Method for Adhesion or Cohesive Strength of Flame-Sprayed Coatings," ASTM C633 - 79, Annual Book of ASTM Standards, Vol. 02.05, 1994.
5. Hayes, E. Jr. and Thun, D., "Development of A Thermally Efficient Paper Machine Yankee Dryer Coating," Thermal Spray Coatings: New Materials, Processes and Applications (Proceeds of Conference), Long Beach, Ca., 1984, pp. 21-26.
6. Ono, K., Jeng, J., Yang, J., "Fracture Mechanism Studies of A Carbon Fiber-Peek Composite by Acoustic Emission," Acoustic Emission: Current Practice and Future Direction, ASTM STP 1077, Philadelphia, Pa. 1991, pp. 395-403.
7. Shankar, N., Berndt, C. C., and Herman, H., "Characterization of the Mechanical Properties of Plasma-sprayed Coatings," Advances In Materials Characterization, Materials Science Research, Vol. 15, edited by David R. Rossington, Robert A. Condrate, and Robert L. Snyder, Plenum Press, 1983, pp. 473-488,
8. Pollock, A., "Acoustic Emission Inspection," Metals Handbook, 9th ed., Nondestructive Evaluation and Control, Vol. 17, edited by ASM International Handbook Committee, pp. 278-291.
9. Ghaffari, S. and Awerbauch, J., "On the Correlation Between Acoustic Emission and Progression of Matrix Splitting in a Unidirectional Graphite/Epoxy Composite," in Acoustic Emission-Current Practice and Future Direction, ASTM STP 1077, pp. 404-415.

10. Shankar, N., Berndt, C. C., and Herman, H., "Structural Integrity of Thermal Barrier Coatings by Acoustic Emission Studies," in Proceedings of the Tenth International Thermal Spraying Conference, Essen, Germany, May 1983, pp. 41-45.
11. Berndt, C. C., "Behavior of Plasma-sprayed Coatings," Ultrastructure Processing of Ceramics, Glasses, and Composites, edited by L. L. Hench and D.R. Ulrich, J. Wiley and Sons, 1984, pp. 524-532.
12. Yosio, N., Veach, C., and Mccauley, B., "Amplitude Distribution of Acoustic Emission Signals," in Acoustic Emission, ASTM STP 505, American Society of Testing Materials, 1972, pp.164-185.
13. Pollock, A., "Acoustic Emission Amplitude Distributions," in International Advances In Nondestructive Testing, Vol. 7, Gordon and Breach, Science Publishers (Inc.), 1981, pp. 215-239.
14. Pollock, A., "Classical Wave Theory in Practical AE Testing," in Progress in Acoustical Emission III, The Japanese Society of NDI, 1986, pp. 708-719.
15. Almond, D. and Reiter, H., "Novel Ways of Looking at Thermal Spray Coatings," Surfacing Journal, Vol. 16, January 1985, pp. 5-11.
16. Carpenter, S. and Smith, D., "The Effects of Cathodic Charging on the Acoustic Emission Generated by Intergranular Cracking in Sensitized 304 Stainless Steel," Metallurgical Transactions A, Vol. 21a, July 1990, pp. 1933-1938.
17. METCO Technical Report, "The Preparation of Specimens for Process Control of Flame Sprayed Coatings by Metallography," May 1971, METCO Inc., Westbury, New York.
18. Brindley, W. and Leonhardt, T., "Metallographic Techniques for Evaluation of Thermal Barrier Coatings," Materials Characterization, Vol. 24, 1990, pp. 93-101.
19. Richert, M., "Plasma Spray Coating Symposium," Copenhagen, Struers Co., Literature, 1988.
20. Kopp, W. and Muller, G., "The Preparation of Porous Materials," Practical Metallography, Vol. 22, 1985, pp. 490-495.
21. Buehler Dialog, "Plasma Sprayed 89W, 7Co, 4C Hard Coating on Carbon Steel," Method Number 12.01, 1989, Buehler Co. Literature.
22. Wellner, P. and Hoven, H., "Techniques for Preparing Polished Sections and the Structural Classification of Special Ceramics With Different Porosities," Practical Metallography, Vol. 18, 1981, pp. 3-13.

23. Blann, G., "Metallographic Specimen Preparation of Thermally Sprayed Coatings for Microstructural Analysis," reprint from Microstructural Science, Image Analysis and Metallography, ASM International, Vol. 17, 1989, pp. 139-151.
24. Elssner, G. and Wellner, P., "Preparation Problems and Phase Identification in Plasma-Sprayed Coatings for High Temperature Applications," Microstructural Science, Vol. 9, 1981, pp. 287-297.
25. Blann, G., Diaz, D., and Nelson, J., "Raising the Standards for Coating Analysis," reprint from Advanced Materials and Processes, December 1989, pp. 31, 34-36.

19. Biographical Sketch

Christine Steinkamp was born July 2, 1955 in Portland, Oregon. She graduated from Wilson High School, Portland, Oregon in 1973. She received a Bachelor of Science Degree in Applied Science and Engineering - Mechanical Engineering in 1979 from Portland State University, Portland, Oregon. Upon graduation she worked for Tektronix Inc. as an electro-mechanical engineer from June 1979 to December 1981.